22 August 2023

NA61/SHINE Analysis Note

Proton intermittency analysis of ^{208}Pb + ^{208}Pb collisions at beam momentum of 13*A* and 30*A* GeV/*c*, and ^{40}Ar + ^{45}Sc collisions at beam momenta of 13*A*-75*A* GeV/*c*

Haradhan Adhikary

Abstract

This note presents the analysis details of Pb+Pb collisions at 13*A* ($\sqrt{s_{NN}} \approx 5.1$ GeV), 30*A* GeV/*c* ($\sqrt{s_{NN}} \approx 7.6$ GeV), and Ar+Sc at 13*A*, 19*A*, 30*A*, 40*A* and 75*A* GeV/*c* beam momentum ($\sqrt{s_{NN}} \approx$ 5.1-11.9 GeV) recorded by NA61/SHINE at the CERN SPS. The goal of this analysis is to search for the critical point of strongly interacting matter. The existence and location of the QCD critical point are objects of both experimental and theoretical studies. It may represent a region in the QCD phase diagram where the properties of strongly interacting matter exhibit non-analytic behavior. The intermittency analysis is performed using both transverse momentum and cumulative transverse momentum, and statistically independent data sets are used for each subdivision number. The results are an important milestone in the search for the critical point of strongly interacting matter.

NA61 Doc:		
EDMS Id:		
Version:	version-1	
Last modified:	22:51 on 22 August 2023	
Prepared by:	**Checked by:**	**Approved by:**
Haradhan Adhikary		

Contents

1 Introduction

The goal of these analyses is to search for the Critical Point (CP) [1] of strongly interacting matter [2] by measuring the second scaled factorial moments (SSFMs) [3] of selected proton candidates within the analyses acceptance in 0-10% of the most central ^{208}Pb + ^{208}Pb collisions at beam momenta of 13*A* and 30*A* GeV/*c* and ^{40}Ar + ^{45}Sc collisions at beam momenta of 13*A*, 19*A*, 30*A*, 40*A*, and 75*A* GeV/*c*. Not all recorded events were eligible for analysis as *central* collisions in the target and not all recorded tracks were the primary products of such collisions. Therefore, optimization was done by introducing selection criteria for events and tracks. In this analysis note, the event and track selection for ^{208}Pb + ^{208}Pb and ^{40}Ar + ^{45}Sc data sets is presented. Also the first results of proton intermittency results for ^{208}Pb + ^{208}Pb collisions at beam momentum of 13*A* and 30*A* GeV/*c* and ^{40}Ar + ^{45}Sc collisions at beam momenta of 13*A*-75*A* GeV/*c* is presented here. This analysis note is organized as follows:

(i) brief introduction of CP and intermittency analysis (Sec. 2 and Sec. 3),

(ii) event selection including the *centrality* selection (Sec. 5),

(iii) single-track selection including proton candidate selection (Sec. 6),

(iv) single-particle acceptance maps (Sec. 7),

(v) two-particle acceptance map (mTTD cut) (Sec. 8),

(vi) new approach to proton intermittency (Sec. 9),

(vii) proton intermittency results (Sec. 10).

As an illustration of the selection procedure, the distributions before and after the event and track selection for all analyzed ^{208}Pb + ^{208}Pb and ^{40}Ar + ^{45}Sc data sets are documented here.

2 Critical point of strongly interacting matter

The diagram shown in Fig. 1 illustrates the phases of matter that can be observed in a system described by Quantum Chromodyanmics (QCD) [4] and is commonly referred to as the phase diagram of strongly interacting matter. This representation is based on state-of-the-art QCD findings.

The phase diagram presented in Fig. 1 follows a format similar to that of water's phase diagram. In this diagram, temperature (T) is plotted on the ordinate and baryon chemical potential (μ_B) on the abscissa, which plays the same role as the pressure in the water phase diagram. The purpose of this diagram is to illustrate the characteristics of different phases and their boundaries, serving as a tool to describe the system's thermodynamic singularities. Several phases are distinguished in this diagram, including hadron gas [5], nuclear-matter [6], QGP [8], quark-matter [9, 10], and color-flavor-locked (CFL) [11].

The transition that proceeded from the HG phase to the QGP phase is similar to the transition from liquid water to water vapour along a first-order transition line ending in a second-order critical point and followed by a cross-over transition. In Fig. 1, the first-order phase transition is marked, which separates the HG and QGP phases. The QGP-HG transition also separates regions with broken chiral symmetry [1] (hadron gas state) and restored chiral symmetry (QGP

[1]Chirality is a projection of spin to momentum vector of particle. Chiral symmetry refers to the axial flavour transformation of the quark part of the QCD Lagrangian density, which requires massless quarks. The chiral symmetry is broken due to the existence of massive quarks [13].

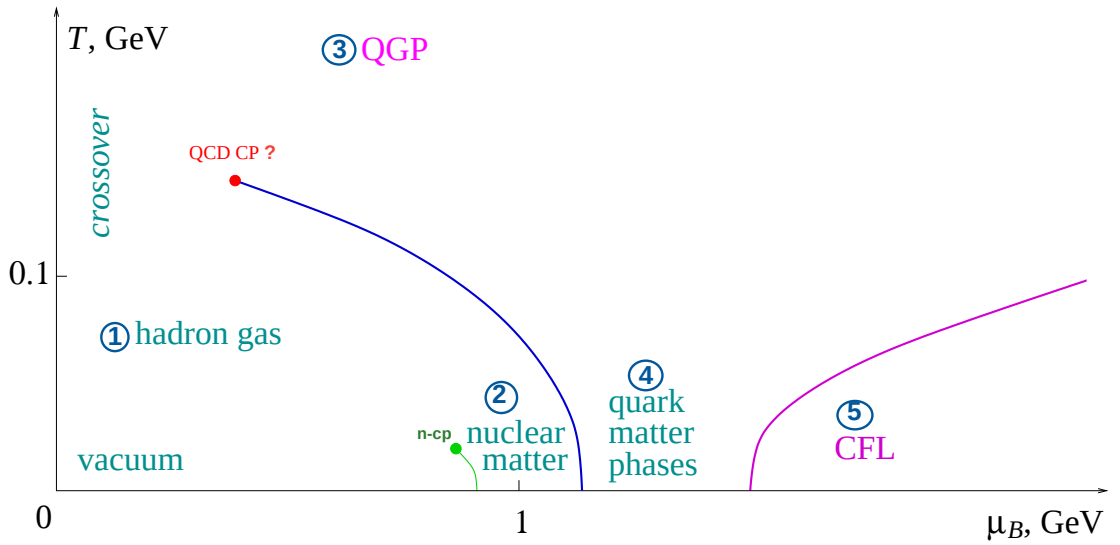

Figure 1: A semi-quantitative illustration of the contemporary view of the phase diagram of strongly interacting matter. Different phases of matter are marked on the phase diagram: 1) hadron gas [5], 2) nuclear matter [6], 3) QGP [7, 8], 4) quark matter [9, 10] and 5) CFL [11] phases. Also, the hypothetical QCD critical point and crossover are mentioned. The green line at small temperatures and high densities shows the nuclear liquid-gas transition, also ending at a critical point (n-cp). The figure is taken from Ref. [12].

state). For many years, it was claimed that chiral transition and deconfinement occur at the same T and μ_B. The later studies [14, 15] showed that these two transitions might be separated in the phase diagram of strongly interacting matter.

Due to the sign problem [16], studying QCD on the lattice at a finite chemical potential is exponentially difficult. Nevertheless, several different models approaches [17, 18, 19, 20, 21, 22] indicate that the transition in this region is strongly first-order. Since the first order line originating at zero T cannot end at the vertical axis μ_B = 0, the line must end somewhere in the middle of the diagram [12], there is a hypothetical end-point that has properties of a second-order phase transition, referred to as the QCD CP in this analysis note.

At the QCD CP, the system exhibits critical phenomena, such as a diverging correlation length and critical opalescence, which are associated with the formation of long-range correlations and the emergence of universal behaviour. The first lattice prediction for the location of the QCD CP ($T = 160 \pm 3.5$ MeV and μ_B = 725 $\pm$35 MeV) has been reported in 2002 in Ref. [23]. Existing lattice methods can also be viewed as extrapolations from μ_B = 0, but finite T. There are two promising approaches are developed to determine the location of the QCD CP; one is simulations at finite imaginary values of μ_B [24], and another approach is Taylor expansions around μ_B = 0 [25]. There are many model calculations to predict the location of QCD CP on the phase diagram. From latest lattice QCD calculation [26] suggests that a possible QCD CP in the phase diagram may exist only at temperature,

$$T^{CP}(\mu_B^{CP}) < 130MeV \ , \ \mu_B^{CP} > 400MeV$$

. Also, calculations of the equation of state as a function of T and μ_B have been performed using direct simulations at imaginary chemical potential and calculations using up-to-eighth order Taylor expansions in μ_B. Results of such calculations agree well for $\mu_B/T \leq 2$ - 2.5.

Since there are no conclusive predictions of QCD CP from lattice QCD calculations and

different models. It is necessary to do experimental research in order to determine whether or not the QCD CP exists and, if it exists, where it is located on the QCD phase diagram.

3 Intermittency analysis in high energy physics

Intermittency means random deviations from smooth or regular behaviour [27]. The idea of "intermittency," which was first created in the study of turbulent flow [28], later became very important in the physics of particle production, especially as a way to study fluctuations. In the pioneering article of Bialas and Peschanski [3] introducing intermittency analysis to high-energy physics, it was proposed to study the scaled factorial moments of the multiplicity of particles produced in high-energy collisions as a function of the resolution-size of rapidity interval.
Wosiek found indications of intermittent behavior in the critical region of the two-dimensional Ising model [29]. This raised the general question of whether or not intermittency and critical behavior are related. Satz showed that the critical behavior of the Ising model indeed leads to intermittency, with indices determined by the critical exponents [30]. Later, Bialas and Hwa reported [31] that intermittency parameters could serve as a signal of second-order phase transition in a statistical system. This initiated experimental studies of the structure of the phase transition region via studies of particle multiplicity fluctuations using scaled factorial moments.

3.1 Scaled factorial moments

The use of scaled factorial moments(SFMs) [3] allows one to decrease the statistical bias due to the finite multiplicity of produced particles in a single collision. At the same time, this measure is sensitive to interesting dynamical phenomena such as the emergence of new scales in particle production or the existence of an "intermittent" background, i.e. cascading fluctuations at different scales. Moreover, this method allows one to identify unusually large fluctuations, such as fluctuations in the second-order phase transition. The SFMs, $F_r(M)$ [3]

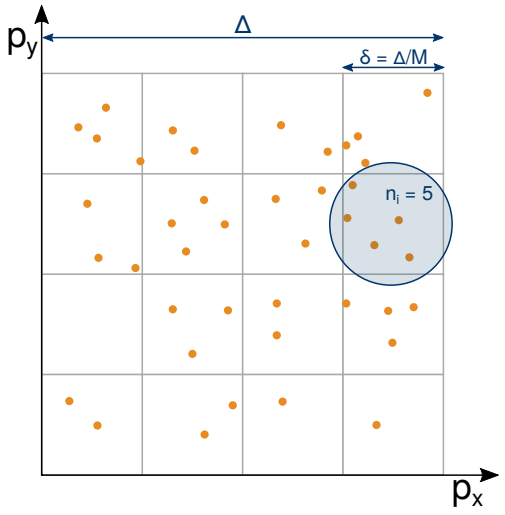

Figure 2: Two-dimensional transverse-momentum space is sub-divided into $M \times M$ number of equally sized bins. The n_i is the particle multiplicity in a given sub-interval, Δ is the momentum region, and δ is bin-width. The figure is taken from Ref. [32]

.

of order (rank) r is defined as:

$$F_r(M) = \frac{\left\langle \frac{1}{M^D} \sum_{i=1}^{M^D} n_i ... (n_i - r + 1) \right\rangle}{\left\langle \frac{1}{M^D} \sum_{i=1}^{M^D} n_i \right\rangle^r} , \tag{1}$$

where M^D is the number of equally-sized subdivision intervals in which the D-dimensional space is partitioned, n_i is the particle multiplicity in a given sub-interval, angle brackets denote averaging over the analyzed events, and Δ is the momentum interval as shown in Fig. 2.

The $F_r(M)$ equals one for all values of r and M^D providing:

(i) multiplicity distribution in Δ is Poissonian,

(ii) particle production is uncorrelated,

(iii) particle density in sub-division space is uniform.

For the ideal gas of particles in the grand-canonical ensemble, these conditions are satisfied in the configuration space, where the particle density is uniform throughout the gas volume, multiplicity fluctuations are Poissonian, and particles are uncorrelated. The momentum distribution is generally non-uniform, and thus, in the momentum space, it is more convenient to use the so-called cumulative variables [33]. By construction, particle density in the cumulative variables is uniformly distributed.

If the dynamics of particle production is scale-invariant, that could be reflected in the power-law behaviour of the SFMs:

$$F_r(M) = F_r(\Delta) \cdot (M^D)^{\phi_r} . \tag{2}$$

The logarithm of SFMs can be written as:

$$log_{10} F_r(M) = \phi_r \cdot log_{10} M^D \; + \; log_{10} F_r(\Delta) . \tag{3}$$

Figure 3 (*left*) shows the linear dependence of the logarithm of SFMs as a function of the logarithm of M^D (for D = 2).

The associated intermittency indices, ϕ_r are predicted [34, 35] to follow the pattern:

$$\phi_r = (r - 1) \cdot (d_r / D), \tag{4}$$

with d_r, the so-called anomalous fractal dimension of the set formed by the order parameter density fluctuations. Figure 3 (*right*) shows linear dependence of ϕ_r on *r*.

For the monofractal set, d_r is independent of r, and it is related to the corresponding fractal dimension, d_F, through the relation, $d_r = D - d_F$. Such behaviour is analogous to critical opalescence in conventional matter [36]. This initiated experimental studies of the structure of the phase transition region via studies of particle multiplicity fluctuations using SFMs.

A systematic search for QCD critical fluctuations has been performed by the NA61/SHINE collaborations at CERN SPS with measurements of intermittency in A+A collisions. For the first time, a systematic two-dimensional scan of system size and collision energy was done. The recent results from the NA61/SHINE Collaboration on QCD CP search in ^{40}Ar + ^{45}Sc collisions at 150*A* GeV/*c* via proton intermittency analysis using cumulative variables and statistically independent data points are reported in Ref [37]. Following this study, the NA61/SHINE Collaboration continues the systematic search for the QCD CP via proton intermittency analysis. The results on of Ar+Sc and Pb+Pb collisions [38] will be reported in this analysis note.

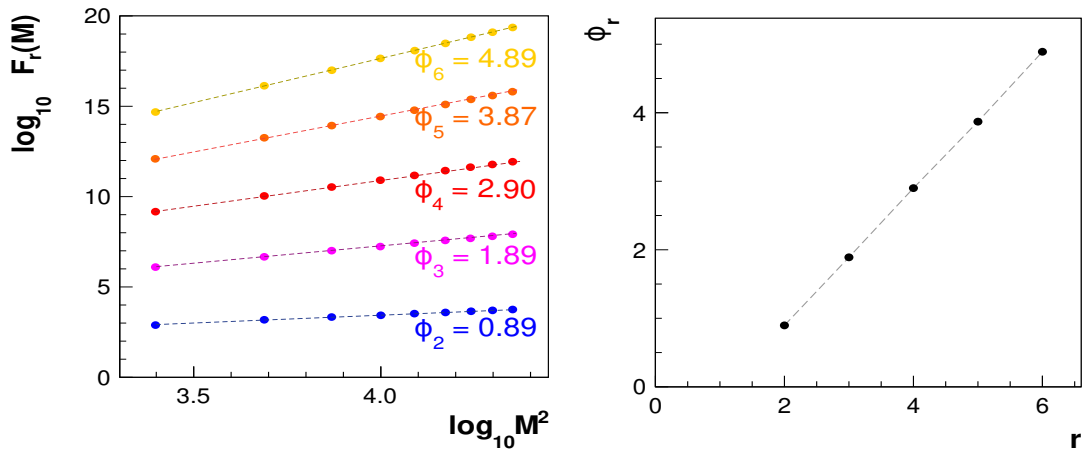

Figure 3: *Left:* the log-log plot of the scaled factorial moments of order $r = 2, 3, 4, 5, 6$ (full-color circles) from the Power-Law model and also intermittency indices (ϕ_2, ϕ_3, ϕ_4, ϕ_5, ϕ_6) values are shown. *Right:* linear dependence of intermittency indices on the order of moments, r are shown [32].

4 NA61/SHINE experiment

The NA61/SPS Heavy Ion and Neutrino Experiment [39], also known as the SHINE experiment, is situated in the North Area of CERN and is a fixed-target experiment on the H2 beamline of the Super Proton Synchrotron (SPS) accelerator. NA61/SHINE is a versatile experimental facility constructed to study hadron production in hadron-proton, hadron-nucleus, and nucleus-nucleus collisions. The long-term advancement of the proton and ion sources at CERN, the accelerator chain, and the H2 beamline in the CERN North Area has tremendously benefited the NA61/SHINE experiment. NA61/SHINE projected from the equipment inherited from its predecessors [40], specifically the NA49 experiment [41]. The ^{40}Ar+^{45}Sc and ^{208}Pb + ^{208}Pb

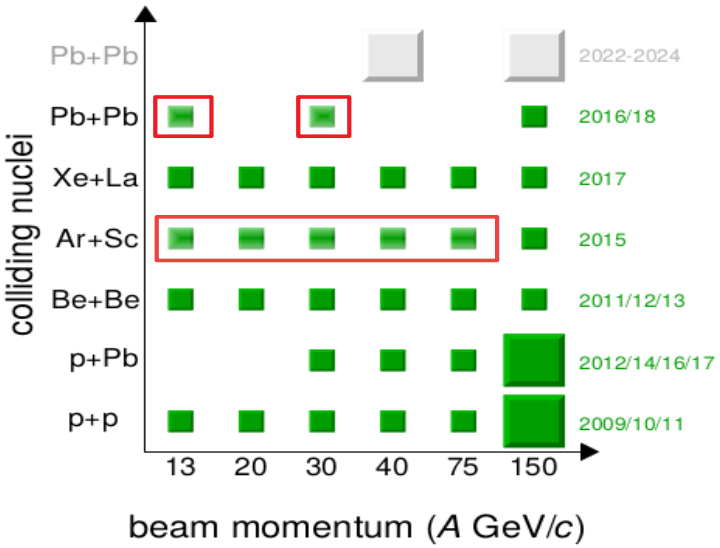

Figure 4: An overview of the NA61/SHINE's system size and collision energy scan. The boxes show the already taken data, and the large boxes mark systems for which large statistics were obtained. The Ar+Sc and Pb+Pb data sets, demonstrated by red boxes, are being studied, and proton intermittency results are presented in this analysis note.

data sets marked by the red box in Fig. 4 were analyzed and results are reported in this analysis note.

4.1 Overview of the NA61/SHINE detector

The layout of the NA61/SHINE large-acceptance hadron spectrometer [40] before LS2 is presented in Fig. 5. The core components of the setup are four large-volume Time Projection Chambers (TPCs): VTPC-1, VTPC-2, MTPC-L, and MTPC-R. TPCs are the main tracking

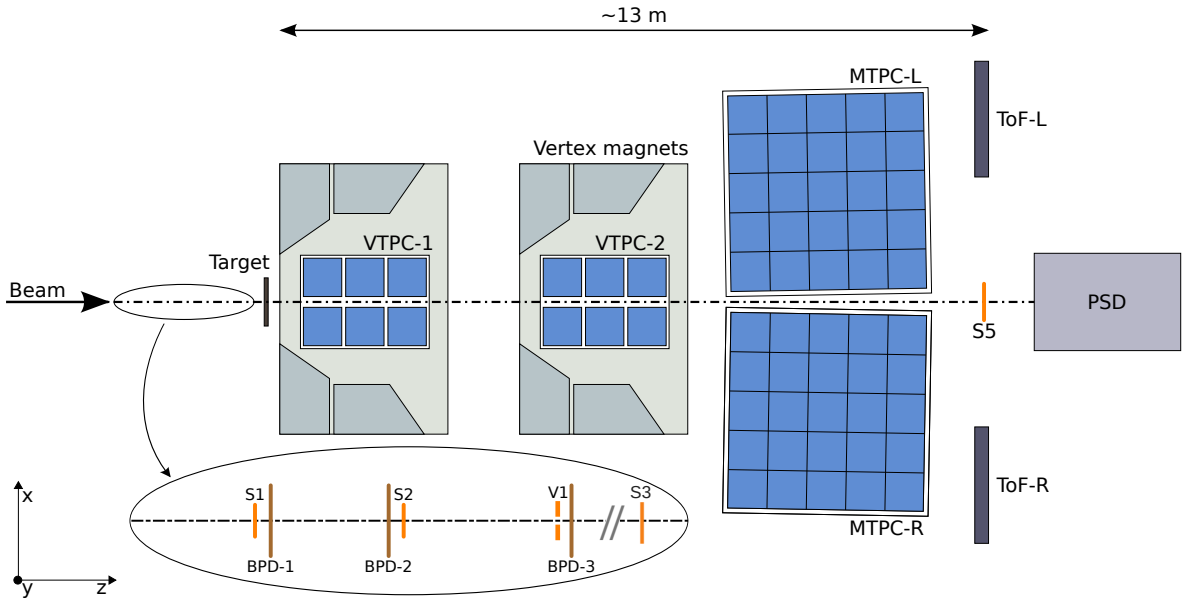

Figure 5: An illustration showing the NA61/SHINE detector setup (not to scale). The four Time Projection Chambers (TPCs) are important. The inside of superconducting magnets contains VTPCs. Two Time of Flight (ToF) walls are located downstream of the MTPCs. The Projectile Spectator Detector (PSD) is on the far right. The figure is taken from Ref. [40].

devices of the NA61/SHINE spectrometer. Two Time of Flight detectors, ToF-L and ToF-R, are placed downstream of the MTPCs. The purpose of the ToF detectors is to improve particle identification capabilities. Another NA61/SHINE spectrometer component is the Projectile Spectator Detector (PSD), which measures the energy of projectile spectators (nucleons and nuclear fragments). The superconducting magnets, large-volume TPCs, and TOF-L/R detectors were inherited from the NA49 experiment. The ^{40}Ar+^{45}Sc data were registered at six beam momenta: p_{beam} = 13*A*, 19*A*, 30*A*, 40*A*, 75*A*, and 150*A* GeV/*c*. A similar beam and detector configuration was used during the ^{40}Ar+^{45}Sc data-taking campaign. They only differ by a magnetic field, which was reduced proportionally to the beam momentum and the PSD position. Later upgraded beam and detector configuration was used for ^{208}Pb + ^{208}Pb at 13*A*, 30*A*, and 150*A* GeV/*c* data-taking during the 2016 data-taking campaign. The key components of the NA61/SHINE facility relevant to this work is discussed in Ref. [40].

4.1.1 Triggering systems

The NA61/SHINE trigger system uses analog signals from beam detectors (BPDs are not included) to classify events and limit stored data, when, for instance, an interaction with a target did not take place. It can include any signal arriving up to ≈300 ns after the S1 signal and has four independent trigger configurations (T1-T4). The Projectile Spectator Detector

also contributes to the trigger logic in veto mode. Collimators in the beam line were adjusted to obtain beam rates of $\approx 10^4/s$ during the $\approx$ 10 s spill and a super-cycle time of 32.4 s. Trigger definitions used during the ^{40}Ar + ^{45}Sc and ^{208}Pb + ^{208}Pb data taking are presented in Table 1.

Table 1: Trigger definitions used during the ^{40}Ar+^{45}Sc and ^{208}Pb + ^{208}Pb data-taking campaign.

Trigger	Description	Definition		Fraction of data	
		Ar+Sc	Pb+Pb	Ar+Sc	Pb+Pb
T3	unidentified beam	S1 · S2	S1 · S2	0.18%	0.80%
T1	identified beam	T3 · $\overline{\text{V1}}$	T3 · $\overline{\text{V1}}$	1.16%	10.4%
T4	unidentified beams interaction	T1 · $\overline{\text{S5}}$	T1 · $\overline{\text{S3}}$	7.13%	67.13%
T2	identified beams interaction	T4 · $\overline{\text{PSD}}$	T4 · $\overline{\text{PSD}}$	92.61%	21.61%

After the T1-T4 signals are generated, they are sent to the prescaler module. The role of the module is to select a given fraction of triggers of a given type for recording.

5 Event selection

The sub-sample consisting of central interactions of beam-ions ^{40}Ar (or ^{208}Pb) with ^{45}Sc (or ^{208}Pb) target nuclei selected on the trigger level - T2 trigger – was analyzed. A sequence of event selection criteria was imposed on the T2 trigger sample, ensuring the highest quality of the analyzed data and proper, well-defined event *centrality* interval. There are two sets of event selection criteria, upstream or non-biasing cuts and downstream or biasing cuts. Also, before the physical event selection of target-inserted data sets, a subset of events has to be excluded due to malfunctioning of PSD and/or other detectors. List of event selection criteria for ^{208}Pb + ^{208}Pb collisions at beam momentum of 13*A* and 30*A* GeV/*c* and ^{40}Ar + ^{45}Sc collisions at beam momenta of 13*A*-75*A* GeV/*c* is summarized in Table 8 and Table 9.

5.1 Target inserted data

The target used in ^{40}Ar + ^{45}Sc data-taking of the NA61/SHINE experiment was a stack of six square ^{45}Sc plates of 2.5×2.5 cm^2 area and 1 mm thickness. During the ^{208}Pb + ^{208}Pb data-taking campaign, a square ^{208}Pb plate, with an area of 2.5×2.5 cm^2 and a thickness of 1 mm was utilized as a target. The targets were placed about 80 cm upstream of the VTPC-1. The targets were mounted in a special target holder device, providing a helium atmosphere around the target to minimize interactions of beam particles with air surrounding the target. A pneumatic movement system is used to remove or insert the target in the beam, allowing easy data collection with and without the target. The data were taken using two target configurations: target inserted (target IN) and target removed (target R). Approximately 90% of accumulated statistics were collected with target IN. A summary of target IN and target R statistics of the collected Ar+Sc and Pb+Pb data is summarized in Table. 2. The target R data was collected to correct for interactions of beam particles with the material surrounding the target (off-target interactions).

The purity of the ^{45}Sc and ^{208}Pb target was measured [42] at Jan Kochanowski University in Kielce, Poland using the WDXRF method [43]. The content of ^{45}Sc in the ^{45}Sc target and ^{208}Pb in the ^{208}Pb target was about 99.3% and 99.4%, respectively.

Table 2: A summary of target IN and target R statistics of the collected Ar+Sc and Pb+Pb data

Beam momentum (GeV/c)	Target IN	Target R
Ar+Sc data sets		
13A	$3.59 \cdot 10^6$	$2.32 \cdot 10^5$
19A	$3.70 \cdot 10^6$	$2.34 \cdot 10^5$
30A	$4.83 \cdot 10^6$	$2.64 \cdot 10^5$
40A	$8.91 \cdot 10^6$	$8.75 \cdot 10^5$
75A	$4.37 \cdot 10^6$	$2.94 \cdot 10^5$
Pb+Pb data sets		
13A	$2.67 \cdot 10^6$	$9.43 \cdot 10^5$
30A	$4.69 \cdot 10^6$	$1.35 \cdot 10^6$

5.2 Selection of runs

Sets of runs and events that have to be excluded due to instabilities with PSD and/or other detectors (stability of target in runs was checked). For ^{40}Ar + ^{45}Sc collisions at beam momentum of 13A GeV/c data sets of run and partial events from specified runs are excluded mentioned in Table 3. For 19A GeV/c (see Table 4), and 75A GeV/c (see Table 5) data sets of run and partial events from specified runs are excluded from further analysis. For ^{208}Pb + ^{208}Pb at beam momentum of 30A GeV/c data, sets of run and partial events from specified runs (see Table 6) are excluded from further analysis.

Table 3: Set of runs with event id of recorded ^{40}Ar + ^{45}Sc collisions at 13A GeV/c (026_17c_v1r7p0_pA_slc6_phys) are identified as bad runs due to PSD malfunction. All events from these runs (20532, 20534, 20535, 20537, 20538, 20539, 20540, 20541, 20544, 20545, 20550) are excluded from further analysis.

runs	events
20576	10300-26100
20615	15000-80000
20629	30000-90000

Table 4: Set of runs with event id of recorded ^{40}Ar + ^{45}Sc collisions at 19A GeV/c (028_17c_v1r7p0_pA_slc6_phys) are identified as bad runs due to PSD malfunction.

runs	event id
20798	40000-110000

Table 5: Set of runs with event id of recorded ^{40}Ar + ^{45}Sc collisions at 75A GeV/c (026_17b_v1r6p0_pA_slc6_phys) are identified as bad runs due to PSD malfunction.

runs	event id
21465	12300-19200
21563	42800-43600

Table 6: Set of runs with event id of recorded ^{208}Pb + ^{208}Pb collisions at 13*A* GeV/*c* (026_17b_v1r6p0_pA_slc6_phys) are identified as bad runs due to PSD malfunction. All events from these runs (26456, 26457, 26458, 26580, 26758, 26759, 26760, 26769, 26770, 26771, 26772, 26773, 26774, 26775, 26776, 26777, 26778, 26779, 26780, 26781, 26782, 26800, 26801) are excluded from further analysis.

runs	event id
26454	5100-6500
26488	57000-63000
26496	22000-30000
26593	2500-6000
26607	9500-13000
26608	0-2000
26619	5500-6500
26620	0-4000
26671	0-6500
26637	16500-17600
26720	5700-6200
26722	1000-2500
26723	1000-12000
26725	0-8500
26726	0-36000
26727	0-6000
26728	0-57000
26729	0-34000
26839	40000-45000
26840	0-2200
26841	0-4800
26842	0-1200
26843	0-3700
26863	16800-21500
26865	44000-61000

Table 7: A summary of good run and event selection of ^{40}Ar + ^{45}Sc collisions

p_{beam} (GeV/*c*)	#target IN events	#good run events
Ar+Sc data sets		
13*A*	$3.61 \cdot 10^6$	$3.02 \cdot 10^6$
19*A*	$3.65 \cdot 10^6$	$3.64 \cdot 10^6$
30*A*	$4.79 \cdot 10^6$	$4.79 \cdot 10^6$
40*A*	$1.05 \cdot 10^7$	$1.05 \cdot 10^7$
75*A*	$4.37 \cdot 10^6$	$4.36 \cdot 10^6$

5.2.1 T2 event selection

The sub-sample consisting of central interactions of beam-ions ^{40}Ar (or ^{208}Pb) with ^{45}Sc (or ^{208}Pb) target nuclei selected on the trigger level - T2 trigger (to select central and semi-central collisions) – was analyzed.

Table 8: List of event selection criteria for ^{40}Ar + ^{45}Sc collisions at beam momentum of 13*A*-75*A* GeV/*c*, see text for details.

p_{beam}(GeV/*c*)	13*A*	19*A*	30*A*	40*A*	75*A*
$\sqrt{s_{NN}}(GeV)$	5.12	6.12	7.62	8.77	11.9
1) Bad runs	✓	✓	✓	✓	✓
2) T2 trigger cut	✓	✓	✓	✓	✓
3) Time stability	✓	✓	✓	✓	✓
4) Target inserted	✓	✓	✓	✓	✓
List of Non-biasing event cuts					
5) WFA beam:	4μs	4μs	4μs	4μs	4μs
6) WFA interaction:	25μs	25μs	25μs	25μs	25μs
7) Beam BPD Fit	✓	✓	✓	✓	✓
8) BPD3 Charge X (min, max)	3000, 7900	3500, 6500	3400, 7400	3500, 8000	3800, 7200
9) BPD3 Charge Y (min, max)	2500, 6800	3200, 6000	2800, 6600	3000, 7000	3600, 6800
List of Biasing event cuts					
10) Fitted Vtx Presence:	✓	✓	✓	✓	✓
11) Vtx Fit Quality	✓	✓	✓	✓	✓
12) Vtx position Z	$\pm$ 2 cm	$\pm$ 2 cm	$\pm$ 2 cm	$\pm$ 2 cm	$\pm$ 2 cm
List of PSD and/or detector malfunction event cuts					
13) Small modules ($E_{PSD}^{max}(GeV)$)	200 GeV	350	600	900	1300
14) Large module ($E_{PSD}^{min}(GeV)$, $E_{PSD}^{max}(GeV)$)	$\times$	20, 500	100, 1000	200, 1000	300, 1700
15) Track ratio ($\frac{nTrInVtxFit}{nTracks}$, nTrInVtxFit)	0.06, 7	0.1, 11	0.1, 13	0.13, 16	0.17, 31
16) S5 cloud cut ($E_{PSD}^{max}(GeV)$, NTrInFit)	320, 50	500, 50	850, 100	1200, 140	2200, 160
17) E_{PSD} vs allTracks ($E_{PSD}^{max}(GeV)$, all tracks)	380, 70	620, 95	$\times$	$\times$	$\times$

Table 9: List of event selection criteria for ^{208}Pb + ^{208}Pb collisions at beam momentum of 13*A*, and 30*A* GeV/*c*, see text for details.

p_{beam}(GeV/*c*)	13*A*	30*A*
$\sqrt{s_{NN}}(GeV)$	5.12	7.62
1) Bad runs	✓	✓
2) T2 trigger cut	✓	✓
3) Time stability	✓	✓
4) Target inserseted	✓	✓
List of Non-biasing event cuts		
5) WFA beam:	25μs	25μs
6) WFA interaction:	×	×
7) Beam BPD Fit	✓	✓
8) BPD3 Charge X (min, max)	2307, 7697	2000, 8408
9) BPD3 Charge Y (min, max)	2400, 6450	2150, 6650
List of Biasing event cuts		
10) Fitted Vtx Presence:	✓	✓
11) Vtx Fit Quality	✓	✓
12) Vtx position Z	$\pm$ 1 cm	$\pm$ 1 cm
List of PSD malfunction event cuts		
13) Small modules $_{(E_{PSD}^{max}(GeV))}$	×	×
14) Large module, $_{(E_{PSD}^{min}(GeV),\ E_{PSD}^{max}(GeV))}$	×	×
15) Track ratio ($_{\frac{nTrInVtxFit}{nTracks}}$, nTrInVtxFit)	×	×
16) S5 cloud cut $_{(E_{PSD}^{max}(GeV)}$, NTrInFit)	×	×
17) E_{PSD} vs allTracks $_{(E_{PSD}^{max}(GeV)}$, all tracks)	×	×

5.3 Non-biasing event selection

The upstream of the target or non-biasing cuts do not employ interaction-dependent variables. They reduce the number of unwanted events without influencing properties of wanted events. These are cuts on the beam's position, composition, and timing.

5.3.1 Beam quality

A precise measurement of the beam particle trajectory was needed for the determination of the interaction. The presence of the signal from BPD-3, together with a signal from either of the other beam position detectors (BPD-1 or BPD-2), was required. Such conditions allow the fitting of the beam trajectory and its extrapolation to the target area. Furthermore, it also assures that the beam particle did not interact upstream of BPD-3. Examples of beam position distributions for ^{208}Pb + ^{208}Pb collisions at beam momentum of 13*A* and 30*A* GeV/*c* and ^{40}Ar + ^{45}Sc collisions at beam momentum of 75*A* GeV/*c* are shown in Figs. 6- 12, respectively. The *left* and *right* distributions are represented before and after the beam quality cut, respectively.

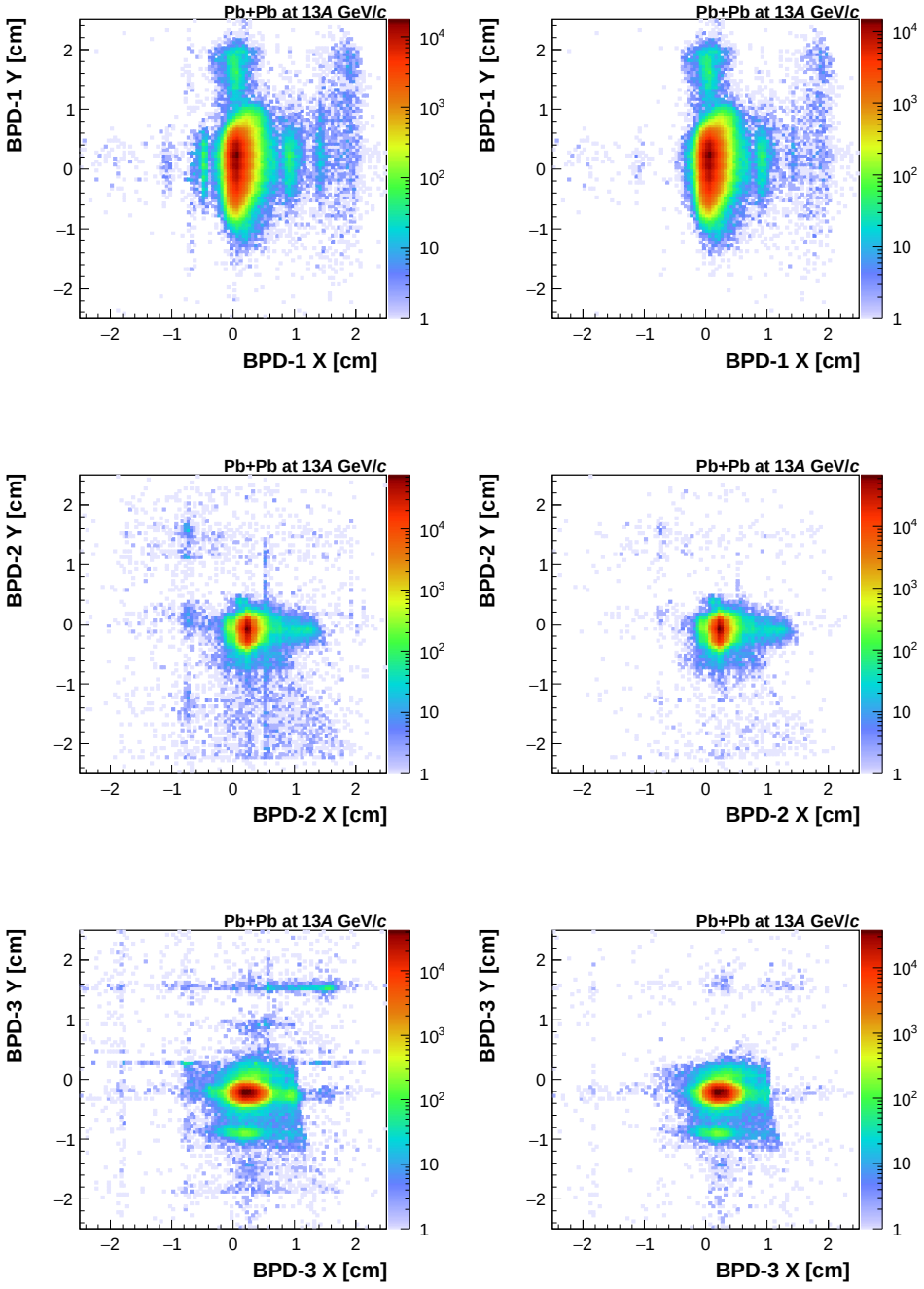

Figure 6: Distributions of BPDs position for ^{208}Pb + ^{208}Pb collisions at 13*A* GeV/*c*. *Left*: BPD1 (*top*), BPD2 (*middle*), and BPD3 (*bottom*) position distribution before the standard BPD cut. *Right*: BPD1 (*top*), BPD2 (*middle*), and BPD3 (*bottom*) position distribution after the standard BPD cut.

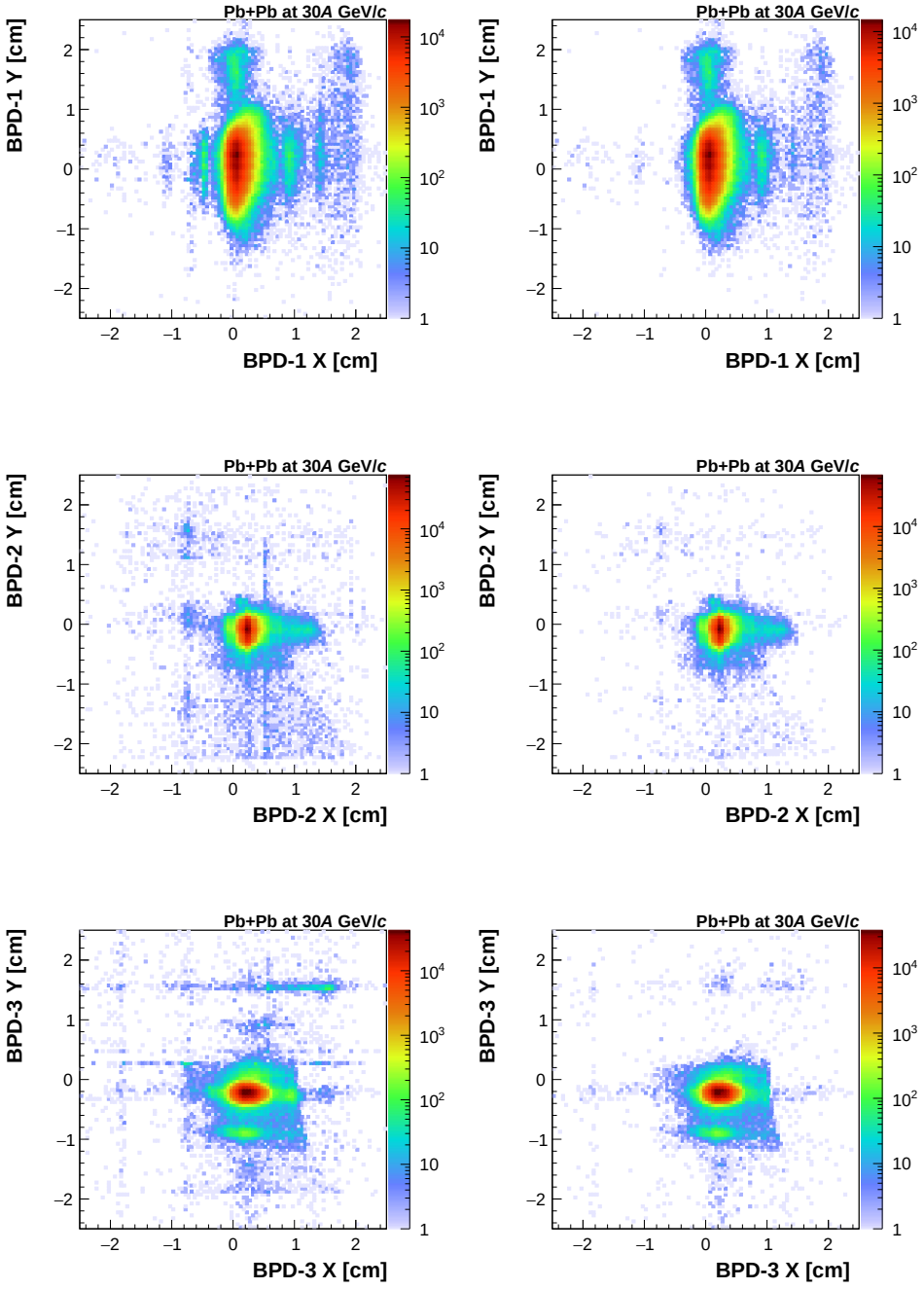

Figure 7: Distributions of BPDs position for ^{208}Pb + ^{208}Pb collisions at 30*A* GeV/*c*. *Left*: BPD1 (*top*), BPD2 (*middle*), and BPD3 (*bottom*) position distribution before the standard BPD cut. *Right*: BPD1 (*top*), BPD2 (*middle*), and BPD3 (*bottom*) position distribution after the standard BPD cut.

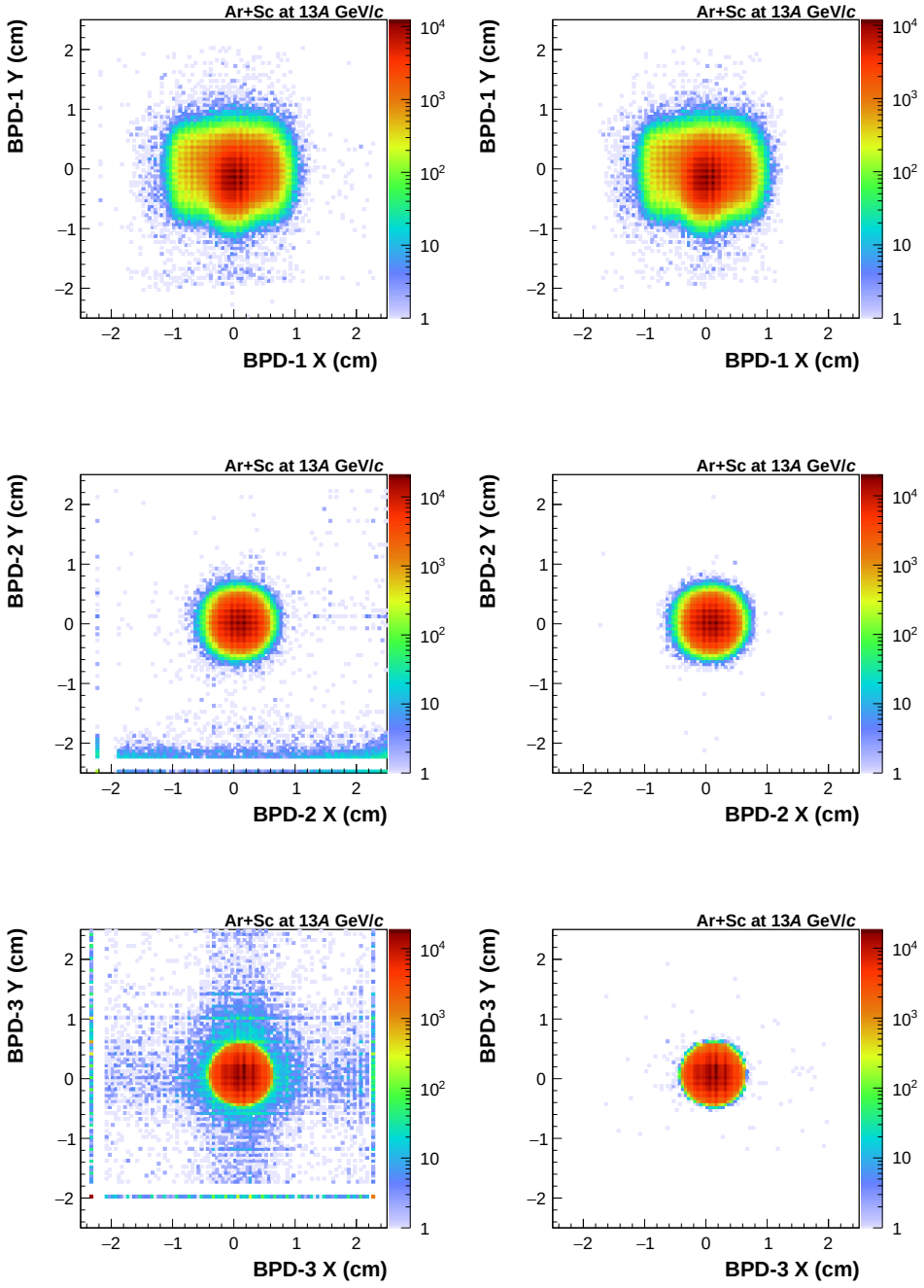

Figure 8: Distributions of BPDs position for ^{40}Ar + ^{45}Sc collisions at 13*A* GeV/*c*. *Left*: BPD1 (*top*), BPD2 (*middle*), and BPD3 (*bottom*) position distribution before the standard BPD cut. *Right*: BPD1 (*top*), BPD2 (*middle*), and BPD3 (*bottom*) position distribution after the standard BPD cut.

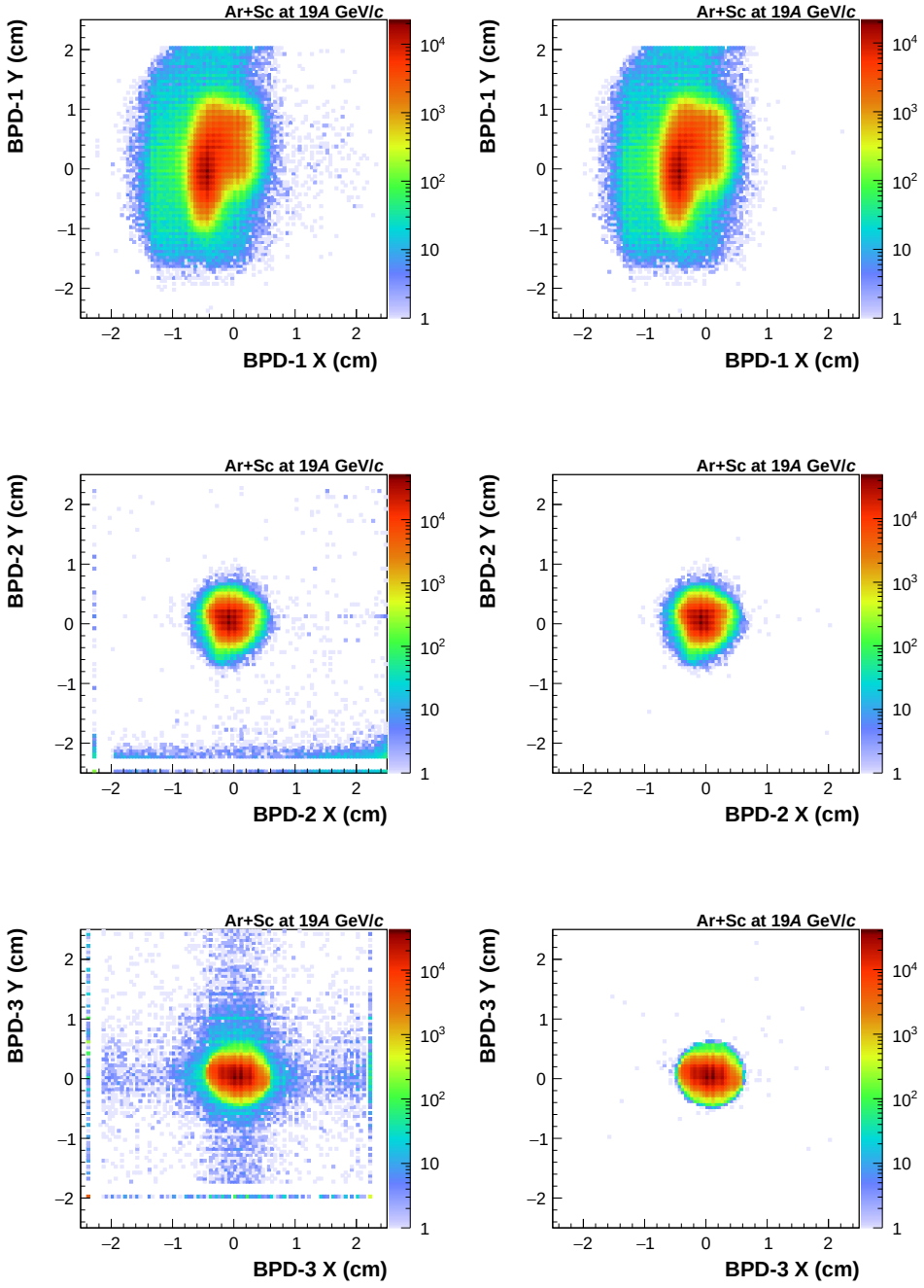

Figure 9: Distributions of BPDs position for ^{40}Ar + ^{45}Sc collisions at 19*A* GeV/*c*. *Left*: BPD1 (*top*), BPD2 (*middle*), and BPD3 (*bottom*) position distribution before the standard BPD cut. *Right*: BPD1 (*top*), BPD2 (*middle*), and BPD3 (*bottom*) position distribution after the standard BPD cut.

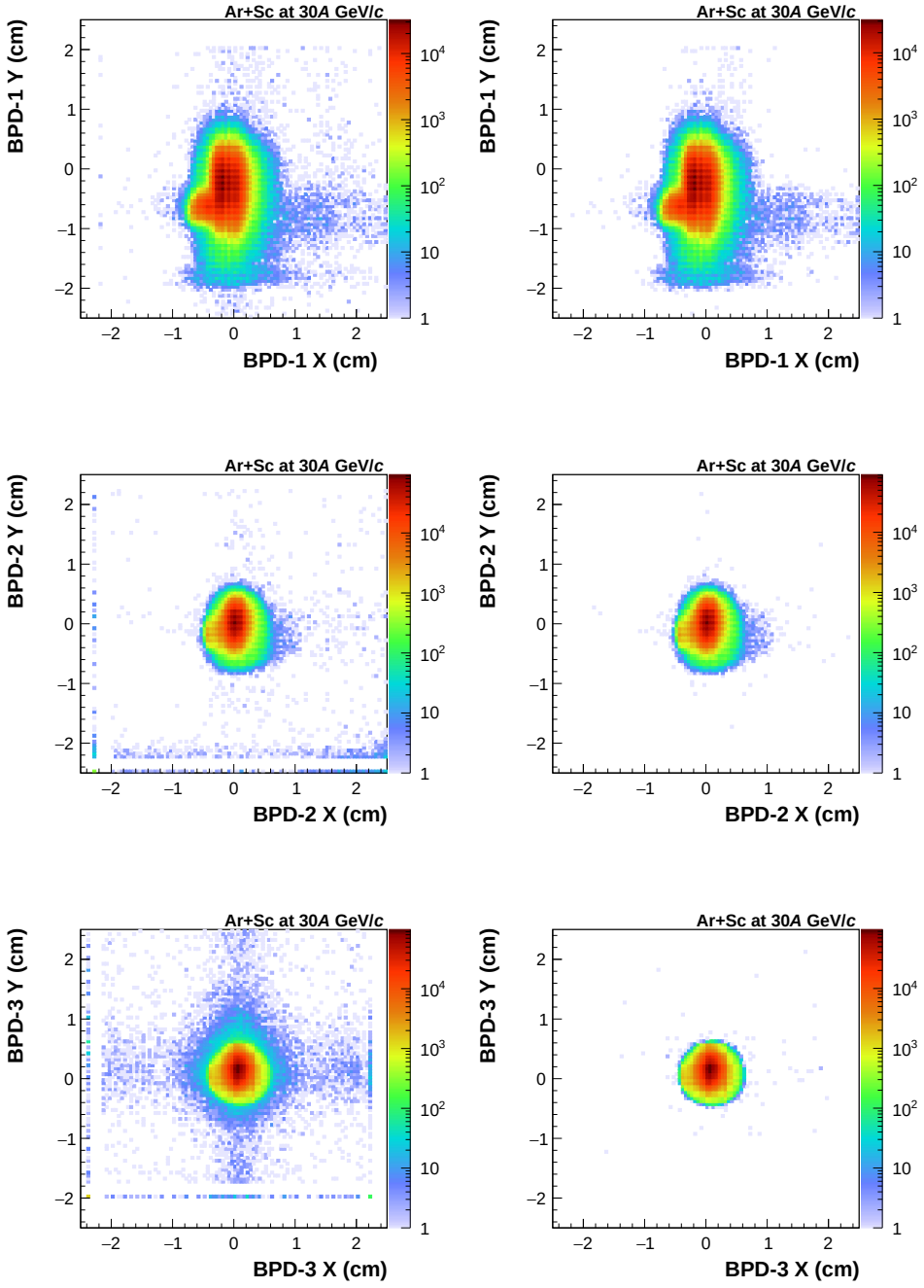

Figure 10: Examples distributions of BPDs position for ^{40}Ar + ^{45}Sc collisions at 30*A* GeV/*c*. *Left*: BPD1 (*top*), BPD2 (*middle*), and BPD3 (*bottom*) position distribution before the standard BPD cut. *Right*: BPD1 (*top*), BPD2 (*middle*), and BPD3 (*bottom*) position distribution after the standard BPD cut.

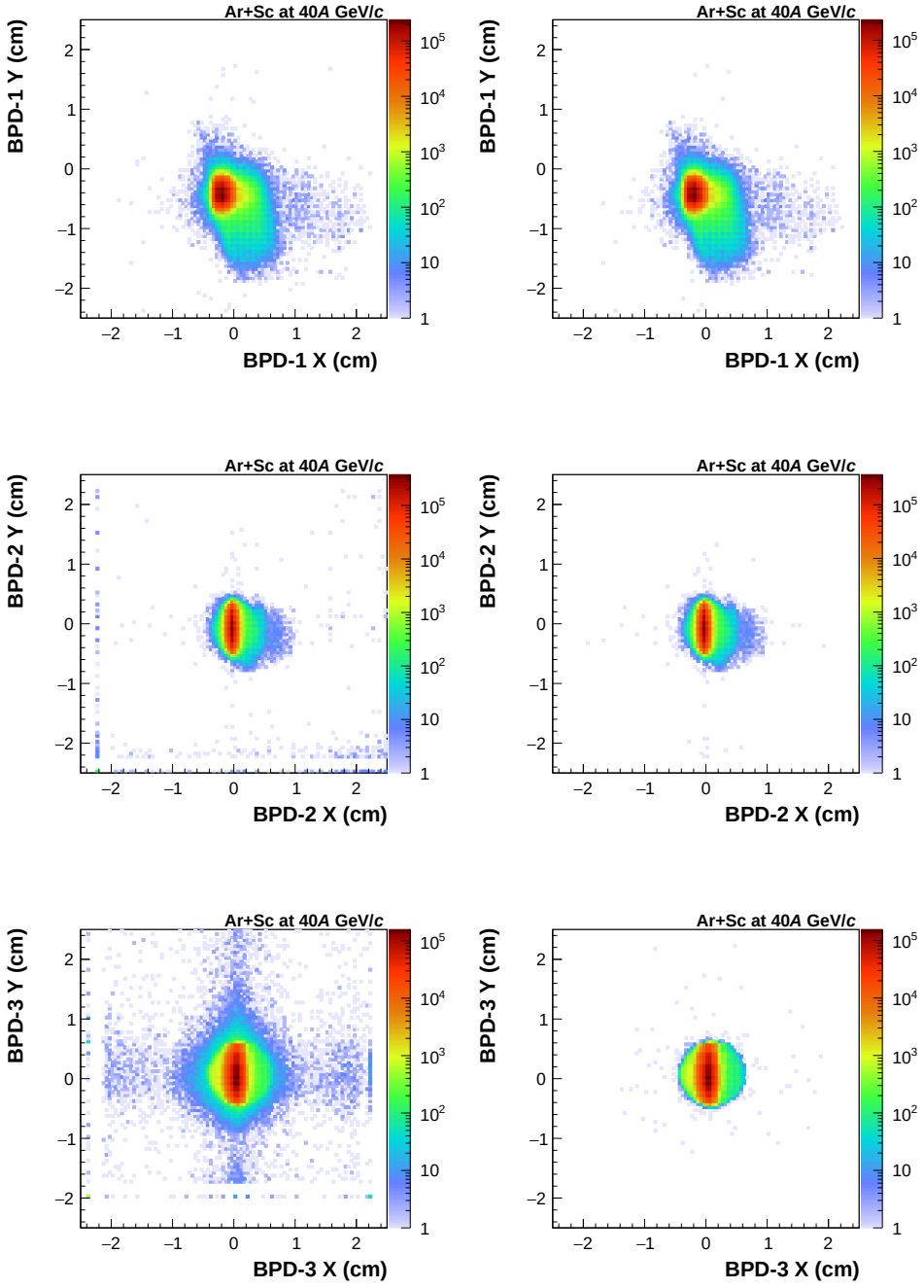

Figure 11: Distributions of BPDs position for ^{40}Ar + ^{45}Sc collisions at 40*A* GeV/*c*. *Left*: BPD1 (*top*), BPD2 (*middle*), and BPD3 (*bottom*) position distribution before the standard BPD cut. *Right*: BPD1 (*top*), BPD2 (*middle*), and BPD3 (*bottom*) position distribution after the standard BPD cut.

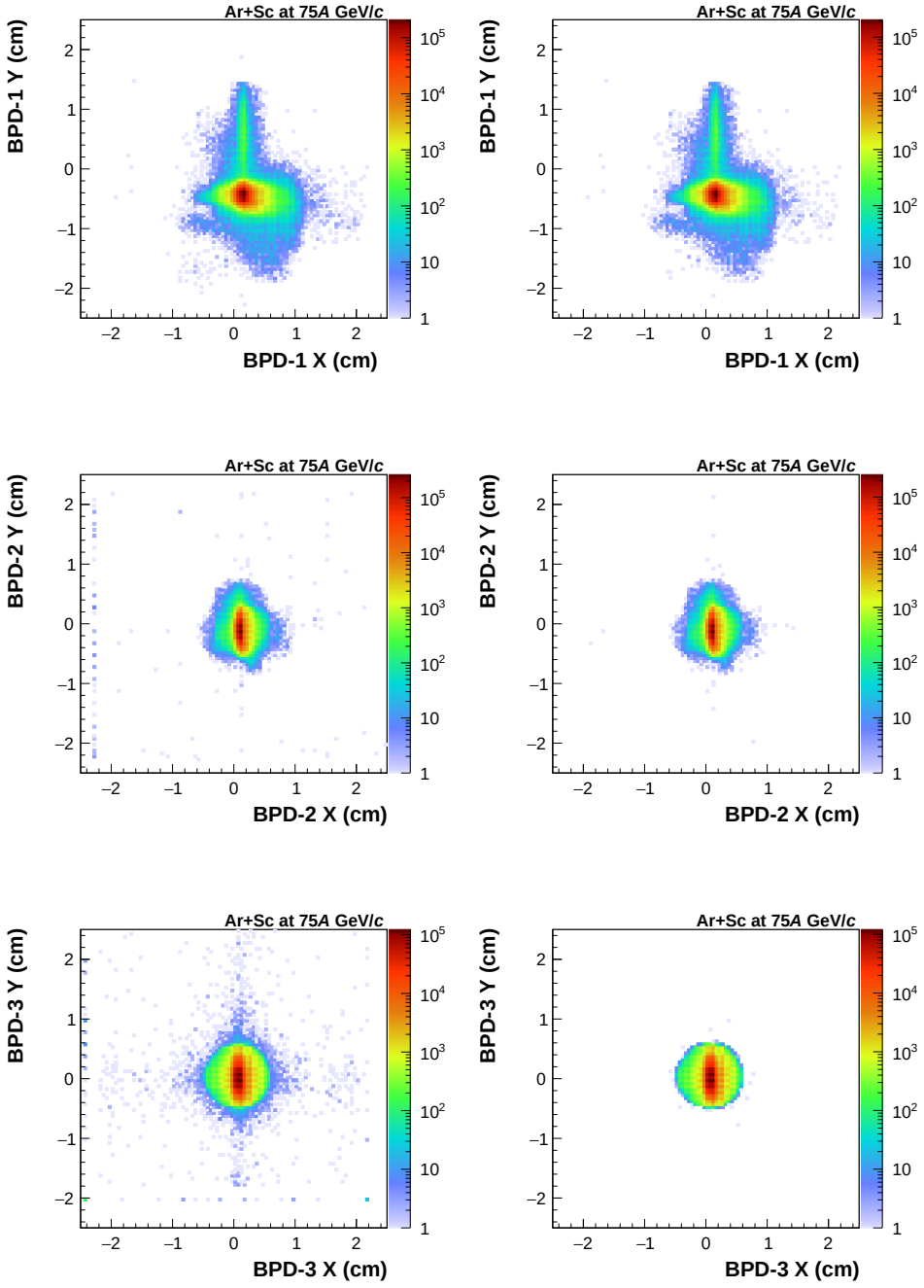

Figure 12: Distributions of BPDs position for ^{40}Ar + ^{45}Sc collisions at 75*A* GeV/*c*. *Left*: BPD1 (*top*), BPD2 (*middle*), and BPD3 (*bottom*) position distribution before the standard BPD cut. *Right*: BPD1 (*top*), BPD2 (*middle*), and BPD3 (*bottom*) position distribution after the standard BPD cut.

5.3.2 BPD3 charge

Additional information is provided to verify the charge of the beam ions measured by the BPD-3 counter. Example distributions of the charge signal obtained on x and y planes of BPD-3 for ^{208}Pb + ^{208}Pb collisions at beam momentum of 13*A*, 30*A* (Fig. 13) and ^{40}Ar + ^{45}Sc collisions at beam momentum of 13*A*- 75*A* GeV/*c* are shown in Fig. 14. In both distributions, the red rectangular region represents the region selected for these analyses. The upper and lower limits of the BPD-3 charge used to select events for ^{208}Pb + ^{208}Pb and ^{40}Ar + ^{45}Sc data sets are summarized in Table 10.

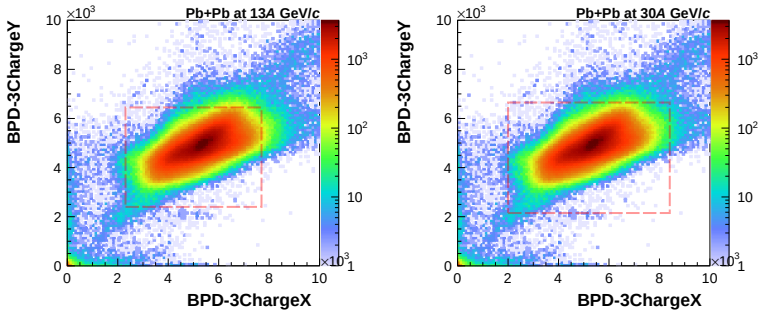

Figure 13: Distributions of BPD3 *X* and *Y* charge for ^{208}Pb + ^{208}Pb collisions at beam momentum of 13*A* and 30*A* GeV/*c*. The dotted rectangular regions represent the select by the BPD3 charge selection criteria.

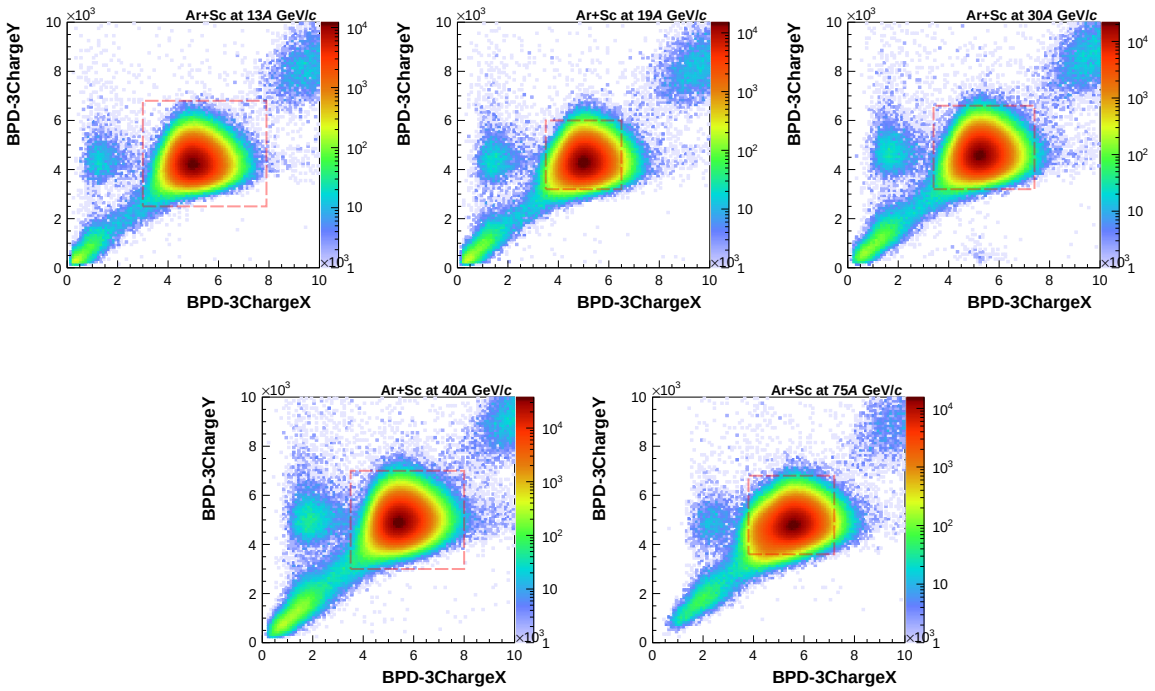

Figure 14: Distributions of BPD3 *X* and *Y* charge for ^{40}Ar + ^{45}Sc collisions at beam momenta of 13*A*-75*A* GeV/*c*. The dotted rectangular regions represent the select by the BPD3 charge selection criteria.

Table 10: The BPD3 charge cut values used to select events for ^{208}Pb + ^{208}Pb collisions at beam momenta of 13*A* and 30*A* GeV/*c* and ^{40}Ar + ^{45}Sc collisions at beam momenta of 13*A*-75*A* GeV/*c*.

	BPD-3 charge X		BPD-3 charge Y	
p_{beam} (GeV/*c*)	lower limit	upper limit	lower limit	upper limit
^{208}Pb + ^{208}Pb data sets				
13*A*	2307	7697	2400	6450
30*A*	2000	8408	2150	6650
^{40}Ar + ^{45}Sc data sets				
13*A*	3000	7900	2500	6800
19*A*	3500	6500	3200	6000
30*A*	3400	7400	2800	6600
40*A*	3500	8000	3000	7000
75*A*	3800	7200	3600	6800

5.3.3 Beam particles off-time

This criterion reduces the contribution of events in which there was an additional beam particle that could interact with the target or the detector material in close time proximity to the triggering particle. If it is too close in time, it may be mistaken for the product of the collision or may interact with the target producing a second collision that is indistinguishable by the reconstruction software. Such events may bias the fluctuation measurements. The main selection tool is the distribution of the time in which beam particles pass through the S1 counter (see Ref. [40]) with respect to the trigger signal (generated by the interaction beam ion). This selection criteria usually refer to the WFA (WaveForm Analyzer) cut.

In the ^{208}Pb + ^{208}Pb event selection, the WFA cut selects events with no off-time beam particle within the $\pm$ 25 μs window with respect to the trigger particle S1 signal. In the ^{40}Ar + ^{45}Sc event selection, the WFA cut selects events with no off-time beam particle within the $\pm$ 4 μs window with respect to trigger particle S1 signal. Additionally, no off-time particle which gives the T4 signal (see Ref. [40]) can be detected within the $\pm$ 25 μs window.

Example distributions of beam particles time measured by the S1 counter (see Figs. 15 and 17) and obeying the T4 trigger (see Figs. 16 and 18) with respect to a trigger signal in target-inserted ^{208}Pb + ^{208}Pb collisions at beam momentum of 13A and 30A GeV/c and ^{40}Ar + ^{45}Sc collisions at beam momentum of 13A-75A GeV/c are shown. The blue line with blue-shaded beam particles time distributions represents before the WFA cut and the red line with red-shaded beam particles time distributions represents after the WFA cut.

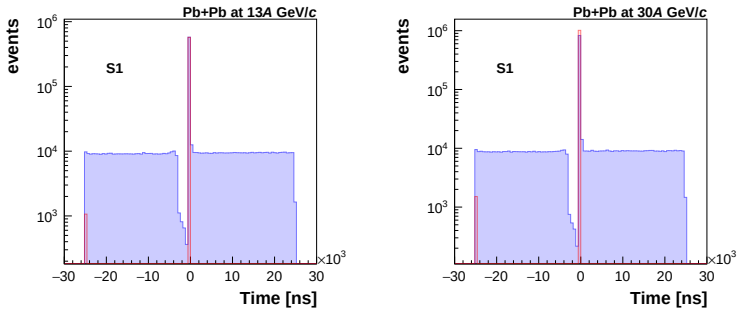

Figure 15: Example distributions of beam particles time measured by the S1 counter with respect to a trigger signal in target-inserted ^{208}Pb + ^{208}Pb collisions at beam momentum of 13A and 30A GeV/c are shown. The blue line with blue-shaded distributions and the red line with red-shaded distributions are before and after the WFA cut.

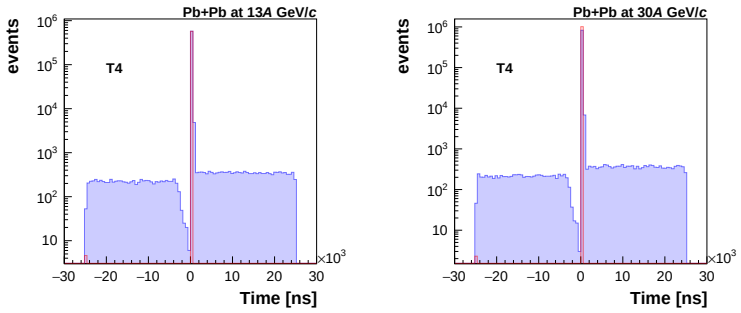

Figure 16: Example distributions of beam particles time measured by the T4 counter with respect to a trigger signal in target-inserted ^{208}Pb + ^{208}Pb collisions at beam momentum of 13A and 30A GeV/c are shown. The blue line with blue-shaded distributions and the red line with red-shaded distributions are before and after the WFA cut.

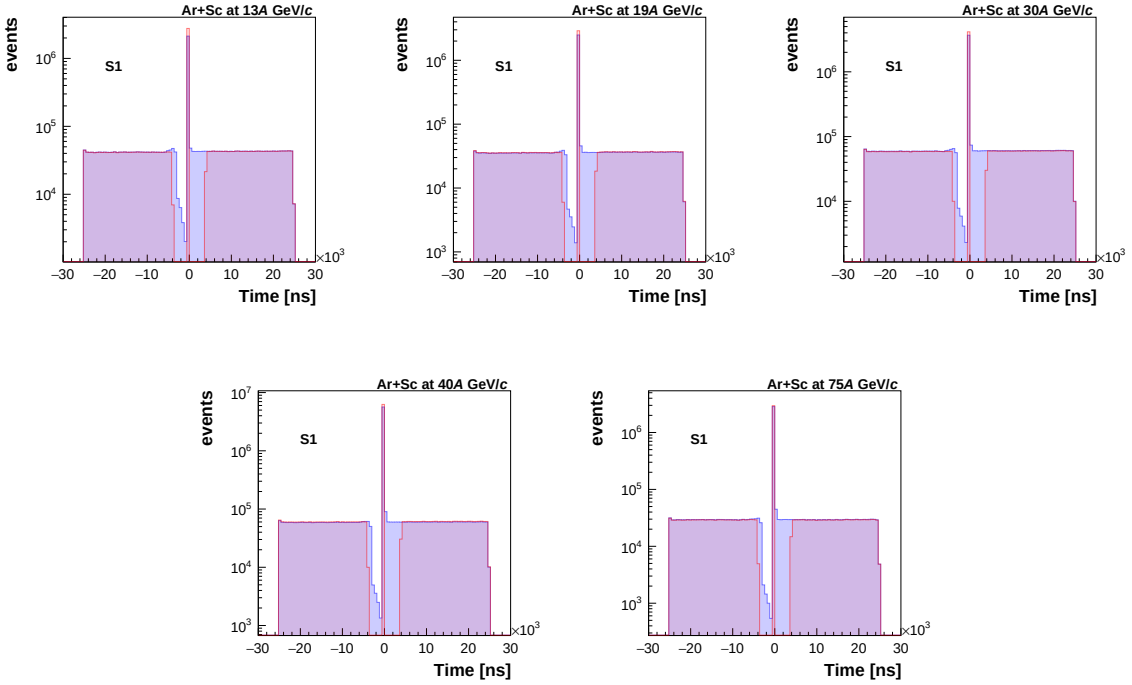

Figure 17: Distributions of beam particles time measured by the S1 counter with respect to a trigger signal in target-inserted ^{40}Ar + ^{45}Sc collisions at beam momenta of 13A-75A GeV/c are shown. The blue line with blue-shaded distributions and the red line with red-shaded distributions are before and after the WFA cut.

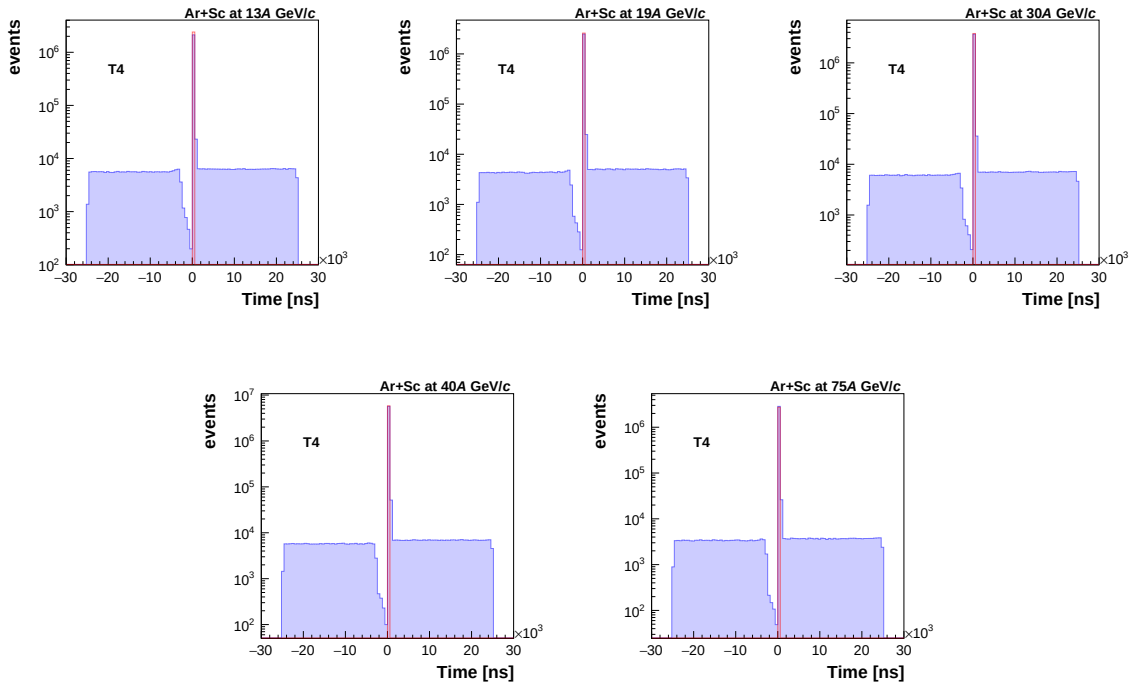

Figure 18: Distributions of beam particles time measured by the T4 counter with respect to a trigger signal in target-inserted ^{40}Ar + ^{45}Sc collisions at beam momenta of 13A-75A GeV/c are shown. The blue line with blue-shaded distributions and the red line with red-shaded distributions are before and after the WFA cut.

5.4 Biasing event selection

In turn, inappropriately applied downstream of the target or biasing cuts may (and typically do) affect the properties of the wanted events. Typically, these are used to remove the background of non-target interactions or to determine collision *centrality*. Using Monte Carlo simulations, it is possible to estimate, and , if needed, correct the effect of these biasing cuts.

5.4.1 Interaction vertex fit quality

This criterion ensures that during the reconstruction process, the interaction vertex is fitted and that the fit quality is good enough.

5.4.2 Interaction vertex z position

Distributions of the fitted z vertex position for the target inserted for ^{208}Pb + ^{208}Pb collisions at beam momentum of 13*A* and 30*A* GeV/*c* and ^{40}Ar + ^{45}Sc collisions at beam momentum of 13*A*-75*A* GeV/*c* are shown in Figs. 19 and 20. An overview of the fitted z vertex position for the target inserted and target removed in a broad range and an explanation of the origin of different peaks is presented in Fig. 34.

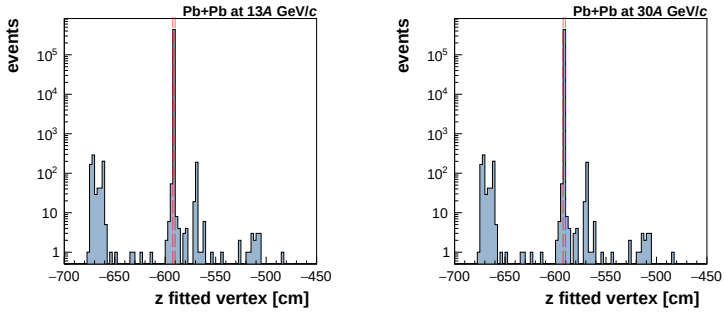

Figure 19: Distributions of the fitted z vertex position for the target inserted data-sets for ^{208}Pb + ^{208}Pb collisions at beam momentum of 13*A* and 30*A* GeV/*c* are shown. In all distributions, the red lines represent the cut used for event selection.

Further analysis was conducted only for events that have a reconstructed interaction vertex within $\pm$ 1 cm for ^{208}Pb + ^{208}Pb data-sets and $\pm$ 2 cm for ^{40}Ar + ^{45}Sc data-sets form the peak maximum or around. The red lines represent the cut used for event selection for ^{208}Pb + ^{208}Pb collisions at beam momentum of 13*A* GeV/*c* and ^{40}Ar + ^{45}Sc collisions at beam momentum of 75*A* GeV/*c*, shown in Figs. 19 and 20.

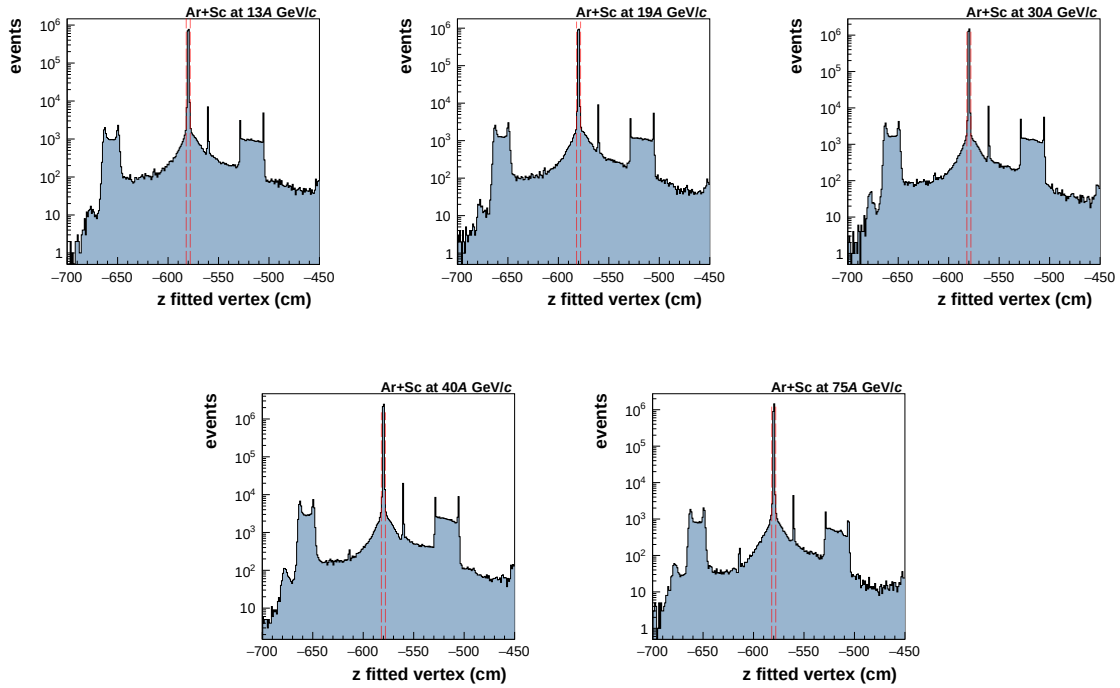

Figure 20: Distributions of the fitted z vertex position for the target inserted data-sets for ^{40}Ar + ^{45}Sc collisions at beam momentum of 13*A*-75*A* GeV/*c* are shown. In all distributions, the red lines represent the cut used for event selection.

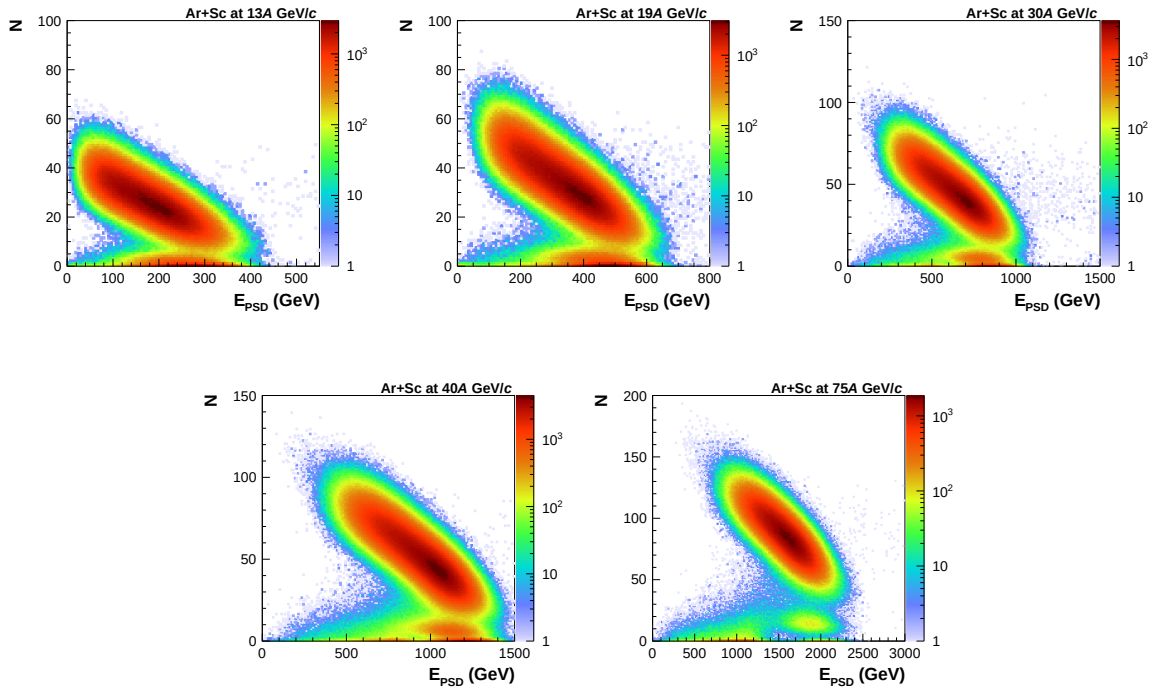

Figure 21: Distributions of PSD energy of all modules with the number of selected vertex tracks of ^{40}Ar + ^{45}Sc collisions at beam momenta of 13*A*, 19*A*, 30*A*, 40*A*, and 75*A* GeV/*c* respectively. PSD energy of all modules with the number of selected vertex tracks for selected events after interaction vertex z position selection citeria implementened.

5.5 PSD and/or detector malfunction event selection citeria

Set of runs T2 events have to be excluded due to instabilities with PSD and/or other detectors or due to reconstruction problem. For ^{40}Ar + ^{45}Sc collisions data sets, additional event selection criteria related to PSD energy are discussed in Sec. 5.2. The distributions of PSD energy deposited in all modules (see Fig. 32) versus the number of selected vertex tracks shown in Figs. 23, 26, 29, and 31 to explain to purpose of PSD malfunction event selection criteria. These event selection criteria were only implemented for ^{40}Ar + ^{45}Sc collisions at beam momenta of 13*A*-75*A* GeV .

5.5.1 PSD modules energy cut

The clouds in high E_{PSD} region in Fig. 21 are due to PSD and/or other detector or double hits. Distributions of small (module number from 1 to 16) vs large (module number from 17 to 44) PSD module energy (see Fig. 32) for ^{40}Ar + ^{45}Sc collisions at beam moentum of 13*A*-75*A* GeV/*c* presented in Fig. 22. Vertical blue line represents the upper limit of small PSD modules energy and horizontal red lines represent the upper and lower limits of large PSD modules energy. The values of the event selection criteria related to PSD small and large modlue energy are summarized in Table 8. Distributions of PSD energy versus the number of vertex tracks for selected events after the PSD energy of small and large modules selection criteria are shown in Fig. 23. This event selection criteria removes events from the analyzed data sets due to PSD malfunctioning or double hits.

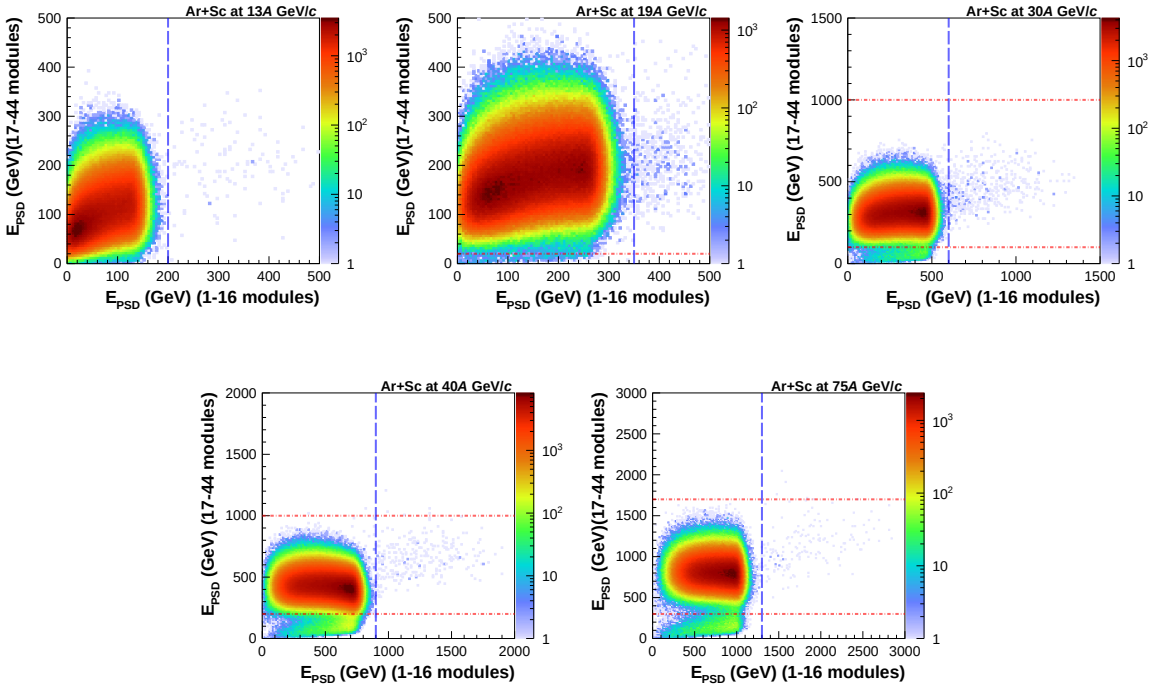

Figure 22: Distributions of small (module number from 1 to 16) vs large (module number from 17 to 44) PSD module energy (see Fig. 32) for ^{40}Ar + ^{45}Sc collisions at beam momenta of 13*A*-75*A* GeV/*c*. Vertical blue line represents the upper limit of small PSD modules energy and horizontal red lines represent the upper and lower limits of large PSD modules energy.

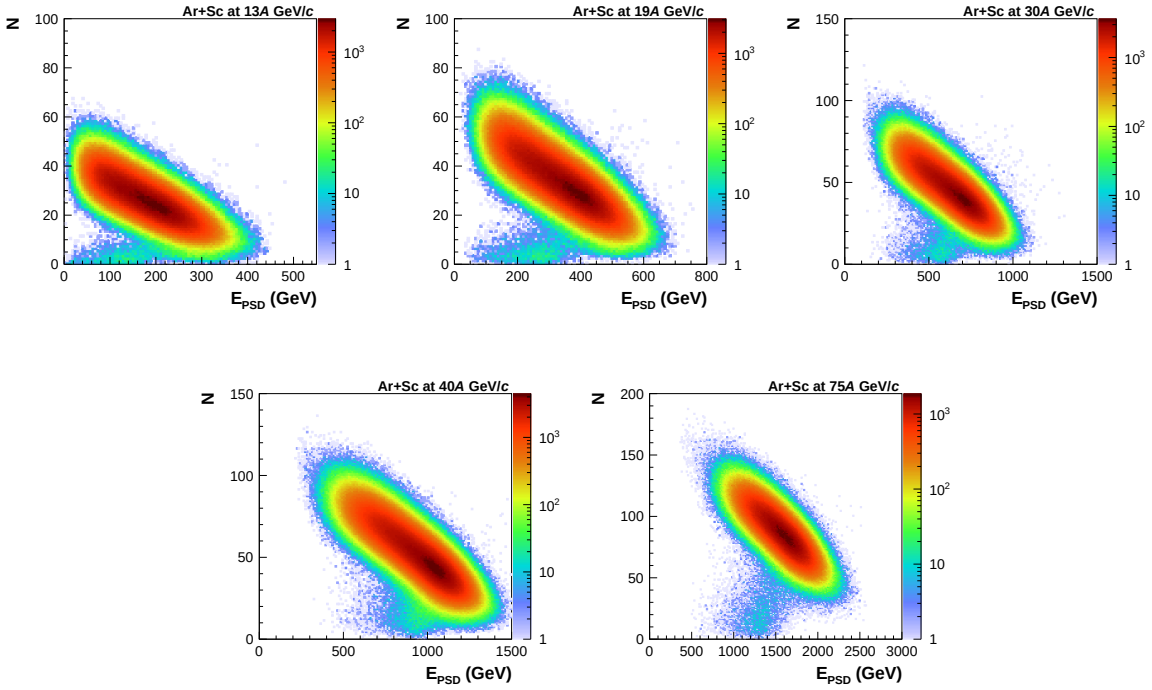

Figure 23: Distributions of PSD energy of all modules with the number of selected vertex tracks for ^{40}Ar + ^{45}Sc collisions at beam momenta of 13*A*, 19*A*, 30*A*, 40*A*, and 75*A* GeV/*c* respectively. PSD energy of all modules versus the number of selected vertex tracks for selected events after the PSD energy of small and large modules selection criteria implemented.

5.5.2 Track ratio cut

Not all registered tracks has fitted vertex (see Fig. 24). As an example of ^{40}Ar + ^{45}Sc collisions at 75*A* GeV/*c*, the ratio of tracks used for vertex fit (VtxTracks) to all registered tracks (allTracks) had to be greater than 0.17 in an event with number of tracks used for vertex fit greater than 31. Event selection criteria for ^{40}Ar + ^{45}Sc collisions at 13*A*, 19*A*, 30*A*, and 40*A* GeV/*c* is mentioned in Table 8. Distributions of vtxTrack (tracks has fitted vertex) to allTracks (all registered tracks) for ^{40}Ar + ^{45}Sc collisions at beam moentum of 13*A*-75*A* GeV/*c* before and after the track ratio criteria implemented are shown in Figs. 24 and 25. Distributions of PSD energy versus the number of vertex tracks of selected events for ^{40}Ar + ^{45}Sc collisions at 13*A*, 19*A*, 30*A*, 40*A*, and 75*A* GeV/*c* after the track ratio selection criteria implemented are shown in Fig. 26.

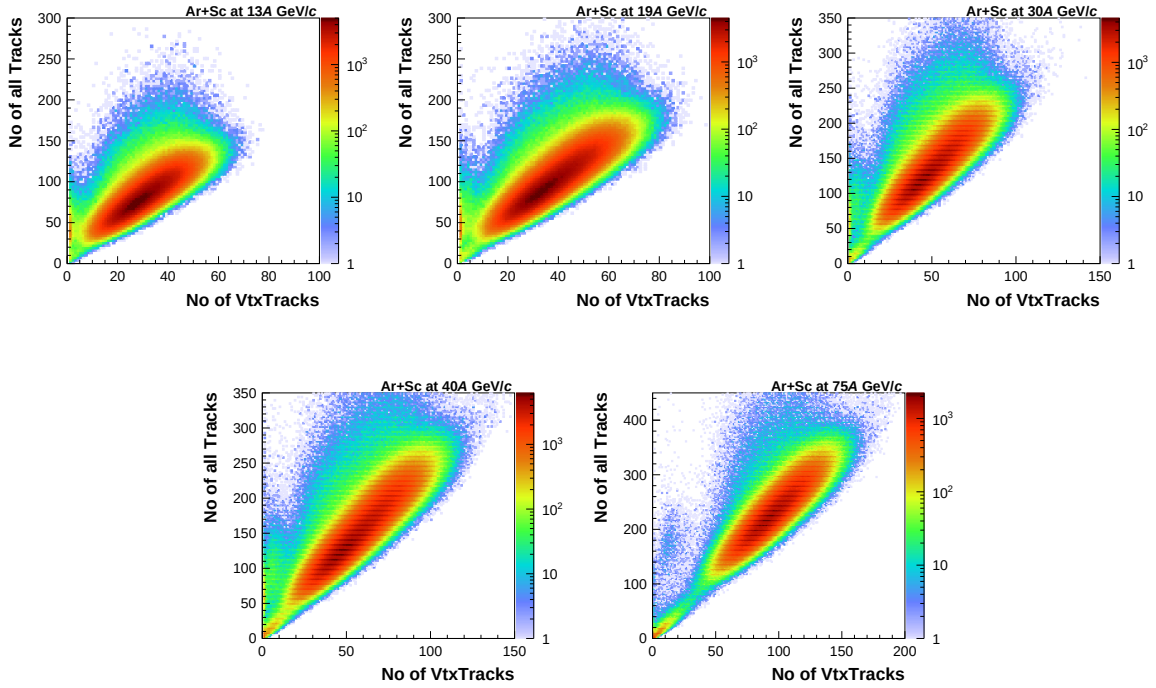

Figure 24: Distributions of vtxTrack (tracks has fitted vertex) to allTracks (all registered tracks) for ^{40}Ar + ^{45}Sc collisions at beam momenta of 13*A*-75*A* GeV/*c* before track ratio criteria implemented.

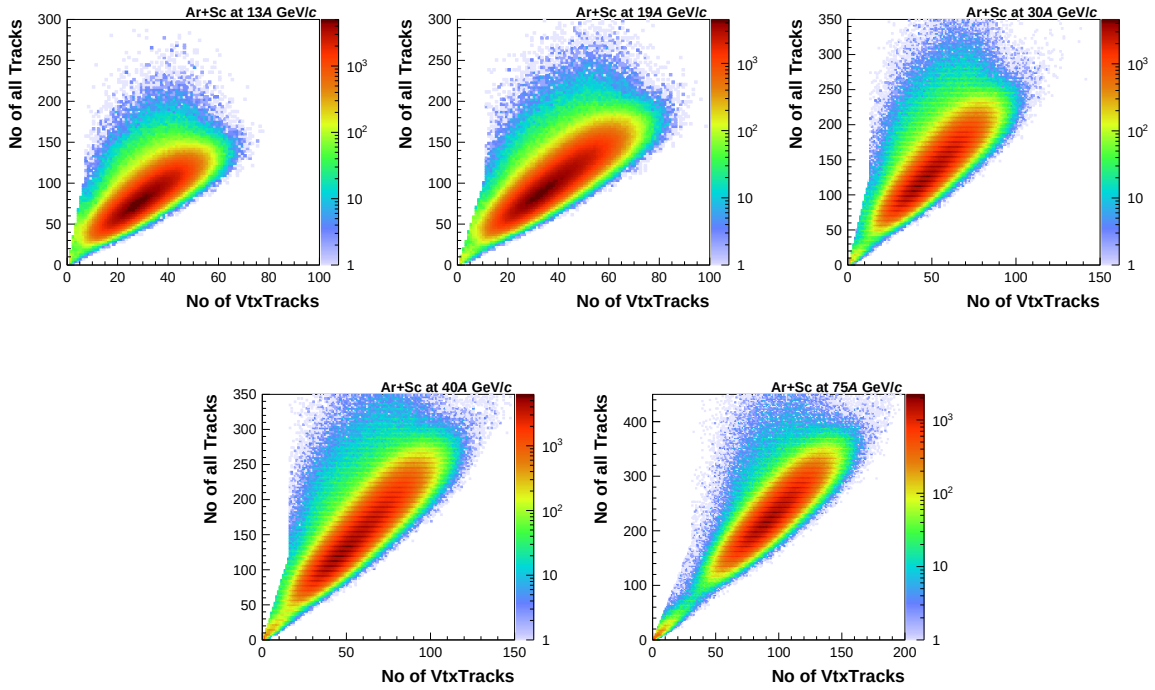

Figure 25: Distributions of vtxTrack (tracks has fitted vertex) to allTracks (all registered tracks) for ^{40}Ar + ^{45}Sc collisions at beam momenta of 13*A*-75*A* GeV/*c* after track ratio criteria implemented.

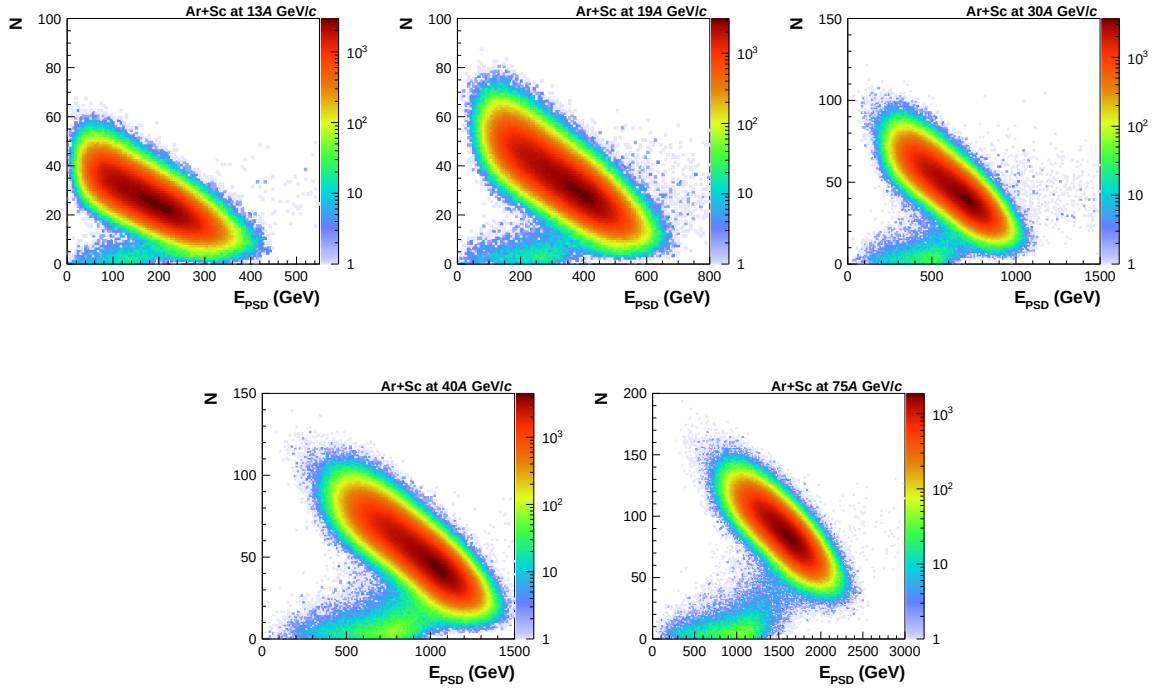

Figure 26: Distributions of PSD energy versus the number of vertex tracks of selected events for ^{40}Ar + ^{45}Sc collisions at beam momenta for 13*A*, 19*A*, 30*A*, 40*A*, and 75*A* GeV/*c* after the track ratio selection criteria implemented.

5.5.3 S5 ADC cut

The clouds in low multiplicity and E_{PSD} region in Fig.26 are removed based on graphical cut in Fig.28 for S5 ADC signal greater than 80 (see Fig. 27). Effect of this selection criteria is visible in Fig. 29.

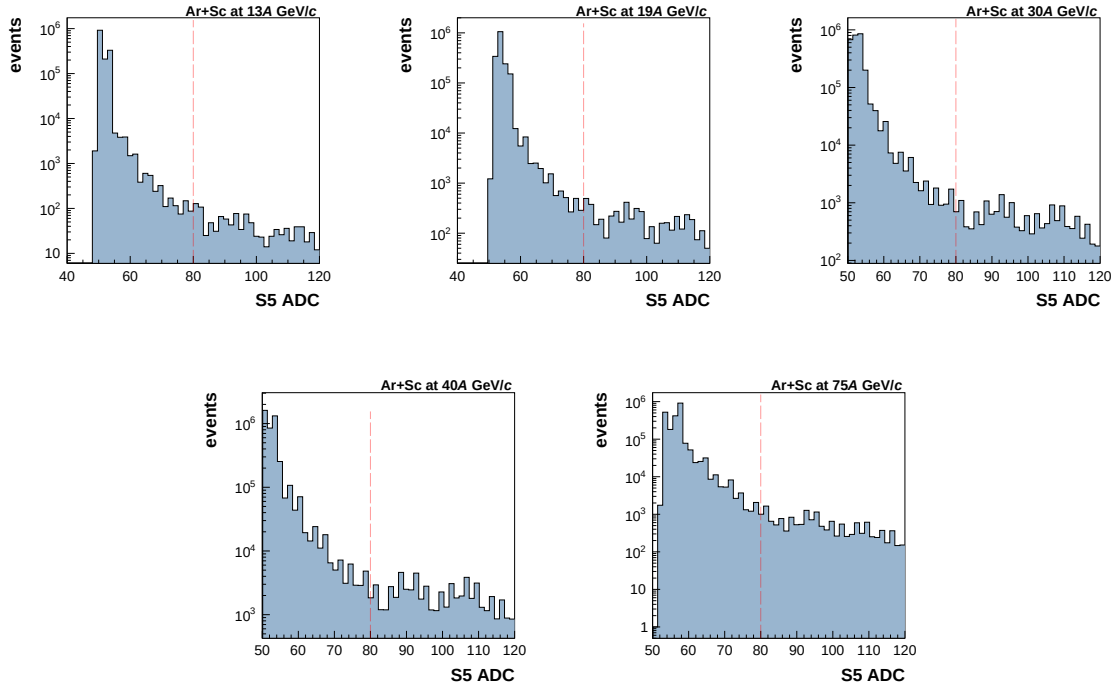

Figure 27: Distributions of S5 ADC signal for ^{40}Ar + ^{45}Sc collisions at beam momenta of 13*A*, 19*A*, 30*A*, 40*A*, and 75*A* GeV/*c* respectively. The vertical lines represent S5 ADC signal at 80.

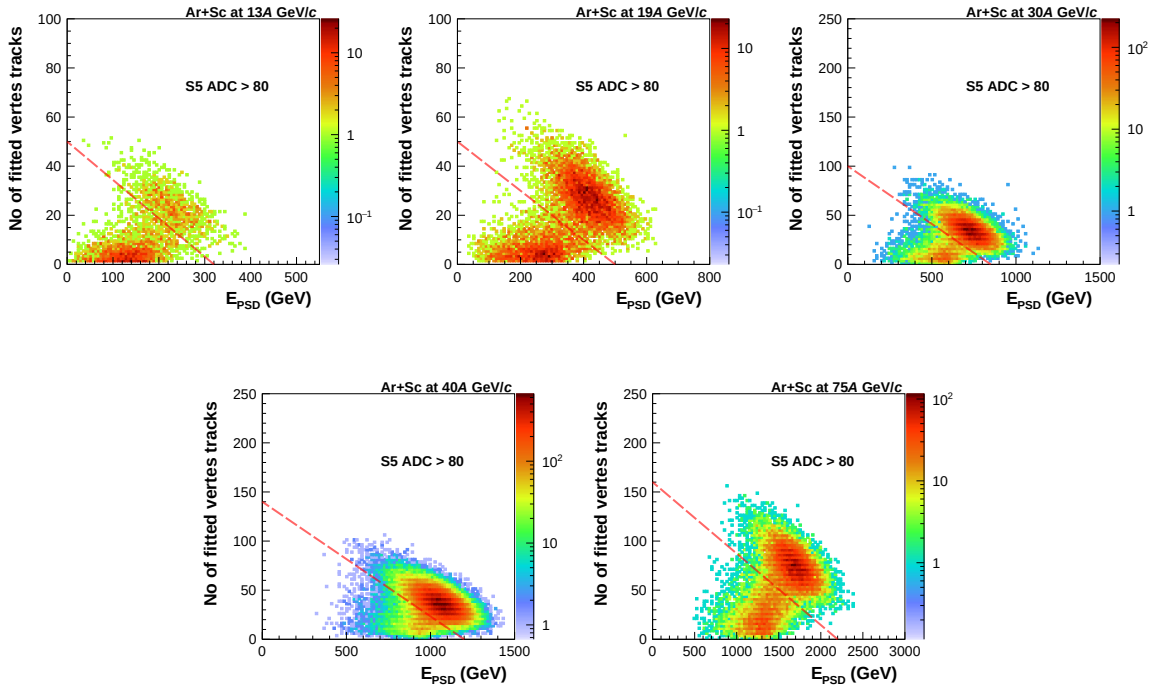

Figure 28: Distributions of PSD energy versus number of fitted vertex form events with S5 ADC signal greater than 80 for ^{40}Ar + ^{45}Sc collisions at 13A, 19A, 30A, 40A, and 75A GeV/c respectively. The clouds below the red lines are removed by the selection criteria.

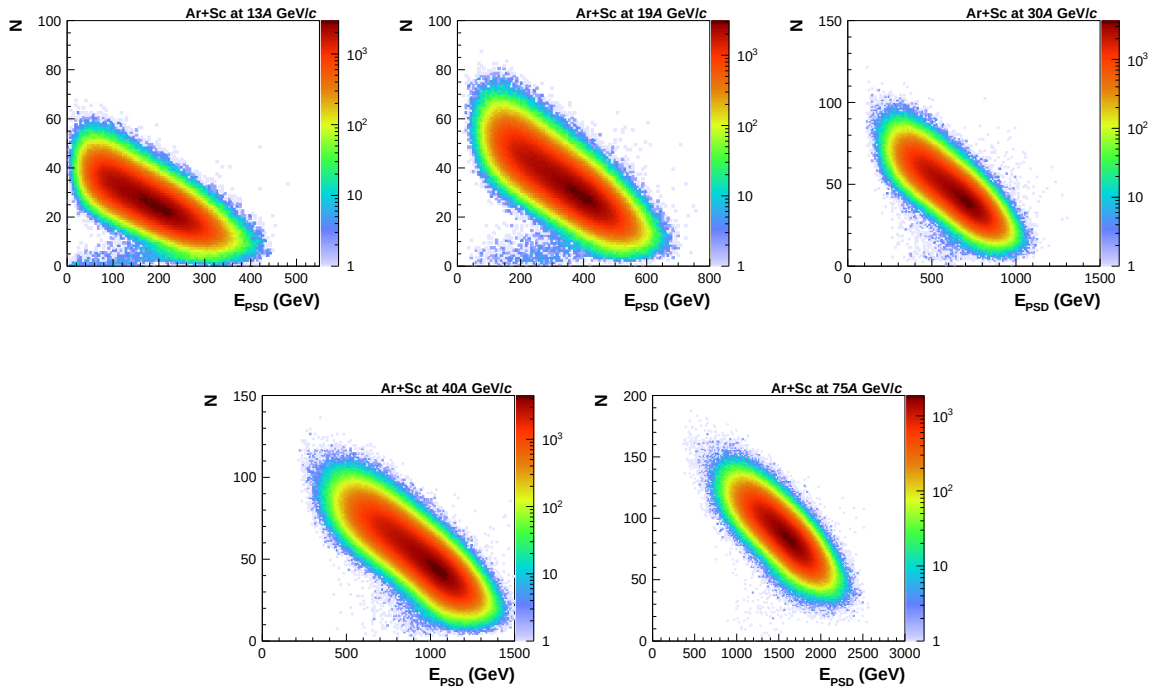

Figure 29: Distributions of PSD energy of all modules with the number of selected vertex tracks for ^{40}Ar + ^{45}Sc collisions at beam momenta of 13A, 19A, 30A, 40A, and 75A GeV/c respectively. PSD energy of all modules with the number of selected vertex tracks for selected events after S5 ADC selection citeria implementened.

5.5.4 PSD energy vs all tracks cut

The possible source of the additional clouds for ^{40}Ar + ^{45}Sc collisions at beam momentum of 13*A* and 19*A* GeV/*c* are unknown. Additional selection criteria was implemented for ^{40}Ar + ^{45}Sc at 13*A* and 19*A* GeV/*c* based on PSD energy with number of all tracks to remove those additional clouds from Fig. 29. The selection criteria is shown in Fig. 30. Distributions of PSD energy versus number of selected vertex tracks after this additional selection criteria shown in Fig. 31.

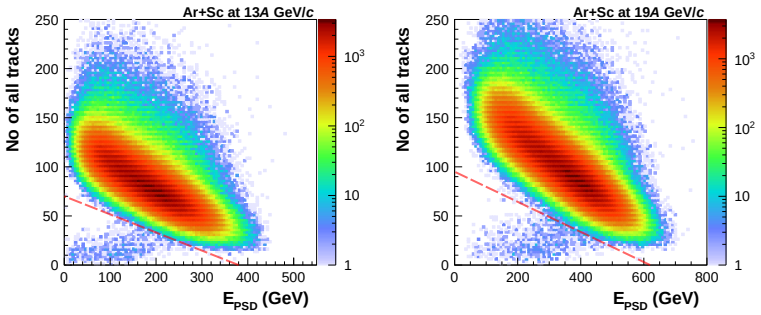

Figure 30: Distributions of PSD energy of all modules with the number of all tracks of ^{40}Ar + ^{45}Sc collisions at beam momentum of 13*A* and 19*A* GeV/*c*. The red lines represent the selection criteria to remove additional clouds for ^{40}Ar + ^{45}Sc at beam momentum of 13*A* and 19*A* GeV/*c* from Fig. 29.

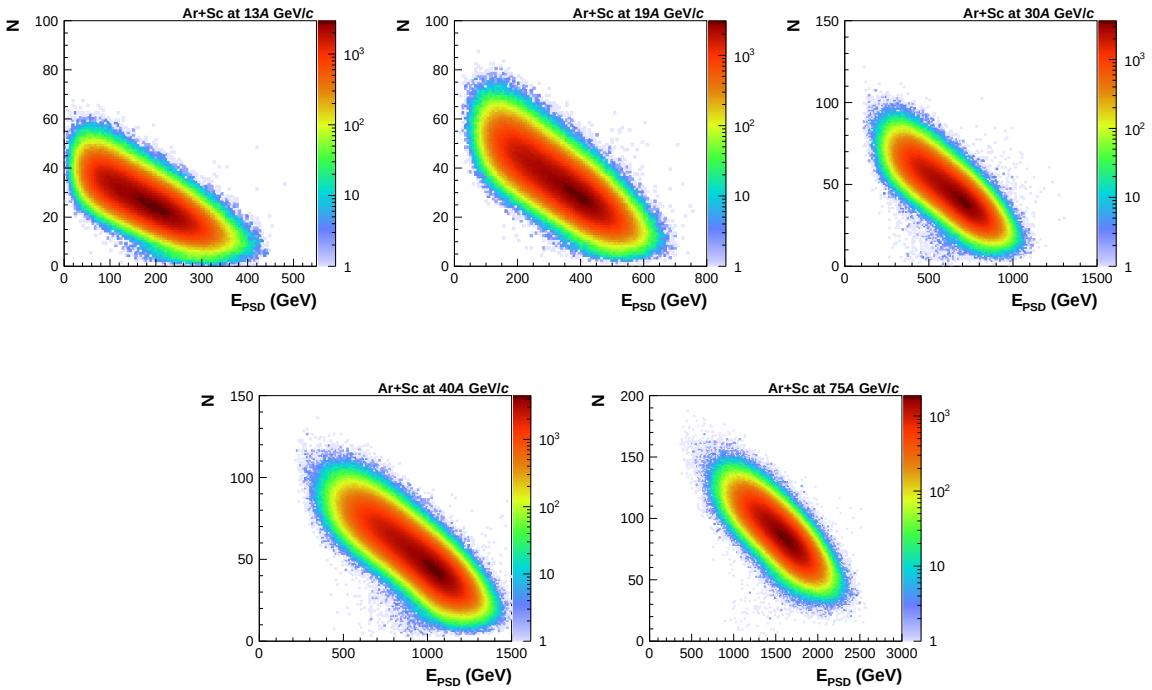

Figure 31: Distributions of PSD energy of all modules with the number of selected vertex tracks of ^{40}Ar + ^{45}Sc collisions at beam momenta of 13A, 19A, 30A, 40A, and 75A GeV/c respectively. PSD energy of all modules with the number of selected vertex tracks for selected events after PSD energy versus to all tracks selection criteria implemented.

5.6 Centrality selection

The energy deposited in PSD, E_{PSD}, is the basis to calculate the number of projectile spectators, hence the collisions *centrality*. The analysis presented in this analysis note concerns 10% of the most *central* ^{40}Ar + ^{45}Sc and ^{208}Pb + ^{208}Pb collisions. A detailed discussion of the *centrality* selection procedure of ^{40}Ar + ^{45}Sc collisions can be found in Refs. [44, 45]. Modules used in the

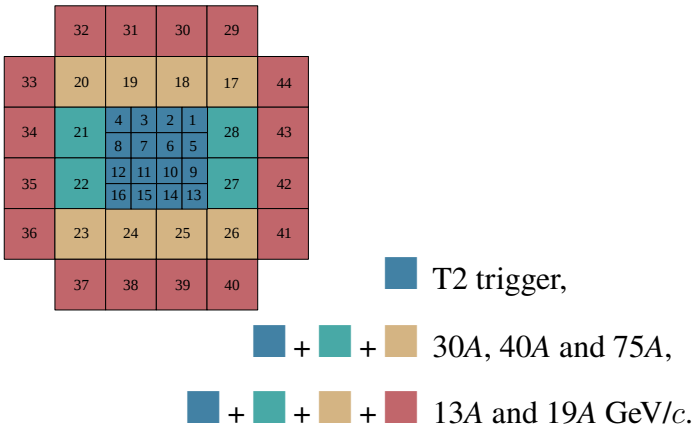

Figure 32: Modules used in the *centrality* determination were chosen based on the anti-correlation between the measured energy and the track multiplicity in a given event. All modules were used to determine the *centrality* of ^{40}Ar + ^{45}Sc collisions at beam momentum of 13*A* and 19*A* GeV/c. For 30*A*, 40*A*, and 75*A* GeV/c, 28 central modules were chosen. For the T2 trigger, 16 central modules were used.

centrality determination of ^{40}Ar + ^{45}Sc data sets are shown in Fig. 32. They were chosen based on the anti-correlation between the measured energy and the track multiplicity in a given event. All modules were used to determine the *centrality* of ^{40}Ar + ^{45}Sc collisions at beam momentum of 13*A* and 19*A* GeV/c and 28 central modules were chosen for 30*A*, 40*A*, and 75*A* GeV/c. For the T2 trigger, 16 central modules were used. For analysis of the data, the event selection was based on the $\approx$ 10% of collisions with the lowest value of the energy E_{PSD} measured by a subset of PSD modules (see Fig. 32) to optimize the sensitivity to projectile spectators. The acceptance resulting from the definition of the forward energy, E_F, corresponds closely to the acceptance [46] of this subset of PSD modules. Online event selection by the hardware trigger (T2) used a threshold on the sum of electronic signals from the 16 central modules of the PSD to accept $\approx$30% of all inelastic interactions (see Table 13).

The *centrality* selection of ^{208}Pb + ^{208}Pb collisions at beam momenta of 13*A* and 30*A* GeV/*c* was done using the model-based method and the data-based method. In this section, the model-based method is discussed.

5.6.1 Cross-section determination

An inelastic cross-section (σ_{inel}) is a cross-section for the processes where the type of initial state particles differ from the final state particles. Inelastic cross-sections have contributions due to electromagnetic and strong processes. The inelastic cross-section can be divided into two parts: quasi-elastic (σ_{qe}) and production (σ_{prod}) cross-section. Quasi-elastic cross-sections involve the process of either target, projectile, or both being fragmented, but no additional hadrons were produced. It is difficult to measure target fragmentation in fixed-target experiments. However, projectile fragmentation is measured by PSD. In the case of production cross-section, new

hadrons are produced in the final state. The inelastic cross-section can be written as:

$$\sigma_{inel} = \sigma_{qe} + \sigma_{prod} \ . \tag{5}$$

The inelastic cross-section due to strong interaction of ^{208}Pb + ^{208}Pb collisions at 13*A* and 30*A* GeV/*c* was calculated from the GLISSANDO model [47]. GLISSANDO – GLauber Initial-State Simulation AND mOre, a versatile Monte-Carlo generator for Glauber-like models of the initial stages of ultra-relativistic heavy-ion collisions. The value of inelastic cross-sections of ^{208}Pb + ^{208}Pb collisions at beam momenta of 13*A* and 30*A* GeV/*c* are summarized in Table 11.

5.6.2 Probability of inelastic interaction

The probability of inelastic interaction, P_{inel}, defined as a ratio between the beam particles that interacted with the target to all beam particles, can be defined as:

$$P_{inel} = \frac{\sigma_{inel} \cdot \rho \cdot L \cdot N_A}{A}, \tag{6}$$

where ρ is the target density, L is the target length, N_A is the Avogadro constant, and A is the atomic number of the target nuclei. The specifications of the ^{208}Pb target are summarized in Table. The probabilities of inelastic interaction of ^{208}Pb + ^{208}Pb at beam momenta of 13*A* and 30*A* GeV/*c* are summarized in Table 11.

5.6.3 Centrality determination

For the *centrality* determination of ^{208}Pb + ^{208}Pb collisions at beam momenta of 13*A* and 30*A* GeV/*c*, data sets are analyzed using identified beam trigger (T1 trigger) with unbiasing event selection criteria (see Sec. 5.3). All biasing and unbiasing event selection criteria are used to analyze ^{208}Pb + ^{208}Pb data sets using T4 and T2 triggers. All PSD modules, including the short module, are used to calculate the PSD energy of ^{208}Pb + ^{208}Pb collisions at beam momenta of 13*A* and 30*A* GeV/*c*. The PSD energy distributions of ^{208}Pb + ^{208}Pb collisions at beam momentum of 13*A* GeV/*c* using T1, T2, and T4 triggers are shown in Fig. 33 (*left*). The distributions are scaled to their integral to the left from the vertical green line, which is assumed to be unbiased by off-target interactions. The dashed vertical red line is at the energy, where the T2 PSD energy distribution has maximum.

The total number of inelastic collisions is given by

$$N_{\text{inel}} = \int_0^\infty \frac{dN}{dE_{PSD}^{T1}} dE_{PSD}^{T1} \cdot P_{inel}, \tag{7}$$

while the number of T2 inelastic collisions is calculated as

$$N_{T2} = \int_0^\infty \frac{dN}{dE_{PSD}^{T2}} dE_{PSD}^{T2}. \tag{8}$$

The T2 *centrality* is defined as

$$C_{T2} = N_{T2}/N_{inel}, \tag{9}$$

and the values of C_{T2} for ^{208}Pb + ^{208}Pb collisions at beam momenta of 13*A* GeV/*c* and 30*A* GeV/*c* are listed in Table 11.

The cumulative distribution of the T2 trigger PSD energy scaled to C_{T2} is shown in Fig. 33 (*right*). The dotted horizontal red, blue, magenta, and green lines represent 5%, 10%, 15%, and

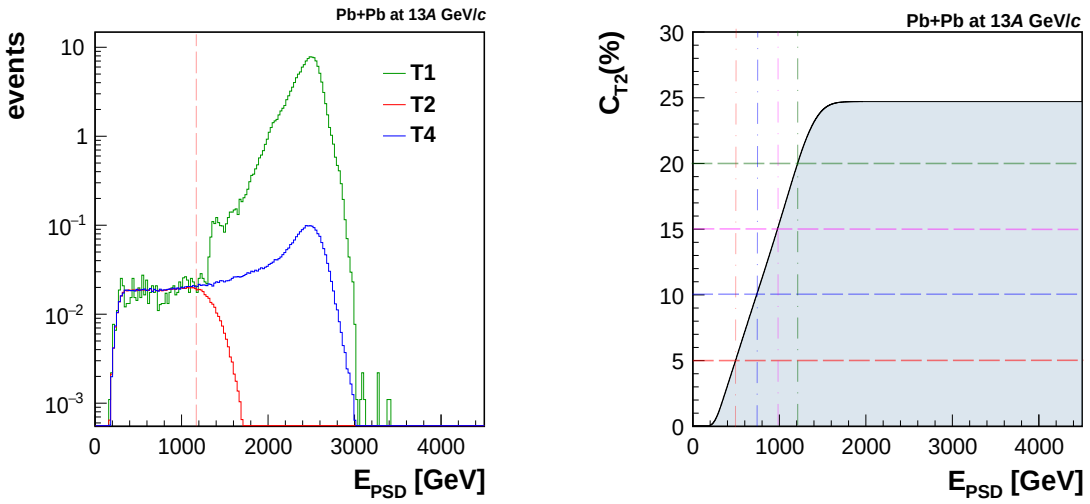

Figure 33: *Left:* The PSD energy distributions for ^{208}Pb + ^{208}Pb collisions at beam momentum of 13*A* GeV/*c* using T1, T2, and T4 triggers are shown, see text for details. *Right:* The scaled cumulative PSD energy distribution for ^{208}Pb + ^{208}Pb collisions at beam momentum of 13*A* GeV/*c* data considering the T2 trigger is shown, see text for details.

Table 11: The value of inelastic cross-section due to strong interaction for ^{208}Pb + ^{208}Pb collisions at beam momenta of 13*A* and 30*A* GeV/*c* are calculated from the GLISSANDO [47] model. Probability of inelastic collisions, P_{inel} and the T2 *centrality*, C_{T2} are calculated for ^{208}Pb + ^{208}Pb collisions at 13*A* and 30*A* GeV/*c*.

p_{beam} (GeV/*c*)	inelastic cross-section, σ_{inel} (mb)	P_{in} (%)	C_{T2}
13*A*	6618.0 ± 7.5	2.2	28%
30*A*	6661.7 ± 3.7	2.3	25%

20% *centrality* intervals, respectively, and the dotted vertical lines represent the corresponding lowest value of E_{PSD} to select desired central events.

The lowest values of the PSD energy to select 10% of the most central ^{208}Pb + ^{208}Pb collisions at beam momenta of 13*A* and 30*A* GeV/*c* are summarized in Table 13. The lowest values of E_{PSD} for different *centrality* intervals from the model-based and the data-based method are summarized in Table 12.

5.6.4 Data-based centrality selection

Centrality selection for ^{208}Pb + ^{208}Pb collisions at 13*A* and 30*A* GeV/*c* was done using two methods: the model-based method and the data-based method. The model-based method was discussed in Sec. 5.6. The data-based method will be briefly discussed in this Appendix.

The data were taken using two target configurations: target inserted (target IN) and target removed (target R). A summary of target IN and target R statistics of the collected Pb+Pb data is summarized in Table. 2. The target R data was collected to correct for interactions of beam particles with the material surrounding the target (off-target interactions). The fitted z vertex position for ^{208}Pb + ^{208}Pb collisions at 13*A* GeV/*c* of the target IN and target R in a broad range and explanation of the origin of different peaks is present in Fig. 34. The distribution

for the data recorded with the ^{208}Pb target removed was scaled by a normalization factor, $\epsilon = N_{\rm I}[-685 < z > -610 \text{ cm}]/N_{\rm R}[-685 < z > -610 \text{ cm}]$, where $N_{\rm I}[-685 < z > -610 \text{ cm}]$ and $N_{\rm R}[685 < z > -610 \text{ cm}]$ are the numbers of events with the T1 trigger for the ^{45}Sc target inserted and removed data sets, respectively. The normalization region $-685 < z > -610$ cm was selected. The resulting normalization factors are $\epsilon = 6.0$ for ^{208}Pb + ^{208}Pb interaction at 13*A* GeV/*c*.

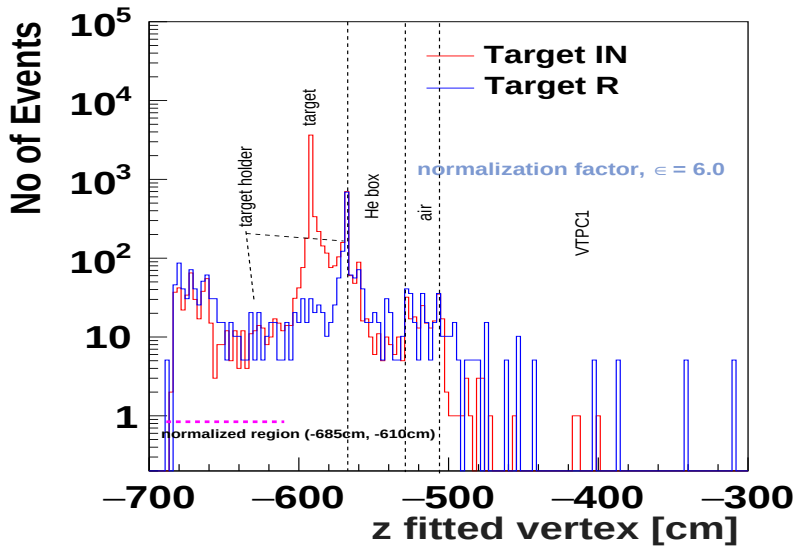

Figure 34: Distribution of fitted vertex z coordinate for data at ^{208}Pb + ^{208}Pb interactions at 13*A* GeV/*c* with ^{208}Pb target inserted and target removed (scaled as explained in the text) for the T1 trigger. Sources of peaks coming from beam interaction with experimental setup are explained.

The PSD energy distribution of target R is scaled by the normalization factor and subtracted from the target IN PSD energy to correct for off-target interactions. The normalized subtracted PSD energy distribution is shown in Fig. 35 (*left*). The normalized subtracted PSD energy distribution transforms into a cumulative distribution to calculate E_{PSD} limits for 0-10% of the central events. The desired centrality and corresponding E_{PSD} limits are mentioned in Fig. 35 (*right*). The lowest values of E_{PSD} for different centrality intervals from the model-based (see Sec. 5.6) and the data-based method are summarized in Table 12.

Table 12: The lowest value of E_{PSD} for 5%, 10%, 15%, 20% centrality interval from the model-based and the data-based method for ^{208}Pb + ^{208}Pb collisions at 13*A* GeV/*c* beam-momentum data set.

	data-based method	model-based method
centrality interval	E_{PSD} (GeV) limits	E_{PSD} (GeV) limits
5%	498	530
10%	720	825
15%	915	1083
20%	1120	1340

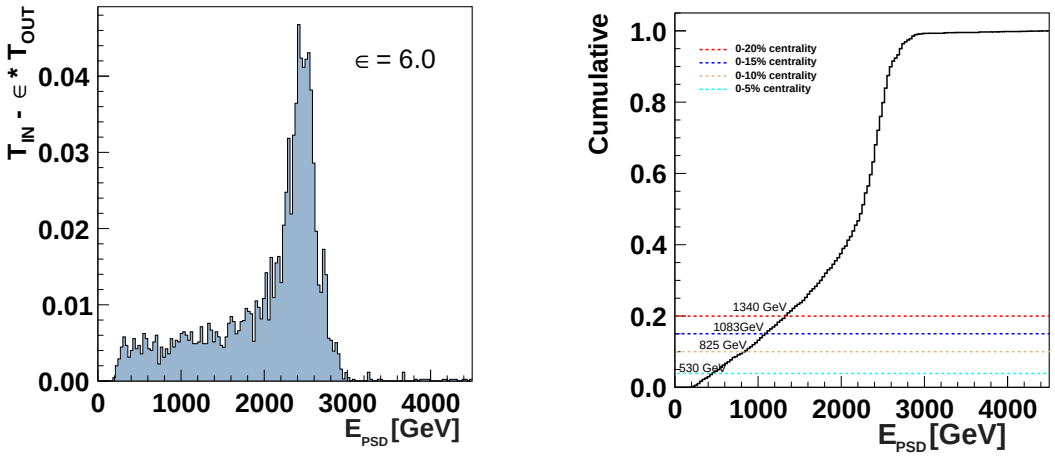

Figure 35: *Left:* The normalized subtracted PSD energy distribution for ^{208}Pb + ^{208}Pb collisions at 13*A* GeV/*c*. The PSD energy distribution of the target R data set was scaled by the normalization factor and subtracted from the target IN PSD energy distribution. *Right:* The normalized subtracted PSD energy distribution transform into cumulative distribution to calculate E_{PSD} limits for 0-10% of the central events.

5.6.5 Central event selection

The proton intermittency analysis results are presented in Sec. 10 for 0-10% of the most central events of ^{40}Ar + ^{45}Sc, and ^{208}Pb + ^{208}Pb collisions. In these analyses, 0-10% of the most central events for ^{40}Ar + ^{45}Sc and ^{208}Pb + ^{208}Pb data sets were selected using the E_{PSD} limits listed in Table 13.

Table 13: The values of online *centrality* selection by the hardware trigger (T2) of ^{208}Pb + ^{208}Pb collisions and ^{40}Ar + ^{45}Sc collisions are tabulated here. The lowest PSD energy values measured by a subset of PSD modules to select 0-10% of the most central collision events of ^{208}Pb + ^{208}Pb and ^{40}Ar + ^{45}Sc interaction are summarized here.

p_{beam} (GeV/*c*)	T2 *centrality* (%)	E_{PSD} limit (GeV) (for 10% central events)
^{208}Pb + ^{208}Pb data sets		
13*A*	34	825
30*A*	25	3002
^{40}Ar + ^{45}Sc data sets		
13*A*	30	143
19*A*	35	264
30*A*	30	446
40*A*	35	666
75*A*	20	1290.6

The event statistics after applying the selection criteria are summarized in Table 14.

Table 14: The statistics of selected events for ^{208}Pb + ^{208}Pb collisions at beam momenta of 13*A* and 30*A* GeV/*c* and ^{40}Ar + ^{45}Sc collisions at beam momenta of 13*A*-75*A* GeV/*c*.

p_{beam} (GeV/*c*)	target IN	T2 trigger (good events)	beam off-time	beam quality	vertex fit quality	vertex z position	PSD and/or detector malfunction	0-10% central
^{208}Pb + ^{208}Pb experimental data sets								
13*A*	$2.67{\cdot}10^6$	$6.58{\cdot}10^5$	$5.82{\cdot}10^5$	$2.50{\cdot}10^5$	$2.49{\cdot}10^5$	$2.46{\cdot}10^5$	$\times$	$1.17{\cdot}10^5$
30*A*	$4.69{\cdot}10^6$	$9.75{\cdot}10^5$	$8.35{\cdot}10^5$	$4.41{\cdot}10^5$	$4.40{\cdot}10^5$	$4.39{\cdot}10^5$	$\times$	$1.69{\cdot}10^5$
^{40}Ar + ^{45}Sc experimental data sets								
13*A*	$3.60{\cdot}10^6$	$2.52{\cdot}10^6$	$1.86{\cdot}10^6$	$1.79{\cdot}10^6$	$1.63{\cdot}10^6$	$1.62{\cdot}10^6$	$1.48{\cdot}10^6$	$4.97{\cdot}10^5$
19*A*	$3.70{\cdot}10^6$	$2.92{\cdot}10^6$	$2.31{\cdot}10^6$	$2.20{\cdot}10^6$	$2.02{\cdot}10^6$	$1.85{\cdot}10^6$	$1.83{\cdot}10^6$	$5.24{\cdot}10^5$
30*A*	$4.84{\cdot}10^6$	$4.08{\cdot}10^6$	$3.19{\cdot}10^6$	$3.09{\cdot}10^6$	$2.94{\cdot}10^6$	$2.76{\cdot}10^6$	$2.74{\cdot}10^6$	$9.13{\cdot}10^5$
40*A*	$8.92{\cdot}10^6$	$6.37{\cdot}10^6$	$5.39{\cdot}10^6$	$5.23{\cdot}10^6$	$4.91{\cdot}10^6$	$4.60{\cdot}10^6$	$4.54{\cdot}10^6$	$1.29{\cdot}10^6$
75*A*	$4.35{\cdot}10^6$	$3.11{\cdot}10^6$	$2.61{\cdot}10^6$	$2.53{\cdot}10^6$	$2.42{\cdot}10^6$	$2.35{\cdot}10^6$	$2.31{\cdot}10^6$	$1.16{\cdot}10^6$

6 Single-track selection

Among the selected events, many tracks should be rejected from the analysis. The cuts presented in this section are standard NA61/SHINE cuts common for most analyses in the experiment. To select tracks of primary charged hadrons and to reduce the contamination by particles from secondary interactions, weak decays, and off-time interactions, the following track selection criteria were applied.

6.1 Track fit quality

Only tracks fitted to the main interaction vertex were selected for this analysis. The momentum fit at the interaction vertex must have converged. The analysis presented in this analysis note is for selected proton candidates; therefore, only positively charged particles were selected.

6.2 Minimal number of clusters

This track cut ensures good momentum reconstruction and track quality. The threshold for the number of clusters in all TPCs (VTPC1, VTPC2, MTPCL, and MTPCR) (see Fig. 37) was set to 30. The maximum number of clusters in all TPCs is 234 and the maximum number of clusters in VTPCs (see Fig. 39) is 143. In addition, the number of clusters in VTPCs (VTPC1 and VTPC2) has to be larger than 15.

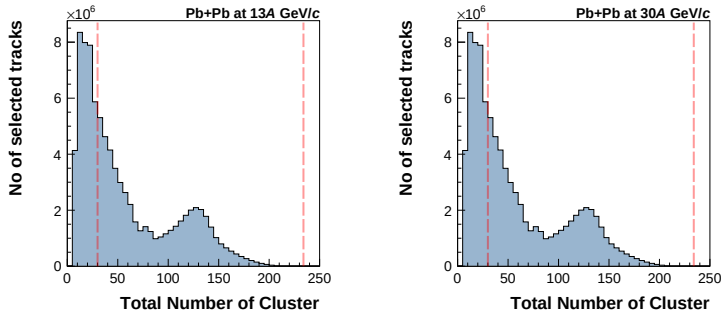

Figure 36: Distributions of total number of measured clusters in TPCs for ^{208}Pb + ^{208}Pb collisions at beam momentum of 13*A* and 30*A* GeV/*c* are shown. The dotted vertical lines show the upper and lower limits of the potential point ratio.

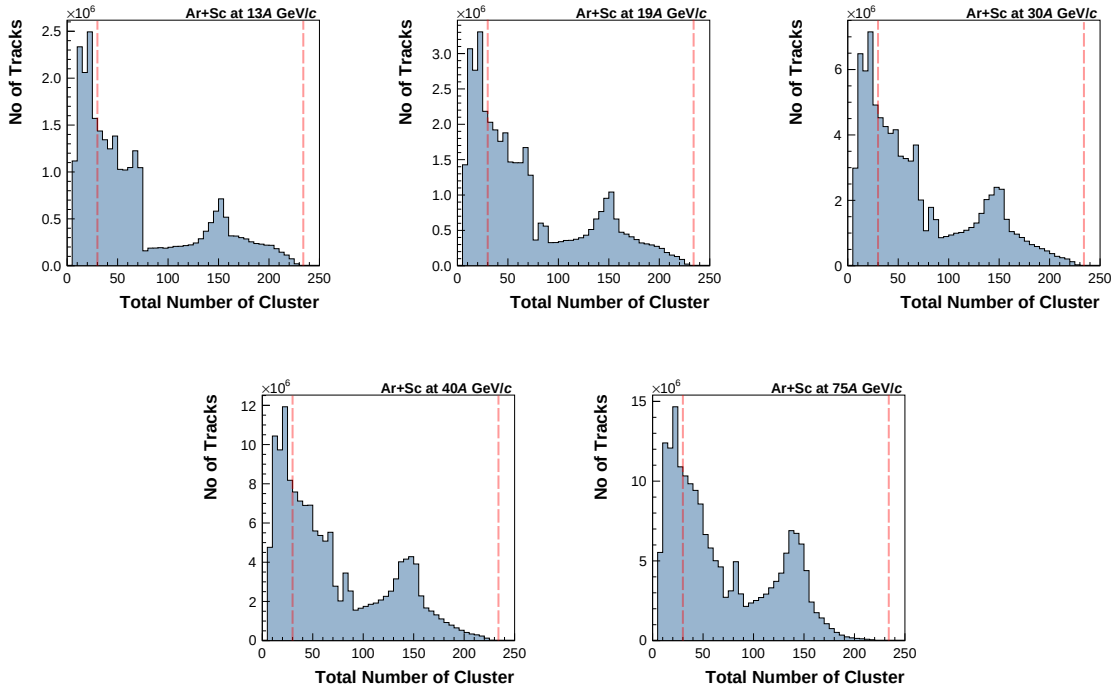

Figure 37: Distributions of total number of measured clusters in TPCs for ^{40}Ar + ^{45}Sc collisions at beam momentum of 13*A*-75*A* GeV/*c* are shown. The dotted vertical lines show the upper and lower limits of the potential point ratio.

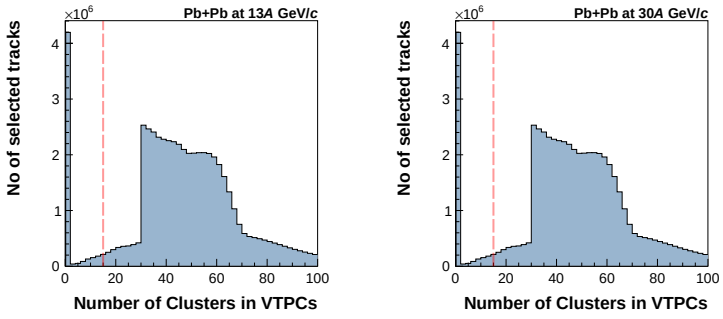

Figure 38: Distributions of number of measured clusters in VTPCs (VTPC1 and VTPC2) for ^{208}Pb + ^{208}Pb collisions at beam momentum of 13*A* and 30*A* GeV/*c* are shown. The dotted vertical lines show the upper and lower limits of the potential point ratio.

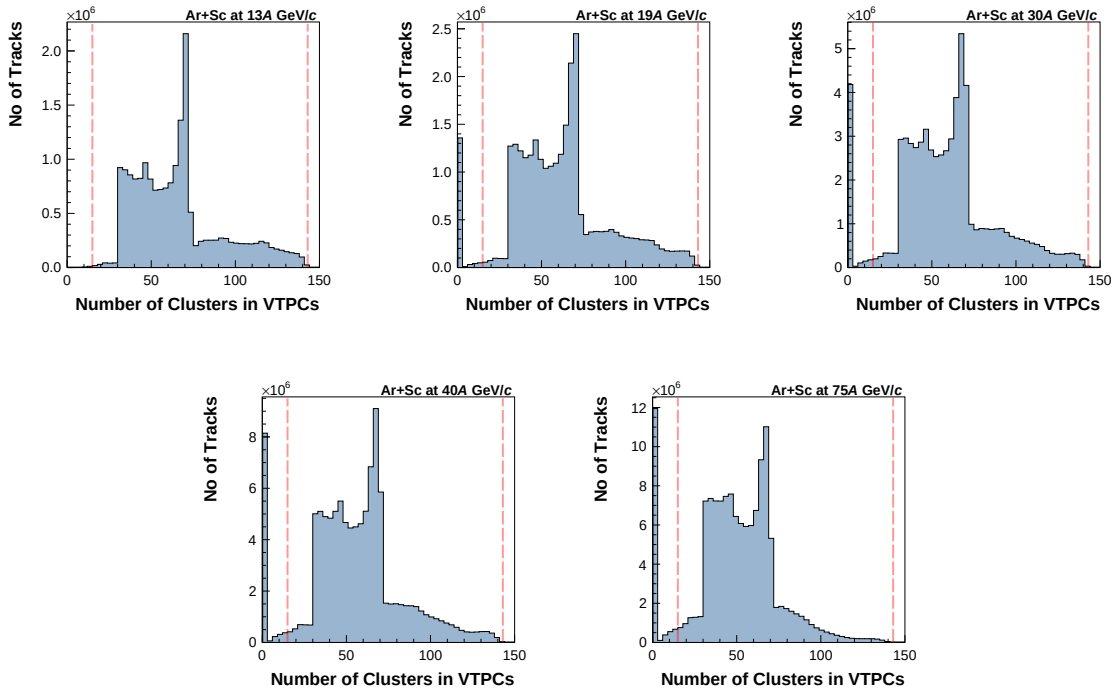

Figure 39: Distributions of number of measured clusters in VTPCs (VTPC1 and VTPC2) for ^{40}Ar + ^{45}Sc collisions at beam momentum of 13*A*-75*A* GeV/*c* are shown. The dotted vertical lines show the upper and lower limits of the potential point ratio.

6.3 Potential-point ratio

The TPC reconstruction may fail to merge track fragments in different TPCs. This can generate two or more tracks for a single particle. Such problematic tracks are referred to as split tracks. For all the selected tracks, the ratio of the number of measured clusters to the number of potential clusters in all TPCs must be greater than 0.5 and less than 1.1. The lower cut removes such split tracks. The number of potential clusters was calculated for vertex tracks. Example potential-point ratio distributions for ^{208}Pb + ^{208}Pb collisions at beam momentum of 13*A* and 30*A* GeV/*c* and ^{40}Ar + ^{45}Sc collisions at beam momenta of 13*A*-75*A* GeV/*c* are shown in Figs. 40 and 41. The dotted vertical lines show the upper and lower limit of the potential point ratio cut.

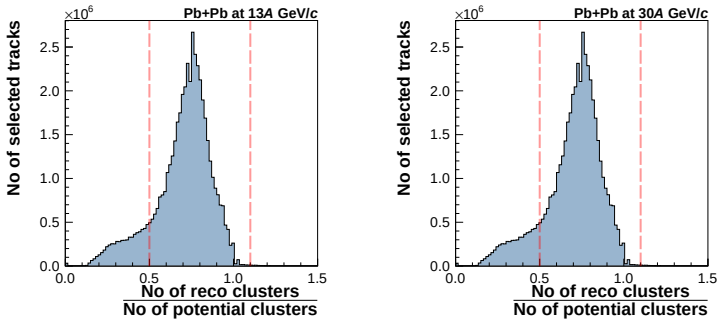

Figure 40: Distributions of ratio (the number of measured clusters to potential clusters in all TPCs) for ^{40}Ar + ^{45}Sc collisions at beam momentum of 13*A*-75*A* GeV/*c* are shown. The dotted vertical lines show the upper and lower limits of the potential point ratio.

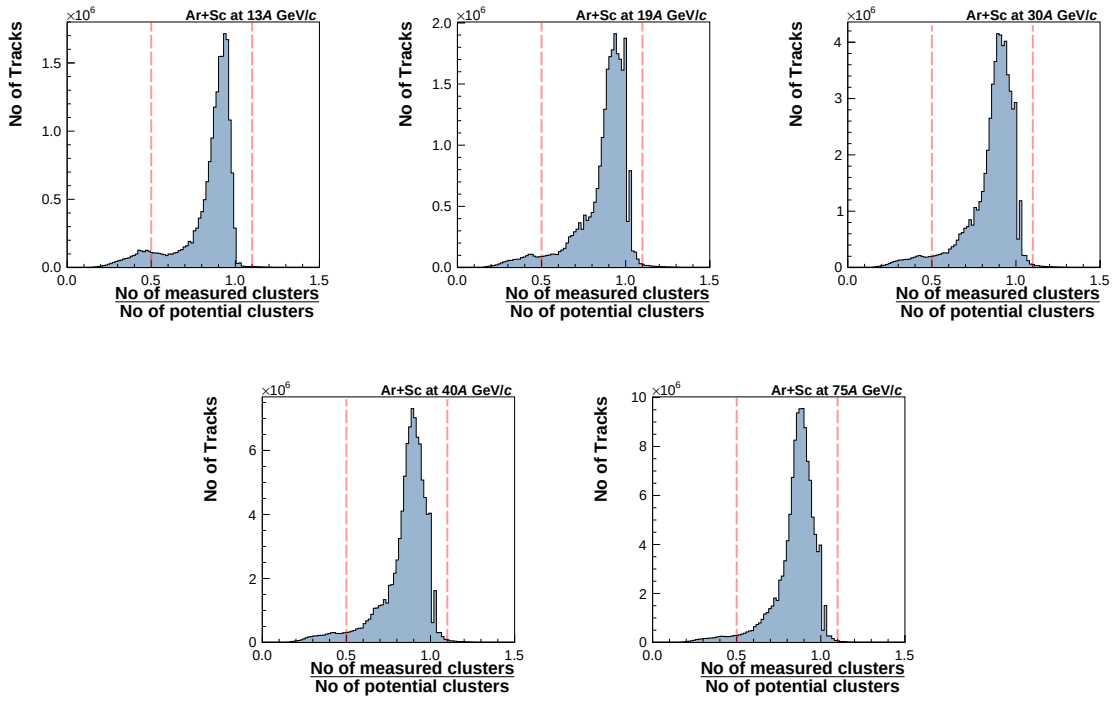

Figure 41: Distributions of ratio (the number of measured clusters to potential clusters in all TPCs) for ^{40}Ar + ^{45}Sc collisions at beam momentum of 13*A*-75*A* GeV/*c* are shown. The dotted vertical lines show the upper and lower limits of the potential point ratio.

6.4 Impact parameters

This track cut enforces that the difference between the track extrapolation to the target z position and the reconstructed interaction vertex is small enough in the x-y plane. It was required to be smaller than 4 cm in the horizontal (bending) plane (b_x) and 2 cm in the vertical (drift) plane (b_y). Example impact-parameters distributions for ^{208}Pb + ^{208}Pb collisions at beam momentum of 13*A* and 30*A* GeV/*c* and ^{40}Ar + ^{45}Sc collisions at beam momenta of 13*A*-75*A* GeV/*c* are shown in Figs. 42 and 43 . The dotted red rectangular region represents the region selected for the analysis.

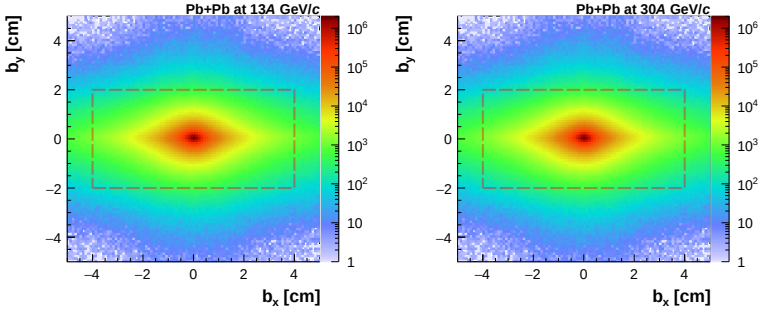

Figure 42: Distributions of impact-parameters (along x, b_x and along y, b_y) for ^{208}Pb + ^{208}Pb collisions at beam momentum of 13*A* and 30*A* GeV/*c* are shown. The dotted red rectangular region represents the region selected for the analysis.

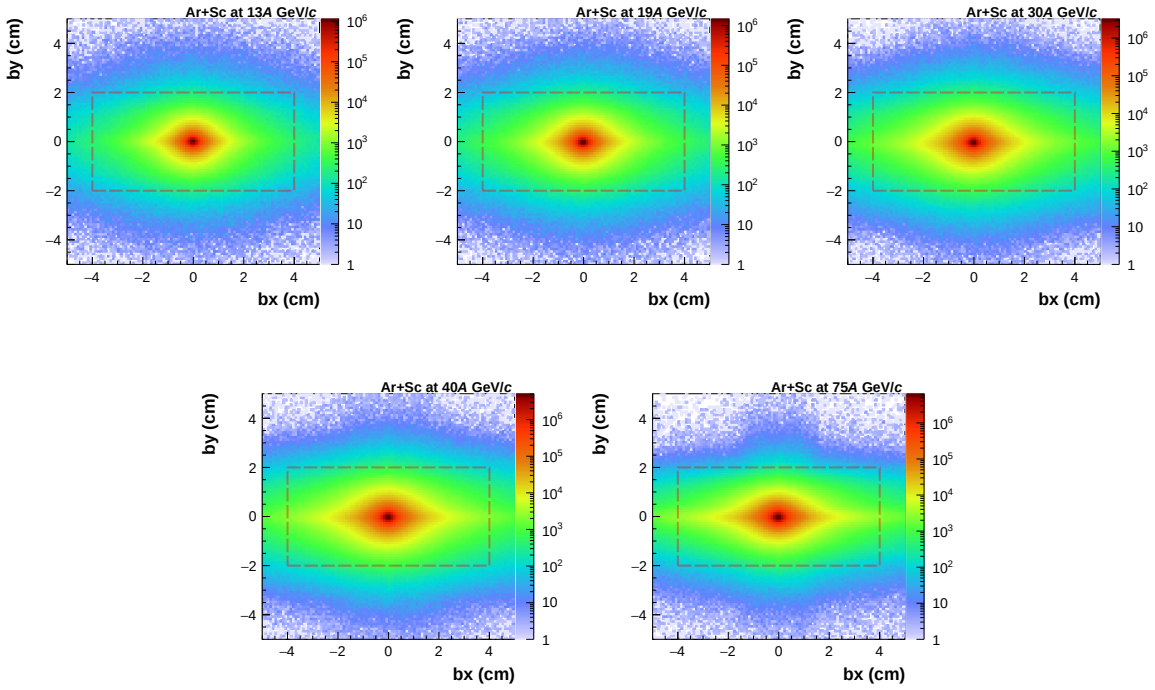

Figure 43: Distributions of impact-parameters (along x, b_x and along y, b_y) for ^{40}Ar + ^{45}Sc collisions at beam momentum of 13*A*-75*A* GeV/*c* are shown. The dotted red rectangular region represents the region selected for the analysis.

6.5 Transverse momenta

Only particles with transverse momentum components, $|p_x|$ and $|p_y|$, values less than 1.5 GeV/c, were selected for the analysis. Example transverse-momenta (along x, p_x and along y, p_y) distributions for ^{208}Pb + ^{208}Pb collisions at beam momentum of 13A and 30A GeV/c and ^{40}Ar + ^{45}Sc collisions at beam momentum of 13A-75A GeV/c are shown in Figs. 44 and 45. The dotted red rectangular region represents the region selected for the analysis.

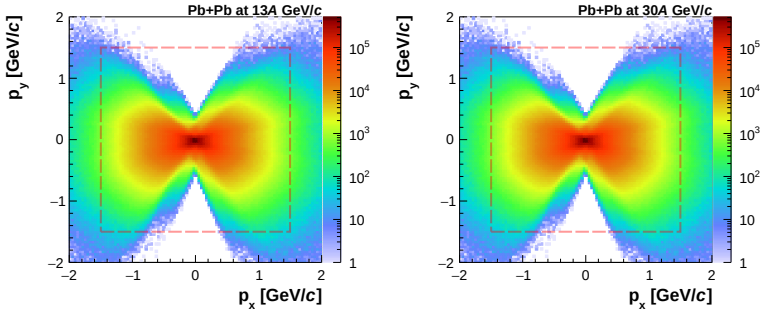

Figure 44: Distributions of transverse-momenta (along x, p_x and along y, p_y) for ^{208}Pb + ^{208}Pb collisions at beam momentum of 13A and 30A GeV/c are shown. The dotted red rectangular region represents the region selected for the analysis.

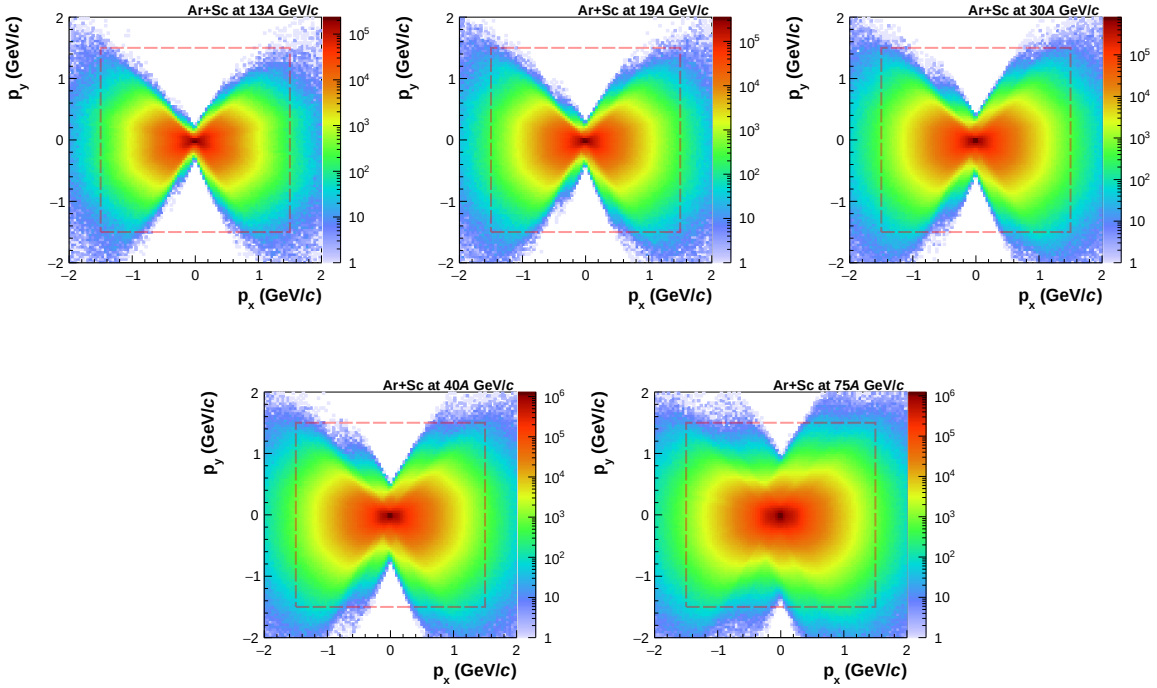

Figure 45: Distributions of transverse-momenta (along x, p_x and along y, p_y) for ^{40}Ar + ^{45}Sc collisions at beam momentum of 13A-75A GeV/c are shown. The dotted red rectangular region represents the region selected for the analysis.

The track statistics after applying the selection criteria are summarized in Table 15.

Table 15: The statistics of selected tracks for ^{208}Pb + ^{208}Pb collisions at beam momentum of 13*A* and 30*A* GeV/*c* and ^{40}Ar + ^{45}Sc collisions at beam momenta of 13*A*-75*A* GeV/*c*.

p_{beam} (GeV/*c*)	track fit quality	minimal number of clusters	potential-point ratio	impact-parameter	transverse-momenta
^{208}Pb + ^{208}Pb data sets					
13*A*	$5.179{\cdot}10^7$	$3.208{\cdot}10^7$	$2.914{\cdot}10^7$	$2.803{\cdot}10^7$	$2.777{\cdot}10^7$
30*A*	$8.465{\cdot}10^7$	$4.783\cdot10^7$	$4.266\cdot10^7$	$3.222{\cdot}10^7$	$3.178\cdot10^7$
^{40}Ar + ^{45}Sc data sets					
13*A*	$2.83{\cdot}10^7$	$1.88{\cdot}10^7$	$1.73{\cdot}10^7$	$1.69{\cdot}10^7$	$1.68{\cdot}10^7$
19*A*	$4.04{\cdot}10^7$	$2.62{\cdot}10^7$	$2.46{\cdot}10^7$	$2.40{\cdot}10^7$	$2.39{\cdot}10^7$
30*A*	$9.16{\cdot}10^7$	$5.94{\cdot}10^7$	$5.61{\cdot}10^7$	$5.47{\cdot}10^7$	$5.45{\cdot}10^7$
40*A*	$1.53{\cdot}10^8$	$9.89{\cdot}10^7$	$9.39{\cdot}10^7$	$9.16{\cdot}10^7$	$9.12{\cdot}10^7$
75*A*	$1.93{\cdot}10^8$	$1.23{\cdot}10^8$	$1.18{\cdot}10^8$	$1.17{\cdot}10^8$	$1.16{\cdot}10^8$

6.6 Selection of proton candidates

To select proton candidates, only positively charged particles were considered. Their ionization energy loss in TPCs is taken to be greater than 0.5 and less than the proton Bethe-Bloch value increased by the 15% difference between the values for kaons and protons while the total momentum is in the relativistic-rise region from 4 to 125 GeV/*c*.

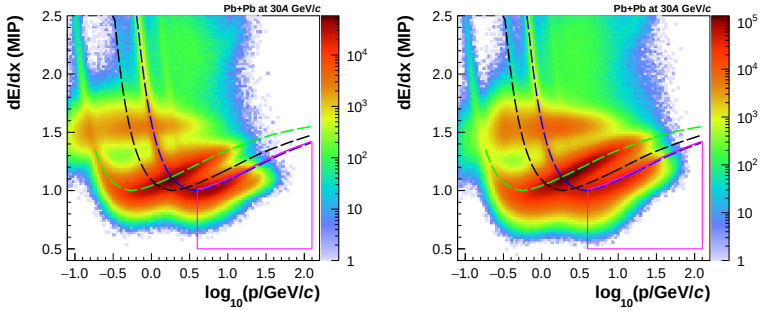

Figure 46: Energy loss measured in TPCs versus the logarithm of the total momentum of positively charged particles from selected events of ^{208}Pb + ^{208}Pb collisions at beam momenta of 13*A* and 30*A* GeV/*c* are shown, see text for details.

Energy loss measured in TPCs versus the logarithm of the total momentum of positively charged particles from selected events of ^{208}Pb + ^{208}Pb collisions at beam momenta of 13*A* and 30*A* GeV/*c*, and ^{40}Ar + ^{45}Sc collisions at beam momenta of 13*A*-75*A* GeV/*c* are shown in Figs. 46 and 47 respectively. The dashed blue, black, and green lines represent the nominal Bethe-Bloch values for protons, kaons, and pions. The selected region in the dE/dx- p_{LAB} plane is marked with a magenta line.

To estimate the fraction of selected protons and kaon contamination in the selected proton candidates, fits to the dE/dx distributions [**?**] in momentum bins were used. The dE/dx fits were done in two-dimensional *p* and p_T bins using *TShine* software. Gaussian distributions for protons and kaons for each bin were drawn with the help of fit parameters such as mean, amplitude, and standard deviation. Example distributions of dE/dx fit in $6.31 < p < 7.94$ GeV/*c* and 1.00$< p_T <$1.10 GeV/*c* bin for ^{208}Pb + ^{208}Pb collisions at beam momentum of 13*A* GeV/*c* (*left*)

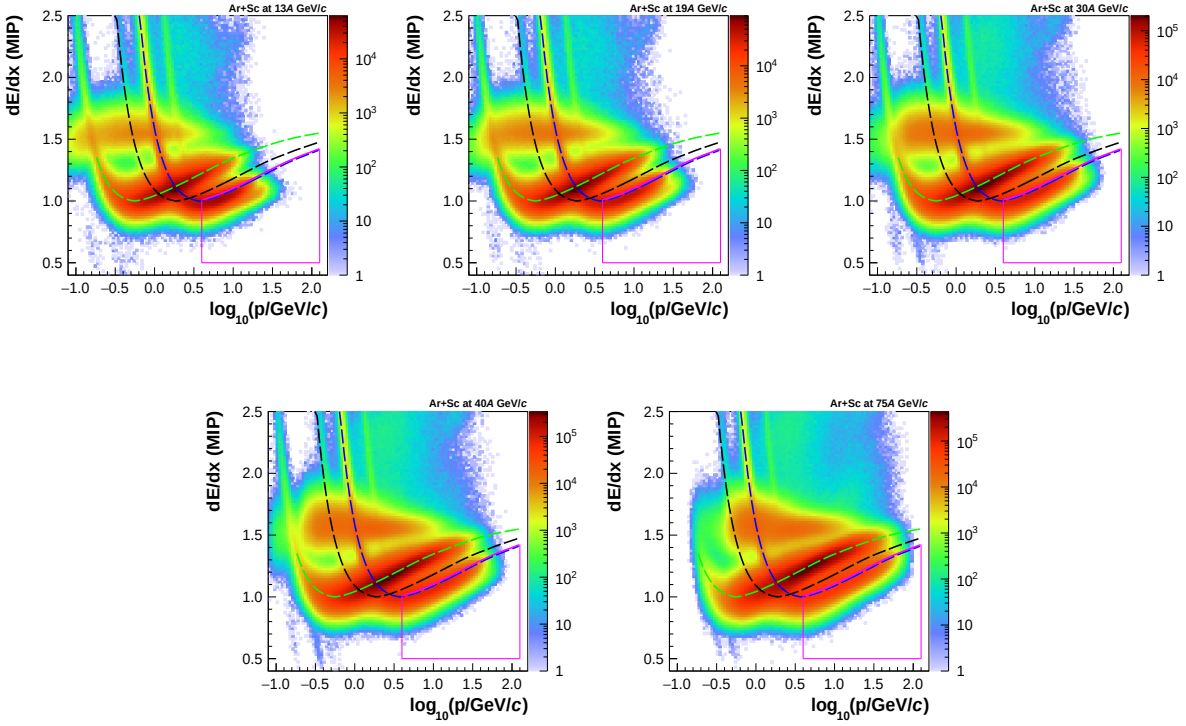

Figure 47: Energy loss measured in TPCs versus the logarithm of the total momentum of positively charged particles from selected events of ^{40}Ar + ^{45}Sc collisions at beam momenta of 13*A*, 19*A*, 30*A*, 40*A*, and 75*A* GeV/*c* are shown, see text for details.

and ^{40}Ar + ^{45}Sc collisions at beam momentum of 75*A* GeV/*c* (*right*) are shown in Fig. 48. Orange and blue distributions represent protons and kaons Gaussian distribution. The green

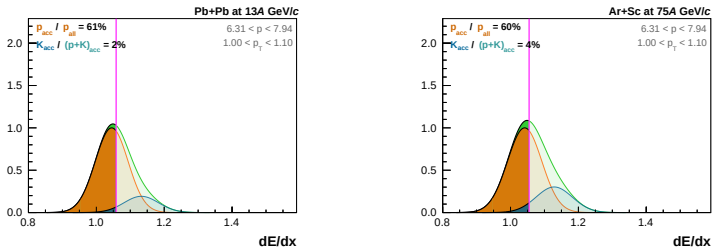

Figure 48: Example distributions of dE/dx fit in $6.31 < p < 7.94$ GeV/*c* and $1.00 < p_T < 1.10$ GeV/*c* bin for ^{208}Pb + ^{208}Pb collisions at beam momentum of 13*A* GeV/*c* (*left*) and ^{40}Ar + ^{45}Sc collisions at beam momentum of 75*A* GeV/*c* (*right*) are shown, see text for details. (Graphical modification as MG comments on 12.08)

distribution represents the sum of these two distributions. The vertical magenta line indicates the dE/dx cut used to select a proton candidate. The selection of proton candidates was found to select, on average, approximately 60% of protons and leave, on average, less than 4% of kaon contamination. The averaging was done over the $p - p_T$ acceptance of these analyses. The corresponding random proton losses do not bias the results in the case of independent production in the transverse momentum space [37]. The results for correlated protons will be

affected by the random losses of proton candidates. Thus the random proton losses due to the proton candidate selection has to be taken into account when calculating model predictions.

6.7 Rapidity selection

As the analysis concerns mid-rapidity protons [49], only proton candidates with center-of-mass rapidity assuming proton mass, y_p, greater than 0 and less than 0.75 were selected. Distributions of y_p versus transverse-momenta, p_T, for ^{208}Pb + ^{208}Pb collisions at beam momenta of 13*A* GeV/*c* (*left*) and 30*A* GeV/*c* (*right*) are shown in Fig. 49, and for ^{40}Ar + ^{45}Sc collisions at beam momenta of 13*A*-75*A* GeV/*c* are shown in Fig. 50. The dotted vertical lines show the upper and lower limits of the mid-rapidity proton selection.

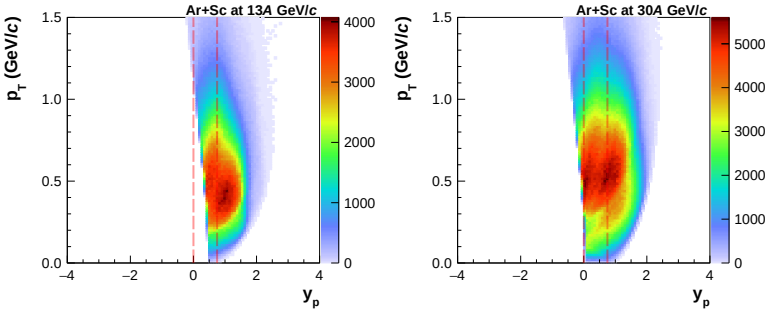

Figure 49: Distributions of y_p versus p_T for ^{208}Pb + ^{208}Pb collisions at 13*A* GeV/*c* (*left*) and 30*A* GeV/*c* (*right*) are shown, see text for details.

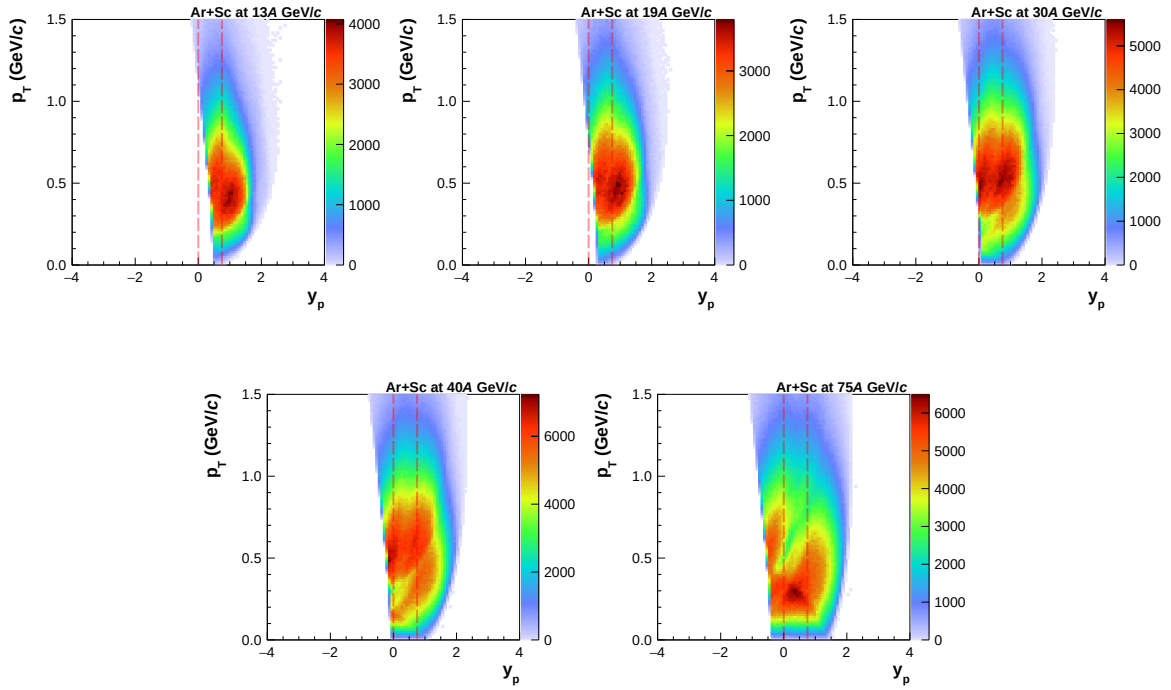

Figure 50: Distributions of y_p versus p_T for ^{40}Ar + ^{45}Sc collisions at beam momentum of 13A-75A GeV/c are shown, see text for details.

7 Single-particle acceptance maps

A three-dimensional (y_p, p_x and p_y) acceptance map [50] was created to describe the momentum region selected for the analysis. The map was created by comparing the number of Monte Carlo generated mid-rapidity protons before and after detector simulation and reconstruction. Only bins from the regions with at least 70% reconstructed tracks are included in the acceptance map. An example map for proton intermittency analysis of ^{40}Ar + ^{45}Sc collisions at 75*A* GeV/*c* is shown in Fig. 51. These maps are also used to calculate model predictions.

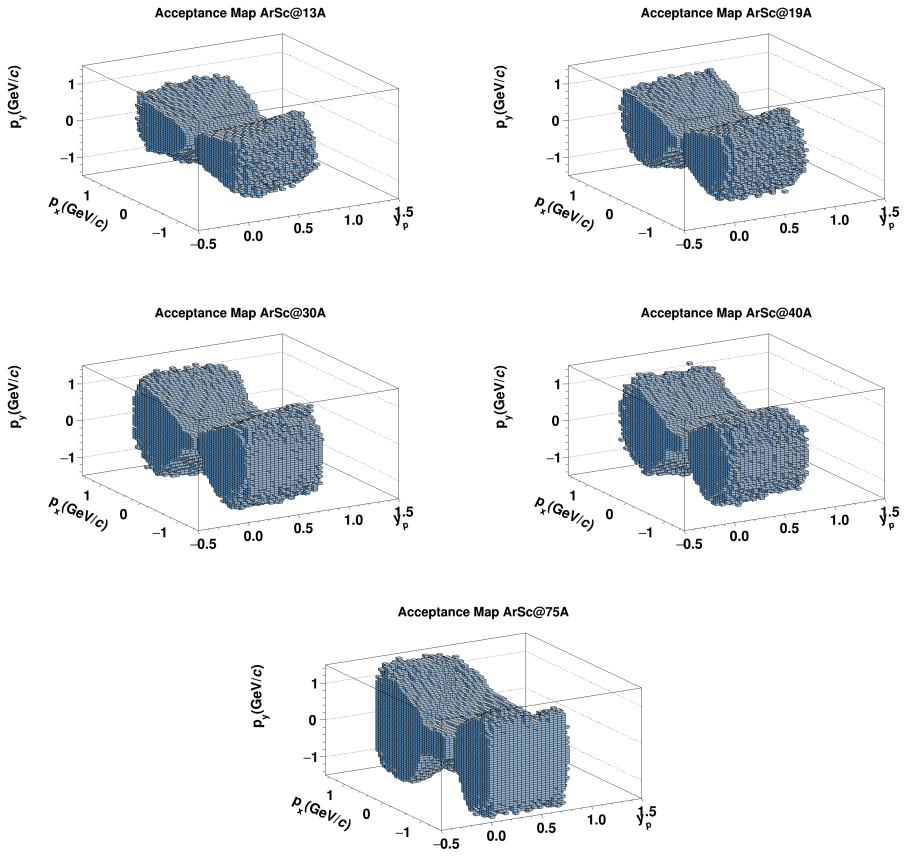

Figure 51: Example of single-particle acceptance map for ^{40}Ar + ^{45}Sc collisions at beam momentum of 75*A* GeV/*c* used for proton intermittency analysis, see text for details.

8 Two-particle acceptance map

Another new tool introduced to the intermittency analysis is a two-particle acceptance map in momentum space. The Time Projection Chambers (TPCs) are the primary tracking devices in the NA61/SHINE experiment. However, it's important to note that they do have limitations. In particular, when two tracks are too close in space, and their clusters overlap, the TPCs fail to differentiate between them. Consequently, the TPC cluster finder frequently rejects overlapping clusters, and the tracks can be lost. Moreover, the TPC track reconstruction may fail to merge two track fragments. This can generate two tracks out of a single track. These biases must be addressed.

An example of problematic tracks is shown in Fig. 52. One of them is a split track presented in Fig. 52 (*left*), and the second kind of problematic track is a merged track shown

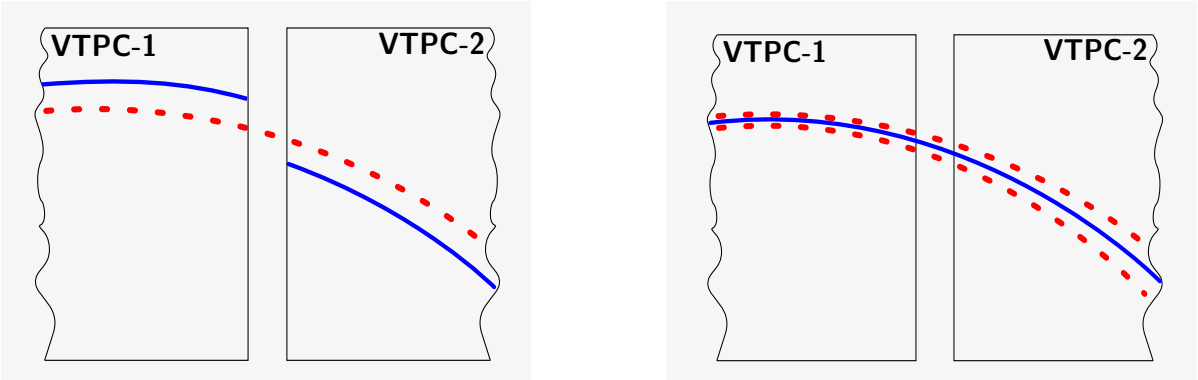

Figure 52: *Left:* An example of split tracks is illustrated here. The boxes represent the two TPC chambers labeled VTPC-1 and VTPC-2. The red dotted line is a single track, but it is split into two tracks between two VTPC-1 and VTPC-2 chambers. *Right:* An example of a merged track is illustrated here. The two red dotted lines represent the trajectory of two close in-space particles (tracks). The blue line represents the merged track, reconstructed when clusters of the two tracks overlap

in Fig. 52 (*right*). The potential point ratio, the ratio of the number of reconstructed points to the number of potential points in all TPCs is required be greater than 0.5 and less than 1.1. This cut can effectively eliminate split tracks. Previously, the geometric Two-Track Distance (gTTD) cut was utilized to eliminate a set of tracks that were positioned too closely together to be reconstructed using geometrical two-track distance calculations. Figure 53 (*left*) shows the

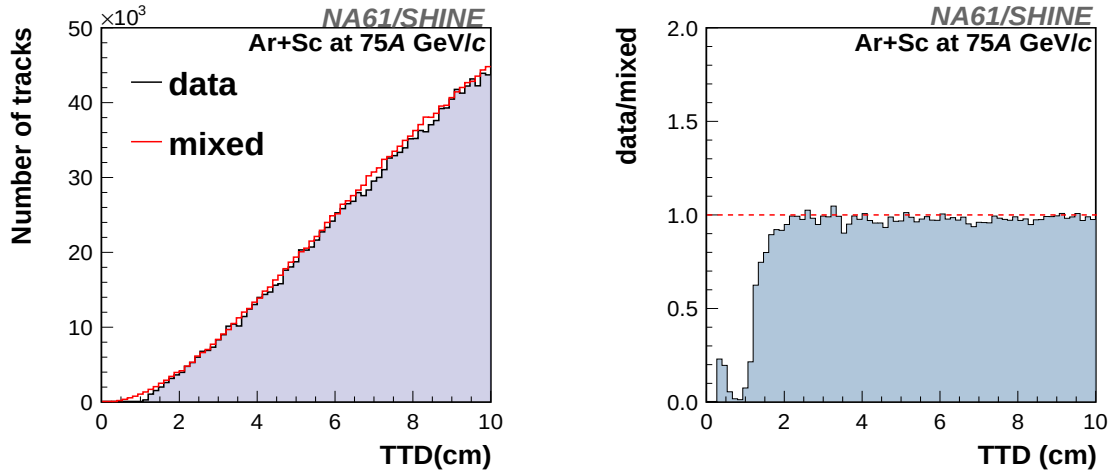

Figure 53: *Left:* An example of geometrical TTD for Ar+Sc at 75*A* GeV/*c* beam-momentum data (black line) and the corresponding mixed (red line) is shown. *Right:* The same distribution is shown for data to mixed ratio. A region less than 2 cm corresponds to the biased region due to the low efficiency of measuring two tracks.

geometric two-track distance of selected protons from Ar+Sc collisions at 75*A* GeV/*c* recorded by the NA61/SHINE experiment(red line) and the corresponding result for mixed events (black line). The ratio of the distributions is shown in Fig. 53 (*right*). The bias due to due to the low efficiency of measuring close tracks is seen for two-track distrance lower than 2 cm.

To apply the gTTD cut, the NA61/SHINE detector geometry and magnetic field information are required. However, access to this information is limited to those who are members of the NA61/SHINE Collaboration. Here, a momentum-based Two-Track Distance (mTTD) cut is introduced. The mTTD cut removes the remaining split tracks from the data after the potential point ratio cut, and it provides the precise definition of the biased region in which we don't have good efficiency for measuring two-tracks. Having this definition of the biased region, one can apply the mTTD cut to the model data. The magnetic field bends the trajectory of charged

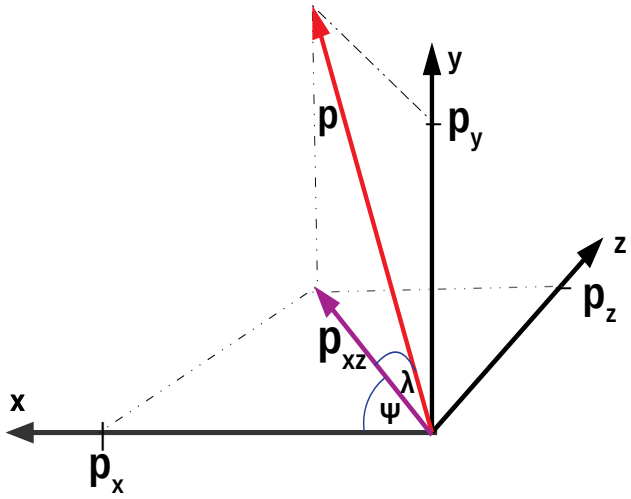

Figure 54: New momentum coordinate systems are introduced in s_x, s_y and ρ in terms of p_x, p_y, and p_{xz}. Where Ψ is the angle between p_{xz} and p_x, and λ is the angle between p_{xz} and p.

particles in the x-z plane. Thus, it is most convenient to express the momentum of each particle in the following momentum coordinates (Fig. 54):

$$\begin{aligned} s_x &= p_x/p_{xz} = cos(\Psi) \ , \\ s_y &= p_y/p_{xz} = sin(\lambda) \ , \\ \rho &= 1/p_{xz} \ , \end{aligned} \tag{10}$$

where $p_{xz} = \sqrt{p_x^2 + p_z^2}$. For each pair of particles, a difference in these coordinates is calculated as:

$$\begin{aligned} \Delta s_x &= s_{x,2} - s_{x,1} \ , \\ \Delta s_y &= s_{y,2} - s_{y,1} \ , \\ \Delta \rho &= \rho_2 - \rho_1 \ . \end{aligned} \tag{11}$$

The distributions of particle pairs' momentum difference for pairs with gTTD less than 2 cm (as an example for Ar+Sc at 75*A* GeV/*c*) are parameterized with ellipses (Eqs. 12) in the new momentum coordinates. Such parameterized elliptical cuts are defined as:

$$\begin{aligned} \left(\frac{\Delta\rho}{r_\rho}\right)^2 + \left(\frac{\Delta s_y}{r_{s_y}}\right)^2 &\leq 1 \ , \\ \left(\frac{\Delta s_x}{r_{s_x}}\right)^2 + \left(\frac{\Delta s_y}{r_{s_y}}\right)^2 &\leq 1 \ , \\ \left(\frac{\Delta\rho\cos\theta - \Delta s_x \sin\theta}{r_{\rho s_x}}\right)^2 + \left(\frac{\Delta\rho\sin\theta + \Delta s_x \cos\theta}{r_{s_x\rho}}\right)^2 &\leq 1 \ , \end{aligned} \tag{12}$$

where $r_{\rho s_x}$ and $r_{s_x \rho}$ is the semi-major and semi-minor axis of an ellipse formed by $\Delta\rho$ and Δs_x, and θ is the angle from the positive horizontal axis to the ellipse's major axis. Similarly, other semi-major and semi-minor axes of the other ellipses are also defined in Eqs. 12.

Proton pairs with momenta inside all the ellipses are rejected. The mTTD cut can replace the gTTD cut. Due to its momentum-based definition, the mTTD cut can be used for model comparison of the experimental results. The parameters of the mTTD cut (Eqs. 12) are given in Table 16 and the cut is used for the data analysis and comparison with the models. The effect of the mTTD cut for ^{40}Ar + ^{45}Sc collisions at beam momentum of 75*A* GeV/*c* mixed events and the Power-Law model is shown in Fig. 55. The dependence of $F_2(M)$ on M^2 in cumulative transverse-momentum space for $M^2 > 1$ is systematically below $F_2(M = 1)$ when gTTD or mTTD cut is applied to fully uncorrelated mixed events (*left*) and the Power-Law model with uncorrelated particles only (*right*).

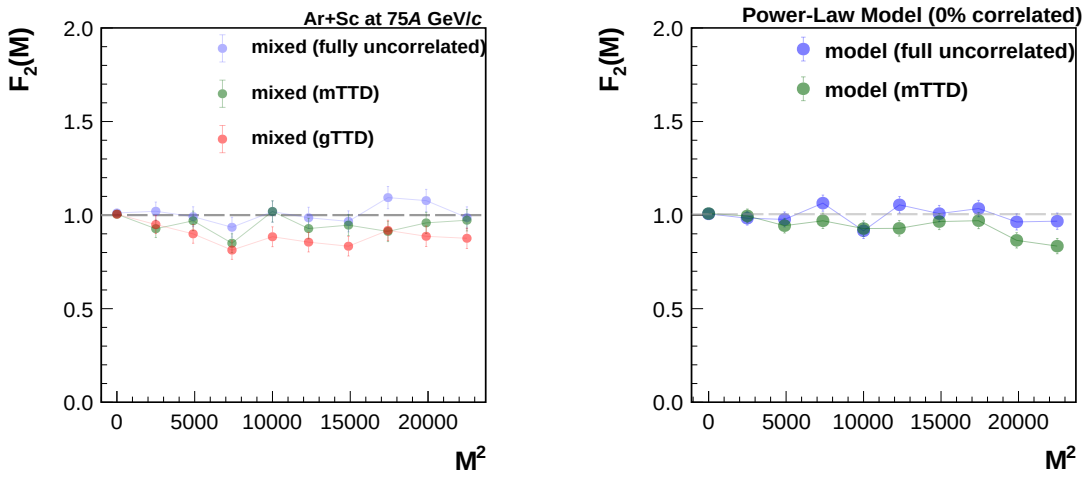

Figure 55: Example of the gTTD or mTTD cut impact on mixed events for ^{40}Ar + ^{45}Sc collisions at beam momentum of 75*A* GeV/*c* (*left*) and on the Power-Law model with uncorrelated particles only (*right*) are shown. The blue circles correspond to the dependence of $F_2(M)$ on M^2 where neither gTTD nor mTTD cut is applied to the mixed events or the Power-Law model. As indicated in the plot, the green and red points correspond to either gTTD or mTTD cut applied.

The momentum-based Two Track Distance (mTTD) cut was introduced in Sec. **??** with the help of the new momentum coordinate system (see Eqs. 10). The mTTD cut provides the precise definition of the biased region in which we don't have good efficiency for measuring two tracks and removes the remaining split tracks from the data after the potential point ratio cut. For each pair of selected proton candidates in both recorded and mixed events (see Sec. 9.1.1) for ^{208}Pb + ^{208}Pb collisions at beam momenta of 13*A* and 30*A* GeV/*c* and ^{40}Ar + ^{45}Sc collisions at beam momenta of 13*A*-75*A* GeV/*c*, the geometrical Two-Track Distance (gTTD) was calculated. It is the average distance of their tracks in x-y plane at eight different z planes (-506, -255, -201, -171, -125, 125, 352, and 742 cm). The TPC's limitation to recognizing close tracks is clearly visible in Fig 57 (*left*) for gTTD less than 2.2cm for ^{40}Ar + ^{45}Sc collisions at beam momentum of 75*A* GeV/*c*. The gTTD cut values for each data set are listed in Table 16.

Example distributions of the rejected protons by the gTTD cut for ^{40}Ar + ^{45}Sc collisions at beam momenta of 75*A* GeV/*c* are shown in Fig. 56. The ellipses were drawn by the red color used as a reference to tune the mTTD cut parameters.

Proton pairs with momenta inside all the parameterized ellipses (see Eqs. 12) are rejected

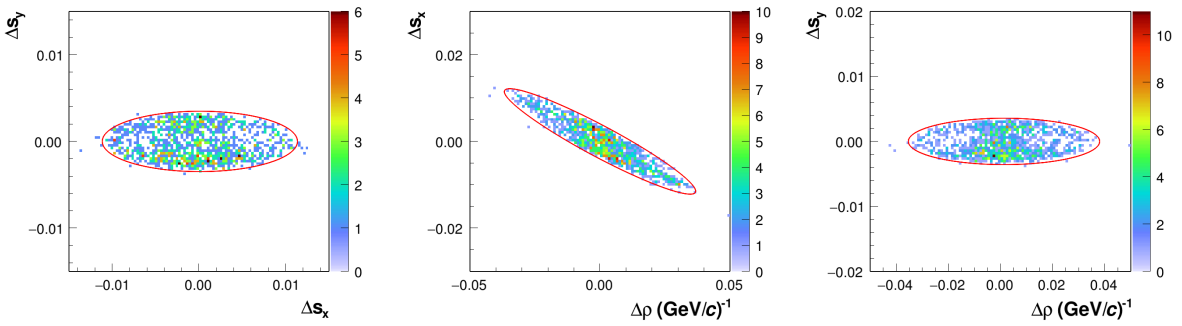

Figure 56: Example distributions of the rejected protons by the gTTD cut for ^{40}Ar + ^{45}Sc collisions at beam momentum of 75*A* GeV/*c*. Ellipses (see Eqs. 12) are drawn by a red color as a reference to tune the mTTD cut parameters (see Table 16).

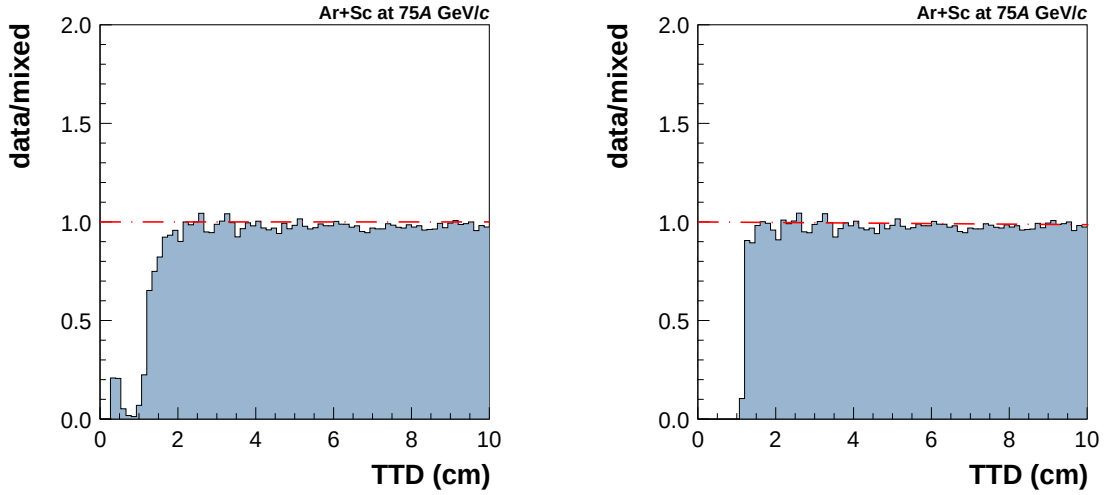

Figure 57: Example distributions of the TTD ratio of the experimental to mixed data before (*left*) and after (*right*) the mTTD cut for ^{40}Ar + ^{45}Sc collisions at beam momentum of 75*A* GeV/*c*.

and the mTTD cut parameters for ^{208}Pb + ^{208}Pb and ^{40}Ar + ^{45}Sc data sets are summarized in Table 16.

The two-particle acceptance used for proton intermittency analysis of ^{40}Ar + ^{45}Sc collisions at beam momentum of 75*A* GeV/*c* data analysis is shown in Fig. 57 (*right*).

The number of proton candidates that are rejected by the mTTD cuts for ^{208}Pb + ^{208}Pb and ^{40}Ar + ^{45}Sc data sets is listed in Table 16.

Due to its momentum-based definition, the mTTD cut can be used when comparing models with experimental results. The mTTD cut is used both for the data analysis and for calculating the model predictions.

Table 16: Numerical values of the mTTD cut parameters of the parameterized ellipses (see Eqs. 12) were used to analyze ^{40}Ar + ^{45}Sc collisions at beam momenta 13*A*- 75*A* GeV/*c*. Particle pairs with momenta inside all the ellipses are rejected.

p_{beam} (GeV/*c*)	gTTD cut (cm)	r_ρ	r_{s_y}	r_{s_x}	$r_{\rho s_x}$	$r_{s_x \rho}$	θ	# mTTD rejected tracks
^{208}Pb + ^{208}Pb data sets								
13A	5	0.089	0.009	0.009	0.089	0.009	6	1258
30A	6	0.102	0.009	0.022	0.102	0.002	13	1694
^{40}Ar + ^{45}Sc data sets								
13A	3.5	0.470	0.004	0.047	0.470	0.004	5	307
19A	2.8	0.121	0.003	0.010	0.121	0.003	8	371
30A	2.8	0.123	0.002	0.013	0.123	0.002	13	349
40A	2.2	0.043	0.002	0.010	0.043	0.002	15	306
75A	2.2	0.080	0.002	0.011	0.020	0.002	31	559

8.1 Two-particle correlation function

The two-particle correlation function, Δp_T of selected proton candidates within the analysis acceptance for ^{208}Pb + ^{208}Pb collisions at beam momentum of 13*A* GeV/*c* and ^{40}Ar + ^{45}Sc collisions at beam momenta of 13*A*-75*A* GeV/*c* is shown in Figs. 58 and 59. The correlation function is defined as the ratio of normalized Δp_T distributions for data and mixed events. The data distribution includes the mTTD cut, whereas the mixed one does not. The decrease of the correlation function at $\Delta p_T \approx 0$ is due to anti-correlation generated by the mTTD cut.

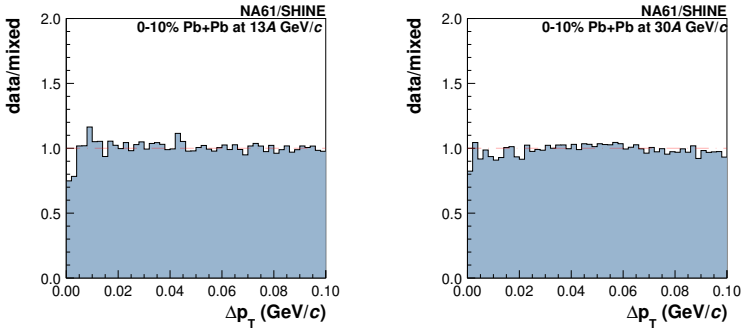

Figure 58: Examples two-particle correlation function in Δp_T for selected proton candidates within analysis acceptance for ^{208}Pb + ^{208}Pb collisions at beam momentum of 13*A* and 30*A* GeV/*c*. The data distribution includes the mTTD cut, whereas the mixed one does not.

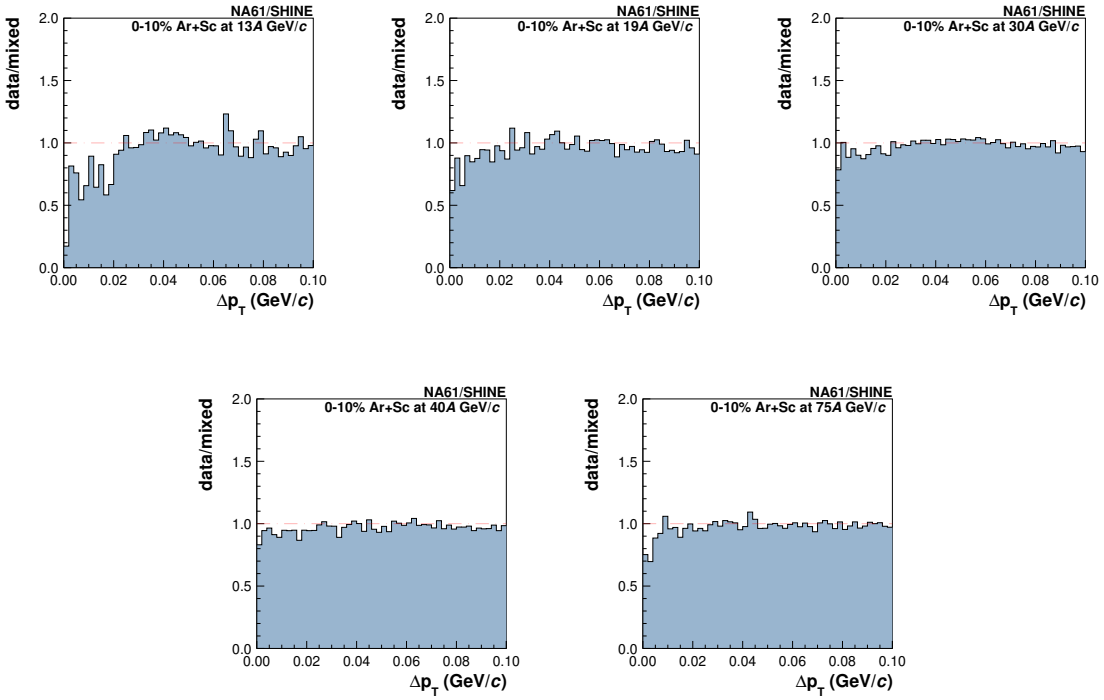

Figure 59: Examples two-particle correlation function in Δp_T for proton candidates within analysis acceptance for ^{40}Ar + ^{45}Sc collisions at beam momentum of 13*A*-75*A* GeV/*c*. The data distribution includes the mTTD cut, whereas the mixed one does not.

9 New approach to proton intermittency analysis

In the proton intermittency analysis presented here, only the second scaled factorial moment (SSFM) is taken into account due to the limited statistics. The SSFM, $F_2(M)$, can be obtained by setting $r = 2$ and for two-dimensional space of transverse momentum, $D = 2$ in Eq. 1:

$$F_2(M) = \frac{\left\langle \frac{1}{M^2} \sum_{i=1}^{M^2} n_i(n_i - 1) \right\rangle}{\left\langle \frac{1}{M^2} \sum_{i=1}^{M^2} n_i \right\rangle^2}, \tag{13}$$

where the transverse-momentum space is partitioned into $M \times M$ equal-size bins and n_i is the number of protons in the i-th bin. For a fixed value of M, the numerator and the denominator are averaged over bins and then over events. The NA49 experiment at CERN

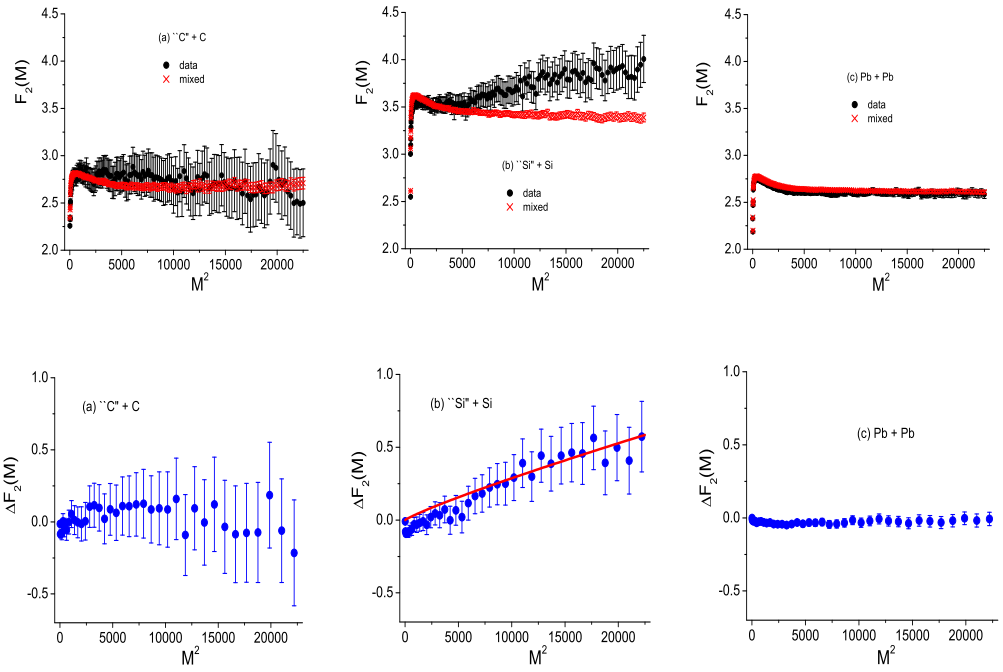

Figure 60: *Top:* $F_2(M)$ of protons in non-uniform transverse-momentum space at mid-rapidity for the most central collisions of (*a*) C+C (12%), (*b*) Si+Si (12%), and (*c*) Pb+Pb (10%) at $\sqrt{s_{NN}}$ ≈17.3 GeV [35]. The black circles (red crosses) represent $F_2(M)$ of the data (mixed events) respectively. *Bottom:* the background subtracted SSFMs, $\Delta F_2(M)$ for the most central collisions of (*a*) C+C (12%), (*b*) Si+Si (12%), and (*c*) Pb+Pb (10%) at $\sqrt{s_{NN}}$ ≈17.3 GeV are calculated using mixed event method. Statistical uncertainties were obtained using the Bootstrap method. Plots are taken from Ref. [35].

SPS searched for an intermittency signal in the production of protons [35] at mid-rapidity in a the transverse-momentum plane using the SSFM. The proton spectra in transverse momentum are non-uniform. Moreover, for each M point, the full set of data was used. Thus the results for different *M* are correlated. Statistical uncertainties were obtained using the Bootstrap method [51].

In this section, I'll discuss the new approach to proton intermittency analysis that the NA61/SHINE experiment uses to search for the QCD CP. The novelty comprises of:

(i) cumulative transformation method (Sec. 9.1.2),

(ii) independent sub-sample of events for each data point (Sec. 9.2),

(iii) analytical calculation of statistical uncertainties (Sec. 9.3),

9.1 Intermittency analysis of non-uniform distributions

The intermittency signal of CP will always be affected by various biasing effects. The most important one is due to the fact that SFMs are sensitive to the shape of the single-particle momentum distribution. This dependence biases the signal of critical fluctuations. In the past, the mixed event method was utilized to correct for the bias. Figure 60 (*top*) shows intermittency analysis results [35] of proton multiplicity at mid-rapidity in the most central (12%, 12%, and 10%) of C+C, Si+Si, and Pb+Pb collisions at beam momentum 158A GeV/c ($\sqrt{s_{NN}} \approx 17.3$ GeV) from the NA49 experiment. In these analyses, SSFMs were shown as a function of the number of sub-divisions in the transverse-momentum space. The black circles (red crosses) represent $F_2(M)$ of the data (mixed events). The background-subtracted SSFMs,

$$\Delta F_2(M) \approx F_2^{\text{data}}(M) - F_2^{\text{mixed}}(M), \tag{14}$$

were calculated to eliminate the bias due to non-uniform spectra using the mixed event method as shown in Fig 60 (*bottom*).

In our approach, the cumulative transformation technique is used to eliminate bias rather than the mixed event method. In the subsequent subsections, two methods are briefly discussed.

9.1.1 Mixed event method

In the case of the mixed event method, particles from different data events are used to generate mixed events. Figure 61 graphically shows the procedure for the random mixing of particles from different events. Each particle in each mixed event comes from a different data event.

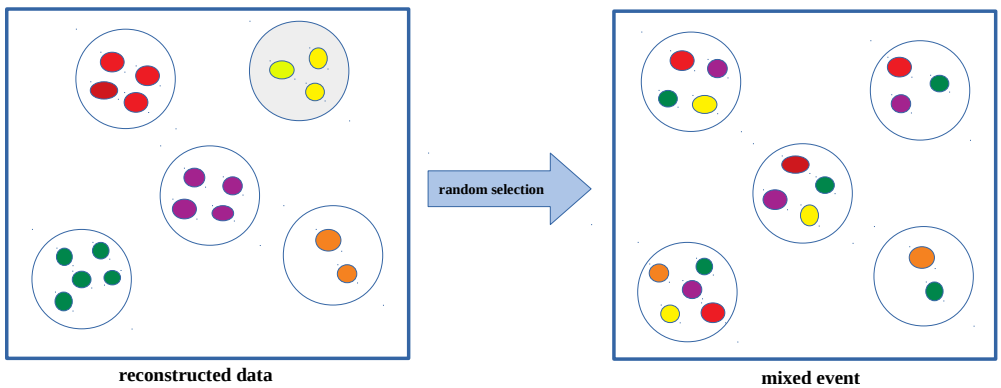

Figure 61: The procedure of random mixing of particles from different events is shown graphically to remove correlations between particles. Each open circle represents one event, and the colour circle corresponds to the track of that event. The *left* box for reconstructed data and *right* box for mixed events.

Mixed events are constructed in this way to remove all correlations between particles. By

construction, the multiplicity distribution of the data and mixed events are identical. Figure 63 (red circles) shows the dependence of the SSFMs on the number of sub-division for mixed events constructed using the Power-Law Model [37] setting the intermittency index to ϕ_2 = 0.83 for r =2.

It was shown [35] that this procedure approximately removes the dependence of $\Delta F_2(M)$ on the shape of a single-particle distribution.

9.1.2 Cumulative transformation method

As it is discussed, the experimental results on $F_2(M)$ do depend on the shape of the single particle distribution and on the choice of variables used for analysis. Bialas and Gazdzicki [33] proposed to study intermittency in terms of variables for which the single-particle density is constant. It was also shown [33] that this method reduces the bias caused by a non-uniform single-particle distribution leaving the CP signal unchanged. In this analysis note, the suggested new variables are referred to as the *cumulative* variables.

Assume that the single particle distribution in a variable x is measured and given by a (non-negative) function $f(x)$. For a one dimensional distribution $f(x)$, the cumulative variable, Q_x, is defined as:

$$Q_x = \int_a^x f(x')dx' \Big/ \int_a^b f(x')dx' \,, \tag{15}$$

where a and b are lower and upper limits of the variable x. For a two-dimensional distribution $f(x, y)$ and a given x the cumulative transformation defined as:

$$Q_y(x) = \int_a^y f(x, y')dy' \Big/ \int_a^b f(x, y')dy'. \tag{16}$$

The cumulative variable has the following properties:

(i) its value depends on the ordering of particles in x, and thus it is the same for all variables which preserve the ordering,

(ii) the single-particle distribution in the cumulative variable is uniform, and it ranges from 0 to 1.

The property (i) gives a new way to compare the results obtained in different experiments. The property (ii) removes the dependence of the intermittency parameters on the shape of the single-particle distribution. At the same time, it has been verified [52] that the transformation preserves the critical behaviour is given by Eq. 2, at least for the SSFMs.

An example of the cumulative transformation of transverse-momentum components, p_x and p_y generated from the Power-Law Model, is shown in Fig 62 where distributions before (*top*) and after (*bottom*) the transformation are shown. Figure 63 shows the dependence of SSFMs on the number of sub-divisions in the cumulative-transformed transverse-momentum plane using data generated within the Power-Law Model.

9.2 Statistically-independent data points

The intermittency analysis gives the dependence of scaled-factorial moments on the number of sub-divisions of transverse momentum or cumulative-transverse-momentum intervals. In the past intermittency analyses, the same data set was used to obtained results for each number of subdivisions (see Fig. 60). The results for different *M* are statistically correlated. Therefore

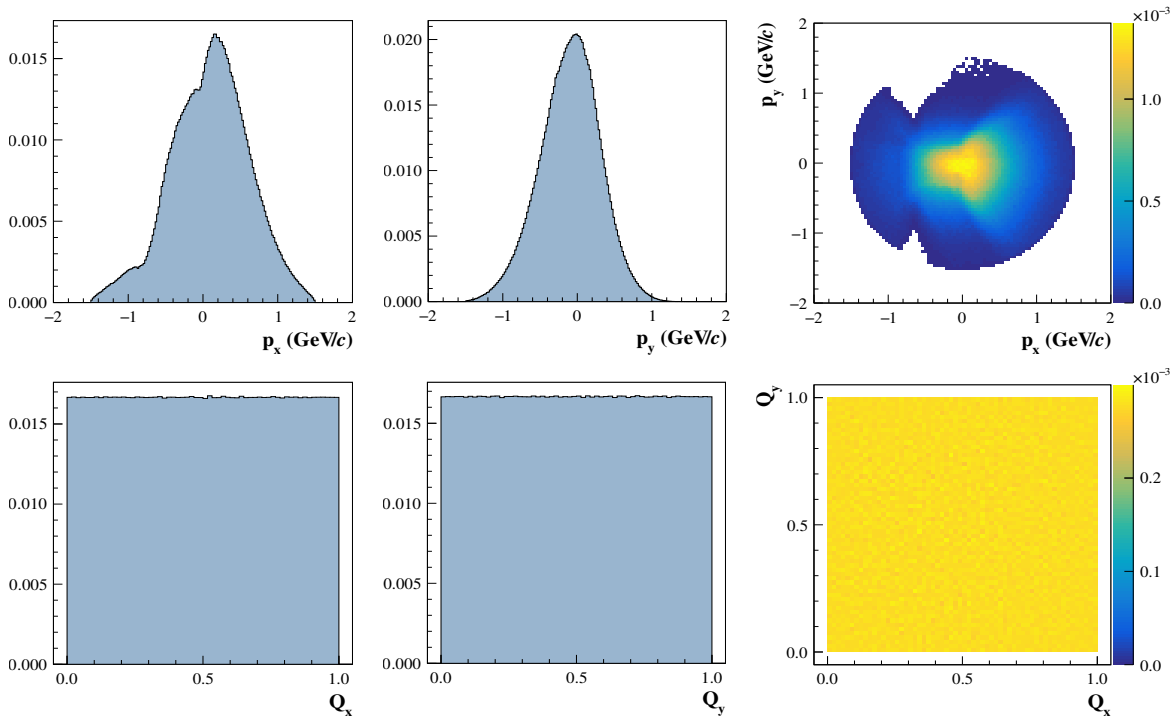

Figure 62: Example of the effect of the cumulative transformation of transverse-momentum components, p_x and p_y, generated from the Power-Law Model [32]. Distributions before (*top*) and after (*bottom*) the transformation.

the full covariance matrix is required for proper statistical treatment of the results. This is numerically not trivial [53].

Here, statistically-independent subsets of data events are used to obtain results for each sub-division number. In this case, the results for different sub-division numbers are statistically independent. Thus only diagonal elements of the covariance matrix are non-zero, and the complete relevant information needed to interpret the results is easy to present graphically. However, this procedure decreases the number of events used to calculate each data point increasing statistical uncertainties. The number of events used in each subset was selected to obtain similar values of the statistical uncertainties of results for different subsets. Table 17 shows the fraction of all available events used to calculate each of the 10 points.

Table 17: Fraction of the total number of analyzed events used to calculate second-order scaled factorial moments for the chosen number of cumulative momentum bins.

number of bins (M^2)	1^2	50^2	70^2	86^2	100^2	111^2	122^2	132^2	141^2	150^2
fraction of all events (%)	0.5	3.0	5.0	7.0	9.0	11.0	13.0	15.5	17.0	19.0

Figure 63 illustrates an example of intermittency analysis using SSFM for a critical system utilizing the new approach with data generated by the Power-Law Model and mixed events. Statistically-independent data subsets are used to obtain results for each sub-division number.

9.3 Statistical uncertainties

Statistical uncertainties in the intermittency analysis (see Fig. 60) of the NA49 experiments were calculated using the Bootstrap method [51]. Here, statistical uncertainties are calculated

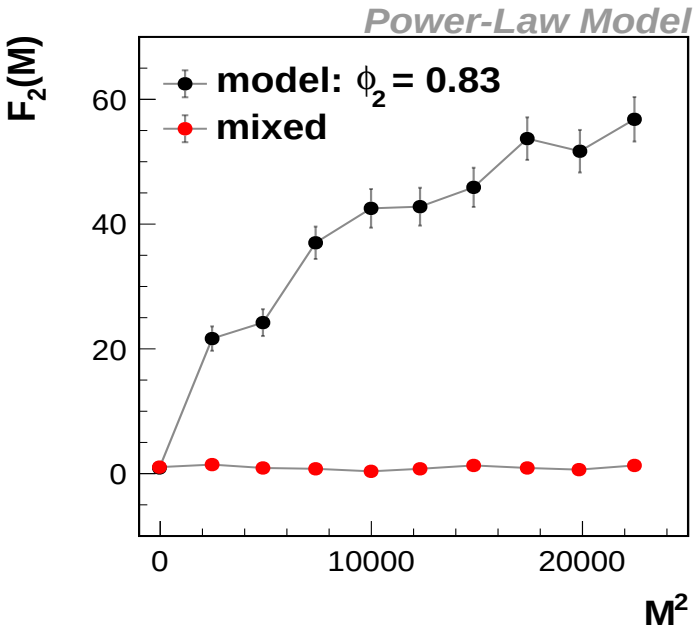

Figure 63: The dependence of the SSFMs of particle multiplicity distribution on the number of sub-divisions in cumulative transverse-momentum space. Independent sub-samples are used for each data point. Black and red circles indicate model and mixed events, respectively. Calculations were performed using the Power-Law Model [32] with intermittency index, ϕ_2 = 0.83 for r = 2. Statistical uncertainties are calculated using statistical uncertainty propagation.

analytically. Below the new approach is briefly presented.

The standard expression for the SSFM, Eq. 13, can be rewritten as

$$F_2(M) = 2M^2 \frac{\langle N_2(M) \rangle}{\langle N \rangle^2}, \tag{17}$$

where N and $N_2(M)$ denote the total number of protons and proton pairs, respectively, in M bins in an event.

With the help of the modified SSFM expression, Eq 17, the statistical uncertainties can be calculated using the statistical uncertainty propagation:

$$\frac{\sigma_{F_2}}{|F_2|} = \sqrt{\frac{(\sigma_{N_2})^2}{\langle N_2 \rangle^2} + 4\frac{(\sigma_N)^2}{\langle N \rangle^2} - 4\frac{(\sigma_{N_2 N})^2}{\langle N \rangle \langle N_2 \rangle}}\,. \tag{18}$$

Statistical uncertainties shown in Fig. 63 are calculated using this method. It has been found that the statistical uncertainties derived from each of the methodologies are similar. However, the new approach, which utilizes statistical uncertainty propagation (Eq. 18), is easy to implement and fast.

10 Proton intermittency results

This section presents results on second-order scaled-factorial moments, $F_2(M)$ (see Eq. 1) of selected proton candidates (see Sec. 6.6) produced within the analysis acceptances by strong and electromagnetic interactions in 0-10% of the most central ^{208}Pb + ^{208}Pb collisions at beam momenta of 13*A*, and 30*A* GeV/*c* and ^{40}Ar + ^{45}Sc collisions at beam momenta of 13*A*, 19*A*, 30*A*, 40*A*, and 75*A* GeV/*c*. The results are shown as a function of the number of subdivisions (*M*) in transverse-momentum space - - the so-called intermittency analysis. The analysis was performed for cumulative and original (or non-cumulative) transverse-momentum components. Independent data sets were used to calculate results for each subdivision. Statistical uncertainties are calculated using statistical uncertainty propagation, Eq. 18 (see Sec. 9.3). The dependence of $F_2(M)$ on *M* is obtained for the maximum subdivision number of *M* = 150 and *M* = 32. The latter, the coarse subdivision, was introduced to limit the effect of experimental momentum resolution [55].

10.1 Results for subdivisions in non-cumulative transverse-momentum space

The results on $F_2(M)$ and $\Delta F_2(M)$ (see Eq. 14) for subdivisions in non-cumulative transverse-momentum space are shown in Figs. 64 - 70. The results shown in Figs. 64 and 68 correspond to fine binning (*M* up to 150), whereas the results shown in Figs. 66 and 70 correspond to coarse binning (*M* up to 32). The mTTD cut for both data and mixed events. The values of the cut parameters are given in Table 16.

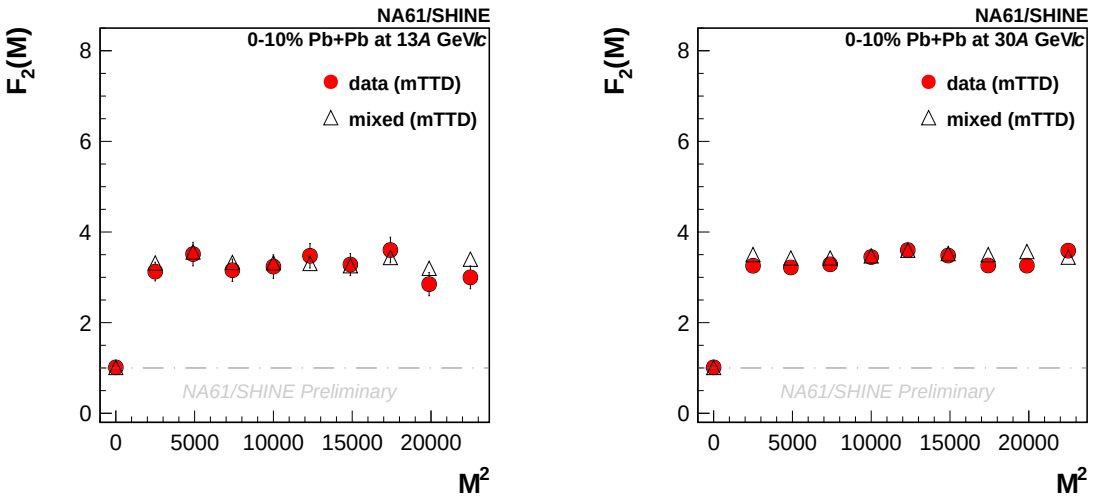

Figure 64: Results on the dependence of the scaled-factorial moment of proton multiplicity distribution on the number of subdivisions in transverse-momentum space *M* for $1 \leq M \leq 150$. Results for $0 - 10\%$ central ^{208}Pb + ^{208}Pb collisions at beam momentum of 13*A* (*left*) and 30*A* GeV/*c* (*right*). Closed red circles indicate the experimental data. Corresponding results for mixed events (open triangles) are also shown. Both the data and mixed events include the mTTD cut. Only statistical uncertainties are indicated.

The red closed circles indicate the experimental data. For comparison, corresponding results for mixed events (see Sec. 9.1.1) are shown by the grey triangles. Note that by

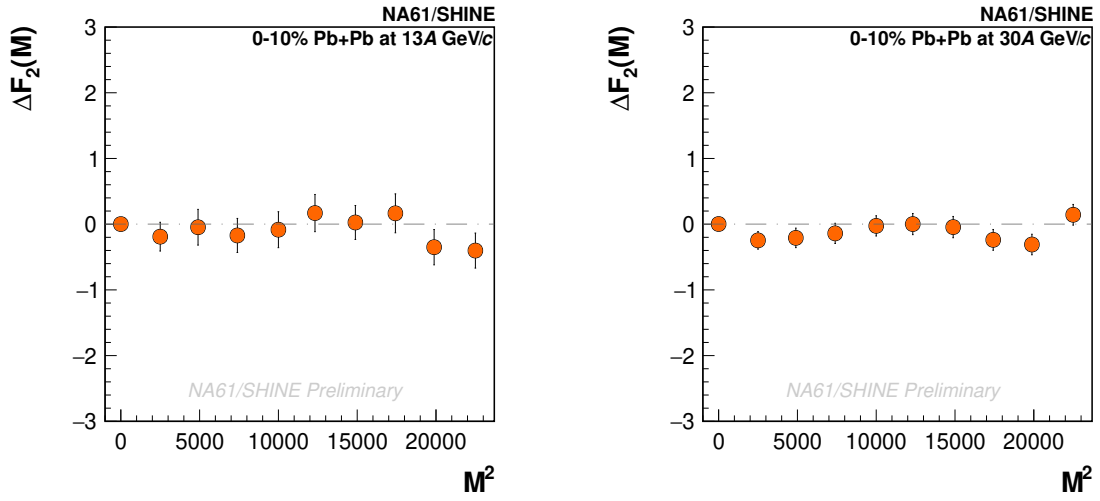

Figure 65: Results on the dependence of $\Delta F_2(M) \approx F_2^{data}(M) - F_2^{mixed}(M)$ of proton multiplicity distribution on the number of subdivisions in transverse-momentum space M for $1 \leq M \leq 150$. Results for $0-10\%$ central ^{208}Pb + ^{208}Pb collisions at beam momentum of 13A (*left*) and 30A GeV/c (*right*), respectively. Both the data and mixed events include the mTTD cut. Only statistical uncertainties are indicated.

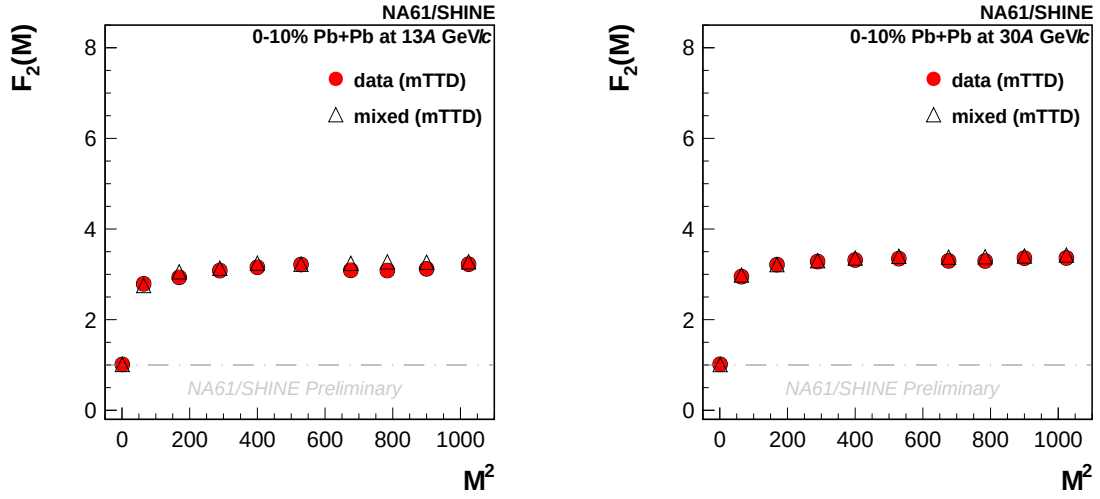

Figure 66: Results on the dependence of the scaled-factorial moment of proton multiplicity distribution on the number of subdivisions in transverse-momentum space M for $1 \leq M \leq 32$. Results for $0-10\%$ centrality selection of events are presented for ^{208}Pb + ^{208}Pb interaction at 13A (*left*) and 30A GeV/c (*right*). Closed red circles indicate the experimental data. Corresponding results for mixed events (open triangles) are also shown. Both the data and mixed events include the mTTD cut. Only statistical uncertainties are indicated.

construction, the multiplicity distribution of protons in mixed events for $M = 1$ equals the corresponding distribution for the data. In mixed events, the only correlation of particles in

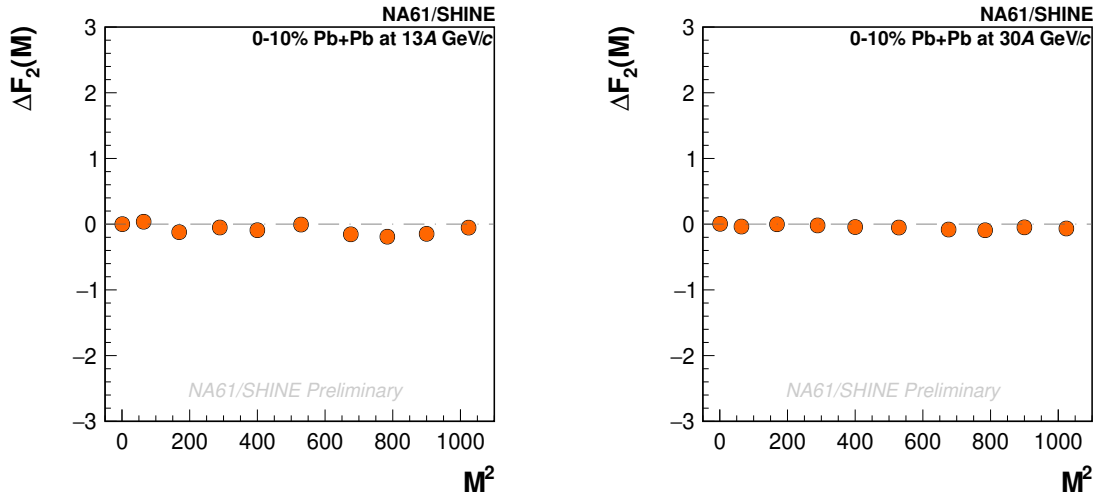

Figure 67: Results on the dependence of $\Delta F_2(M) \approx F_2^{data}(M) - F_2^{mixed}(M)$ of proton multiplicity distribution on the number of subdivisions in transverse-momentum space M for $1 \leq M \leq 32$. Results for $0-10\%$ central ^{208}Pb + ^{208}Pb collisions at beam momentum of 13A (*left*) and 30A GeV/c (*right*), respectively. Both the data and mixed events include the mTTD cut. Only statistical uncertainties are indicated.

the transverse-momentum space is due to the mTTD cut. Both the data and mixed events include the mTTD cut. Only statistical uncertainties are indicated. The horizontal dotted line represents the reference line at $F_2(1)$.

By construction, $F_2(1)$ values are equal for subdivisions in cumulative transverse-momentum space and non-cumulative transverse-momentum space. But for the latter, $F_2(M)$ strongly depends on M^2. This dependence is primarily due to the non-uniform shape of the single-particle transverse-momentum distributions (see Sec. 9.1.2). It can be accounted for by comparing the experimental data results with those obtained for the mixed events (see Sec. 9.1.1) using $\Delta F_2(M) \approx F_2^{data}(M) - F_2^{mixed}(M)$ [56]. The dependence of $\Delta F_2(M)$ on the number of sub-divisions shown in Figs. 65, 69 and 67, 71 for fine and coarse binning.

The experimental results presented in Figs. 64 - 71 do not show any significant difference to the results for mixed events with the mTTD cut on M ($\Delta F_2(M) \approx 0$). There is no indication of the critical fluctuations for selected protons. The numerical values of proton intermittency in transverse-momentum space for ^{208}Pb + ^{208}Pb collisions at beam momentum 13A and 30A GeV/c and ^{40}Ar + ^{45}Sc collisions at beam momenta of 13A, 19A, 30A, 40A, and 75A GeV/c are presented in Tables 18 and 19.

10.2 Results for subdivisions in cumulative transverse-momentum space

Figures 72, 74 and 73, 75 present the dependence of $F_2(M)$ on M in cumulative transverse-momentum space for the maximum subdivision number of M = 150 and M = 32, respectively. The experimental results are shown for 0-10% central ^{208}Pb + ^{208}Pb collisions at beam momentum of 13A, and 30A GeV/c and ^{40}Ar + ^{45}Sc collisions at beam momenta of 13A, 19A, 30A, 40A, and 75A GeV/c. As a reference, the corresponding results for mixed events are also shown. For the mixed events, the second scaled-factorial moment is independent of M, $F_2(M) = F_2(1)$.

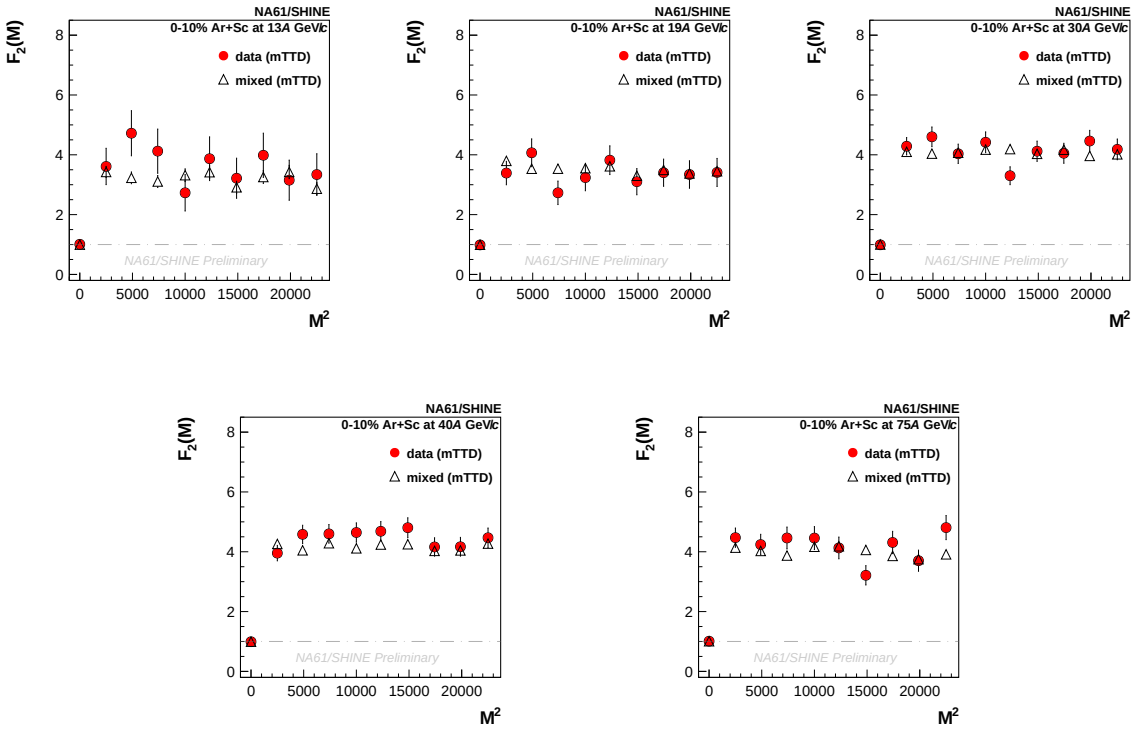

Figure 68: Results on the dependence of the scaled-factorial moment of proton multiplicity distribution on the number of subdivisions in transverse-momentum space M for $1 \leq M \leq 150$. Results for $0 - 10\%$ central ^{40}Ar + ^{45}Sc collisions at beam momenta of 13A, 19A, 30A, 40A, and 75A GeV/c, respectively. Closed red circles indicate the experimental data. Corresponding results for mixed events (open triangles) are also shown. Both the data and mixed events include the mTTD cut. Only statistical uncertainties are indicated.

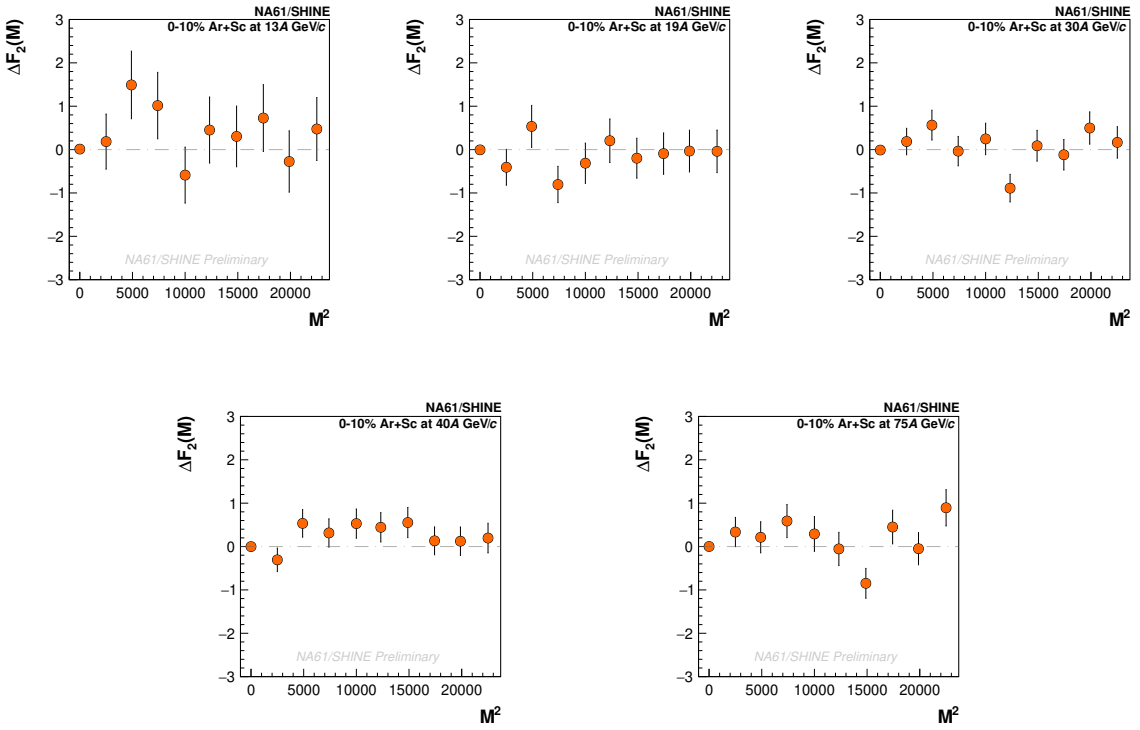

Figure 69: Results on the dependence of $\Delta F_2(M) \approx F_2^{data}(M) - F_2^{mixed}(M)$ of proton multiplicity distribution on the number of subdivisions in transverse-momentum space M for $1 \leq M \leq 150$. Results for $0 - 10\%$ central ^{40}Ar + ^{45}Sc collisions at beam momenta of 13A, 19A, 30A, 40A, and 75A GeV/c, respectively. Both the data and mixed events include the mTTD cut. Only statistical uncertainties are indicated.

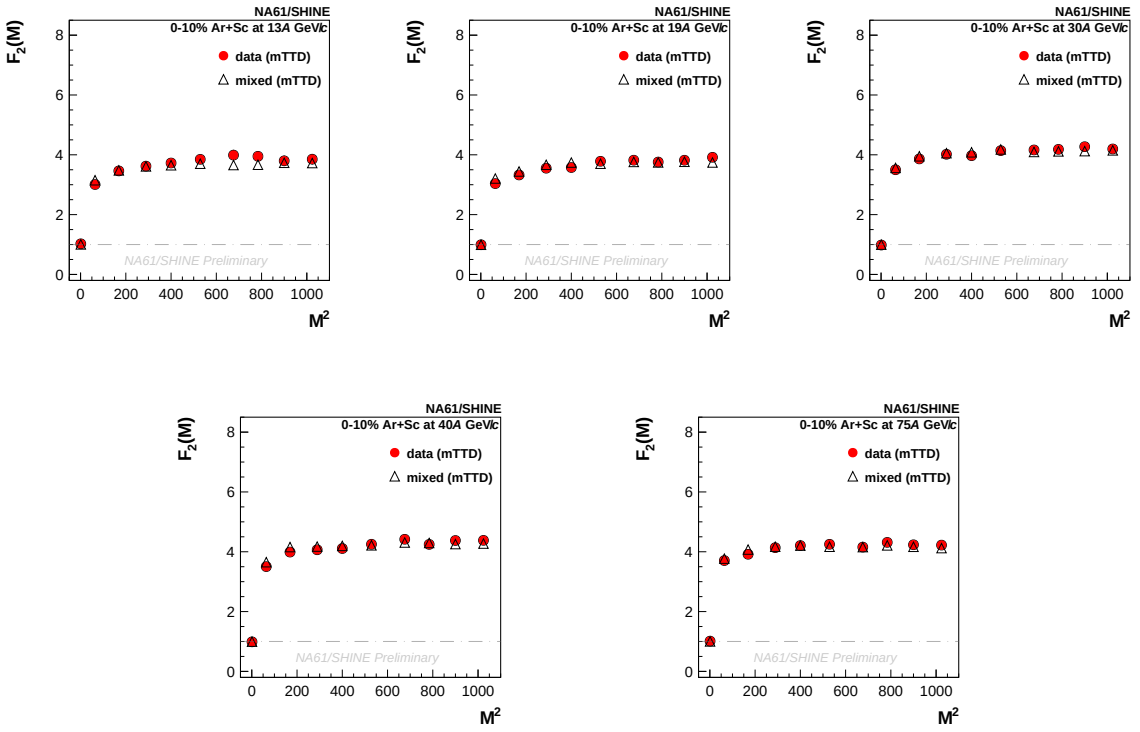

Figure 70: Results on the dependence of the scaled-factorial moment of proton multiplicity distribution on the number of subdivisions in transverse-momentum space M for $1 \leq M \leq 32$. Results for $0 - 10\%$ central ^{40}Ar + ^{45}Sc collisions at beam momenta of 13A, 19A, 30A, 40A, and 75A GeV/c, respectively. Closed red circles indicate the experimental data. Corresponding results for mixed events (open triangles) are also shown. Both the data and mixed events include the mTTD cut. Only statistical uncertainties are indicated.

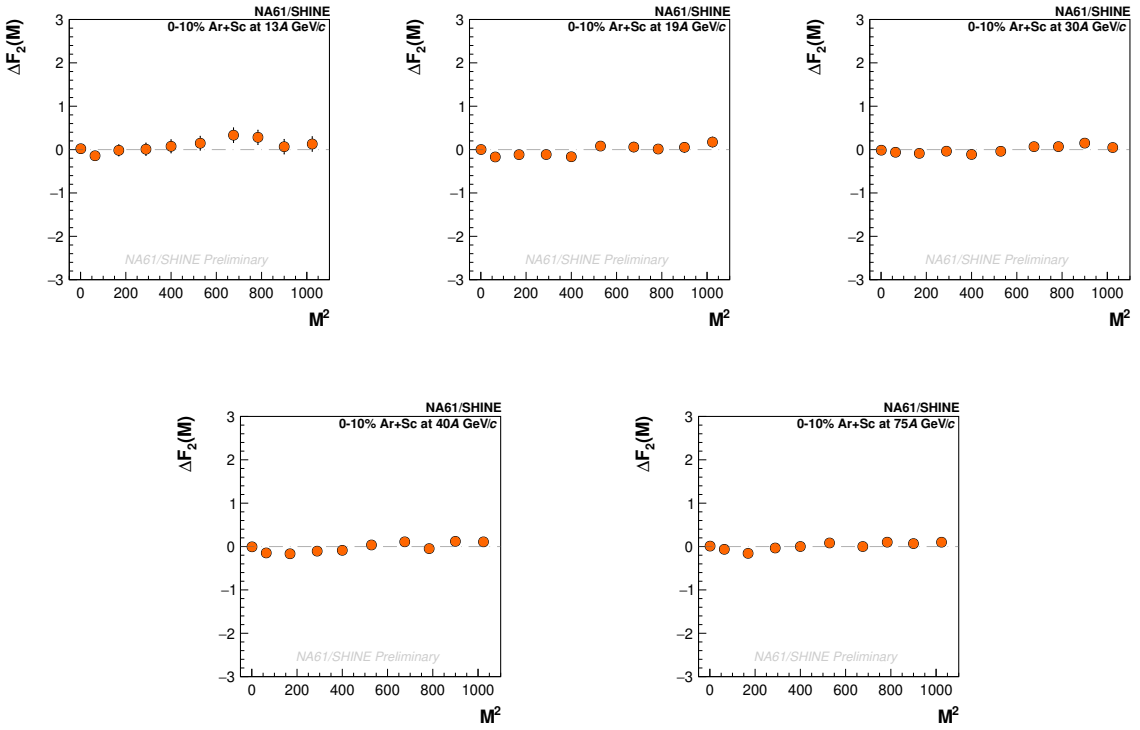

Figure 71: Results on the dependence of $\Delta F_2(M) \approx F_2^{data}(M) - F_2^{mixed}(M)$ of proton multiplicity distribution on the number of subdivisions in transverse-momentum space M for $1 \leq M \leq 32$. Results for $0 - 10\%$ central ^{40}Ar + ^{45}Sc collisions at beam momenta of 13A, 19A, 30A, 40A, and 75A GeV/c, respectively. Both the data and mixed events include the mTTD cut. Only statistical uncertainties are indicated.

The numerical values of proton intermittency in cumulative transverse-momentum space for ^{208}Pb + ^{208}Pb collisions at beam momentum 13*A* and 30*A* GeV/*c* and ^{40}Ar + ^{45}Sc collisions at beam momenta of 13*A*, 19*A*, 30*A*, 40*A*, and 75*A* GeV/*c* are presented in Tables 20 and 21. The results for subdivisions in cumulative transverse-momentum space, $F_2(M)$ for $M > 1$, are systematically below $F_2(M = 1)$. It is probably due to the anti-correlation generated by the mTTD cut to the data. The effect of the mTTD cut on the results for mixed events is shown in Fig. 55. Based on the findings, it is evident that when *M* is greater than one, the values of $F_2(M)$ are systematically below $F_2(M = 1)$ in cumulative transverse-momentum space when the mTTD or gTTD cut is applied to the mixed events. Note that the mTTD cut is necessary to properly account for the detector losses of close-in-space tracks (see Sec. **??**).

The experimental results show only a slight decrease of $F_2(M)$ with *M*. There is no indication of the critical fluctuations for selected proton candidates.

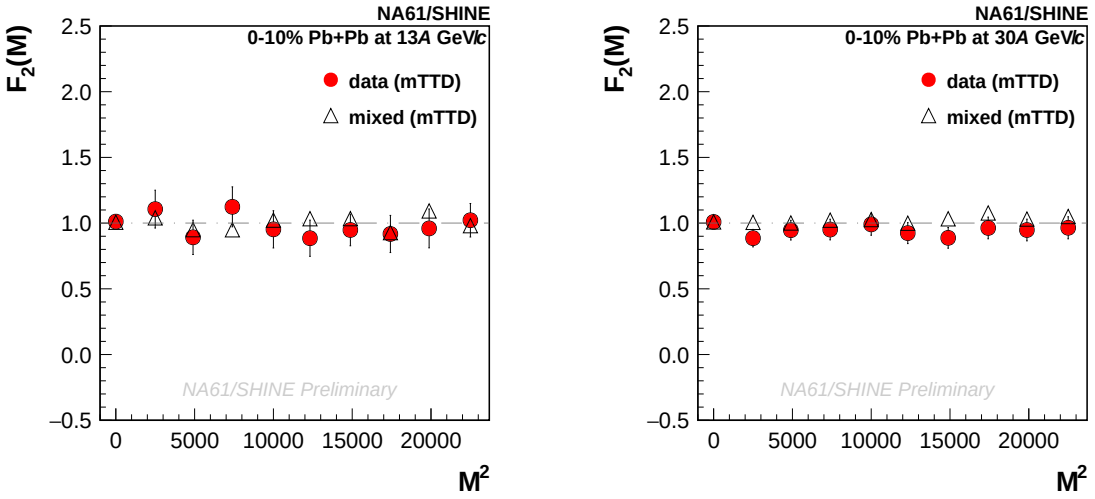

Figure 72: Results on the dependence of the scaled-factorial moment of proton multiplicity distribution on the number of subdivisions in cumulative transverse-momentum space *M* for $1 \leq M \leq 150$. Results for $0 - 10\%$ central ^{208}Pb + ^{208}Pb collisions at beam momentum of 13*A* (*left*) and 30*A* GeV/*c* (*right*). Closed red circles indicate the experimental data. Corresponding results for mixed events (open triangles) are also shown. Both the data and mixed events include the mTTD cut. Only statistical uncertainties are indicated.

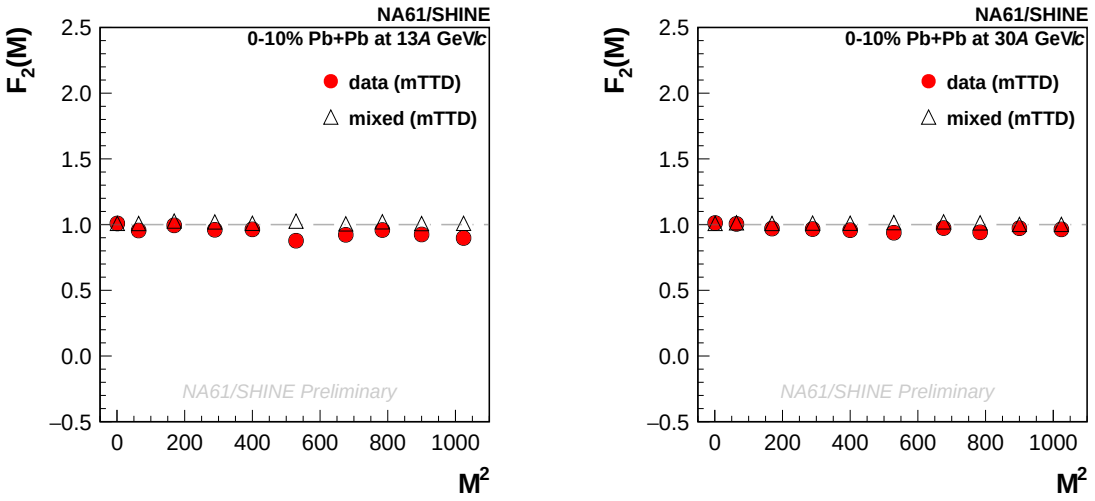

Figure 73: Results on the dependence of the scaled-factorial moment of proton multiplicity distribution on the number of subdivisions in cumulative transverse-momentum space M for $1 \leq M \leq 32$. Results for $0 - 10\%$ central ^{208}Pb + ^{208}Pb collisions at beam momentum of 13A (*left*) and 30A GeV/c (*right*). Closed red circles indicate the experimental data. Corresponding results for mixed events (open triangles) are also shown. Both the data and mixed events include the mTTD cut. Only statistical uncertainties are indicated.

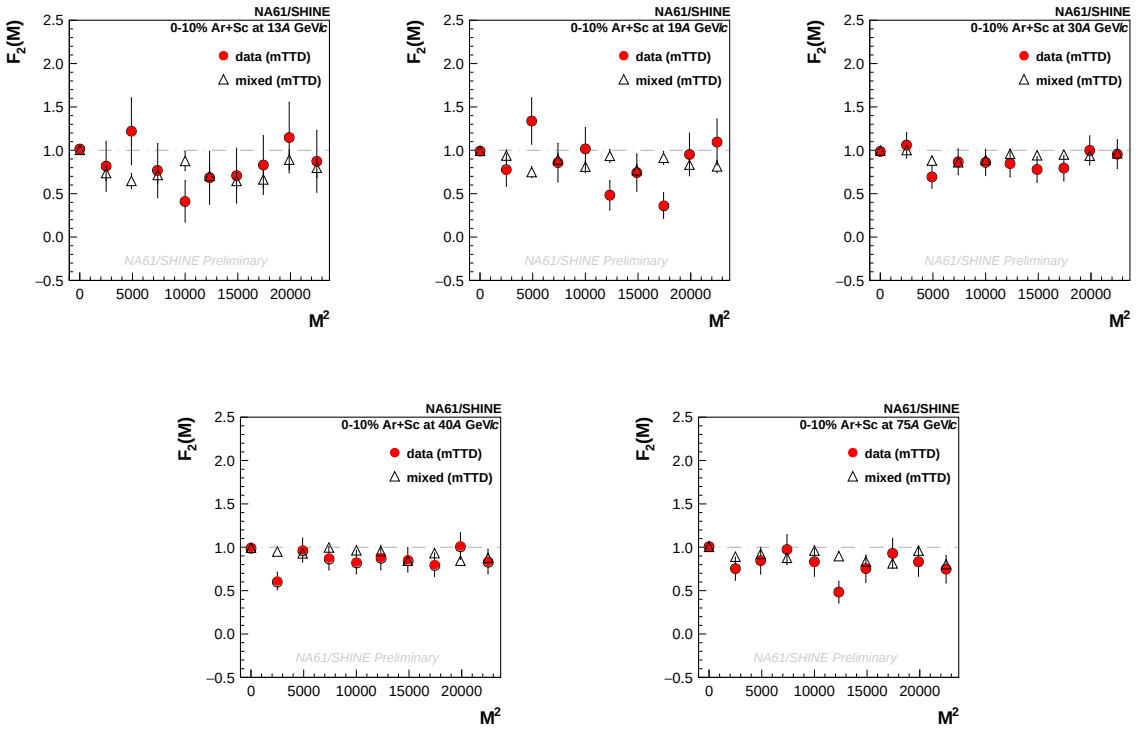

Figure 74: Results on the dependence of the scaled-factorial moment of proton multiplicity distribution on the number of subdivisions in cumulative transverse-momentum space M for $1 \leq M \leq 150$. Results for $0-10\%$ central ^{40}Ar + ^{45}Sc collisions at beam momenta of 13A, 19A, 30A, 40A, and 75A GeV/c, respectively. Closed red circles indicate the experimental data. Corresponding results for mixed events (open triangles) are also shown. Both the data and mixed events include the mTTD cut. Only statistical uncertainties are indicated.

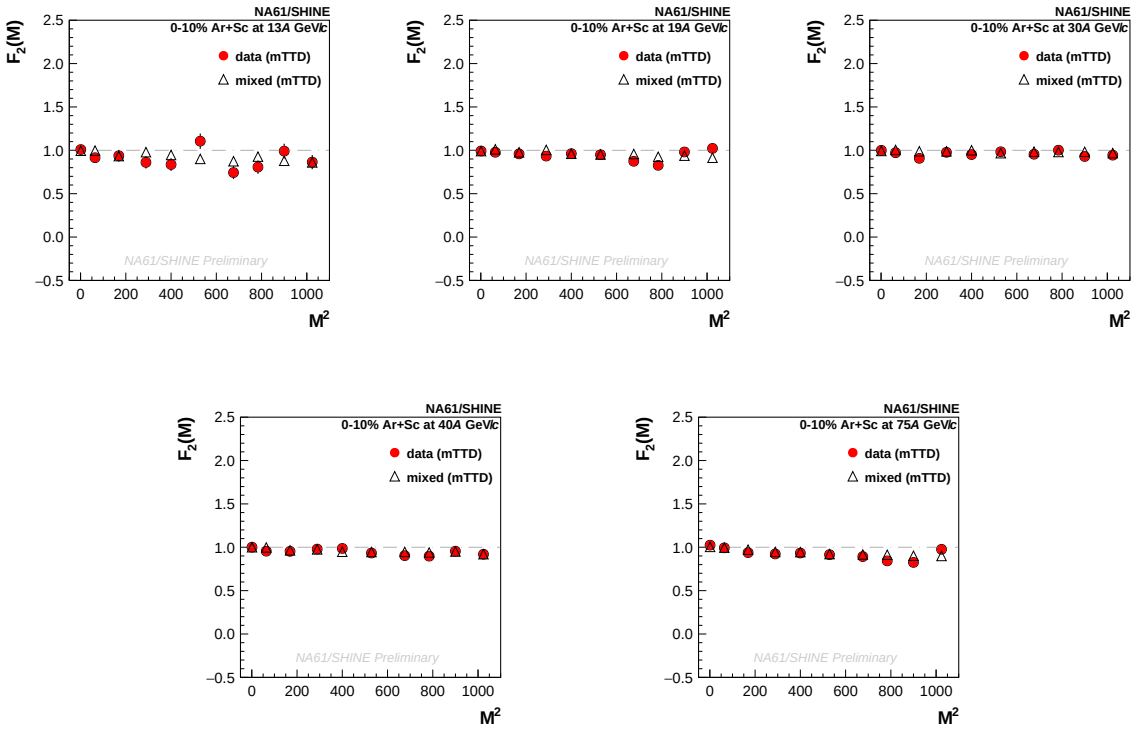

Figure 75: Results on the dependence of the scaled-factorial moment of proton multiplicity distribution on the number of subdivisions in cumulative transverse-momentum space M for $1 \leq M \leq 32$. Results for $0-10\%$ central ^{40}Ar + ^{45}Sc collisions at beam momenta of 13A, 19A, 30A, 40A, and 75A GeV/c, respectively. Closed red circles indicate the experimental data. Corresponding results for mixed events (open triangles) are also shown. Both the data and mixed events include the mTTD cut. Only statistical uncertainties are indicated.

Table 18: Numerical values of the results for ^{208}Pb + ^{208}Pb collisions at 13*A* GeV/*c* and 30*A* GeV/*c* presented in Figs. 64 and 66 are tabulated. The subdivisions are in non-cumulative transverse-momentum space. The *left* table corresponds to fine binning, $1 \leq M \leq 150$ and the right table corresponds to coarse binning, $1 \leq M \leq 32$. The statistical uncertainties, σ_{F_2} are also shown.

non-cumulative and fine binning					non-cumulative and coarse binning				
	13*A* GeV/*c*		30*A* GeV/*c*			13*A* GeV/*c*		30*A* GeV/*c*	
M	$F_2(M)$	σ_{F_2}	$F_2(M)$	σ_{F_2}	*M*	$F_2(M)$	σ_{F_2}	$F_2(M)$	σ_{F_2}
1	1.0127	0.0069	1.0133	0.0041	1	1.0118	0.0068	1.0145	0.0046
50	2.5263	0.2062	3.2553	0.1267	8	2.7906	0.0380	2.9483	0.02409
70	3.5126	0.2595	3.2176	0.1414	13	2.9334	0.0459	3.2134	0.02831
86	2.9856	0.2601	3.2864	0.1461	17	3.0828	0.0509	3.2818	0.03034
100	3.2372	0.2455	3.1474	0.1463	20	3.1554	0.0529	3.3159	0.0312
111	3.4750	0.2701	3.3007	0.1530	23	3.2161	0.0553	3.3463	0.0323
122	2.7120	0.2440	3.3802	0.1540	26	3.0891	0.0571	3.2963	0.0332
132	3.6026	0.2834	3.2611	0.1502	28	3.0838	0.0555	3.2948	0.0330
141	2.8489	0.2551	3.0581	0.1479	30	3.1205	0.0577	3.3564	0.0335
150	2.7787	0.2515	2.9885	0.1492	32	3.2232	0.0586	3.3609	0.0342

Table 19: Numerical values of the results for ^{40}Ar + ^{45}Sc collisions at 13*A*-75*A* GeV/*c* presented in Figs. 68 and 70 are tabulated. The subdivisions are in non-cumulative transverse-momentum space. The *top* table corresponds to fine binning, $1 \leq M \leq 150$ and the *bottom* table corresponds to coarse binning, $1 \leq M \leq 32$. The statistical uncertainties, σ_{F_2} are also shown.

	non-cumulative and fine binning									
	13*A* GeV/*c*		19*A* GeV/*c*		30*A* GeV/*c*		40*A* GeV/*c*		75*A* GeV/*c*	
M	$F_2(M)$	σ_{F_2}	$F_2(M)$	σ_{F_2}	$F_2(M)$	σ_{F_2}	$F_2(M)$	σ_{F_2}	$F_2(M)$	σ_{F_2}
1	1.0081	0.0162	0.9863	0.0102	0.9901	0.0065	0.9914	0.0063	1.0090	0.0082
50	3.6106	0.6074	3.3898	0.3917	4.2859	0.2912	3.9545	0.2582	4.4718	0.3221
70	4.7210	0.7543	4.0678	0.4649	4.6021	0.3295	4.5818	0.3047	4.2405	0.3427
86	4.1219	0.7393	2.7299	0.3934	4.0345	0.3232	4.5985	0.3119	4.4609	0.3671
100	2.7299	0.6100	3.2382	0.4402	4.4189	0.3474	4.6435	0.3229	4.4572	0.3840
111	3.8691	0.7306	3.8201	0.4807	3.3006	0.2997	4.6843	0.3250	4.1286	0.3644
122	3.2168	0.6703	3.1009	0.4382	4.1199	0.3393	4.8042	0.3327	3.2122	0.3242
132	3.9844	0.7394	3.4019	0.4542	4.0509	0.3348	4.1608	0.3064	4.3107	0.3720
141	3.1513	0.6715	3.3416	0.4586	4.4603	0.3567	4.1673	0.3130	3.7012	0.3527
150	3.3401	0.6962	3.4104	0.4681	4.1819	0.3469	4.4678	0.3273	4.8076	0.4031
	non-cumulative and coarse binning									
1	1.0241	0.0169	0.9924	0.0092	0.9823	0.0067	0.9877	0.0062	1.0119	0.0077
8	3.0068	0.0920	3.0378	0.0614	3.5003	0.0456	3.5035	0.0407	3.7058	0.0504
13	3.4613	0.1232	3.3261	0.0796	3.8625	0.0576	3.9894	0.0538	3.9157	0.0634
17	3.6205	0.1355	3.5516	0.0897	4.0170	0.0646	4.0664	0.0595	4.1359	0.0710
20	3.7256	0.1443	3.5753	0.0934	3.9707	0.0668	4.1082	0.0607	4.2068	0.0739
23	3.8482	0.1524	3.7829	0.1002	4.1394	0.0694	4.2511	0.0643	4.2496	0.0779
26	3.9897	0.1608	3.8198	0.1044	4.1624	0.0733	4.4173	0.0688	4.1551	0.0794
28	3.9498	0.1567	3.7577	0.1034	4.1818	0.0722	4.2456	0.0662	4.3129	0.0794
30	3.7991	0.1597	3.8186	0.1045	4.2715	0.0746	4.3761	0.0686	4.2335	0.0805
32	3.8528	0.1596	3.9164	0.1073	4.1952	0.0743	4.3811	0.0695	4.2220	0.0806

Table 20: Numerical values of the results presented in Figs. 72 and 73 are tabulated. The number of subdivisions in cumulative transverse-momentum space, *M*, for $1 \leq M \leq 150$ (fine binning) and $1 \leq M \leq 32$ (coarse binning). Results for ^{208}Pb + ^{208}Pb interaction at beam momenta of 13*A* and 75*A* GeV/*c*, respectively, the data points with an error for each *M* bin, are presented here.

cumulative and fine binning					cumulative and coarse binning				
	13*A* GeV/*c*		30*A* GeV/*c*			13*A* GeV/*c*		30*A* GeV/*c*	
M	$F_2(M)$	σ_{F_2}	$F_2(M)$	σ_{F_2}	*M*	$F_2(M)$	σ_{F_2}	$F_2(M)$	σ_{F_2}
1	1.0116	0.0074	1.0089	0.0040	1	1.0084	0.0068	1.0119	0.0038
50	1.1064	0.1440	0.8855	0.0664	8	0.9550	0.0193	1.0050	0.0115
70	0.8917	0.1306	0.9463	0.0749	13	0.9941	0.0250	0.9696	0.0143
86	1.1238	0.1522	0.9510	0.0785	17	0.9604	0.0275	0.9659	0.0158
100	0.9526	0.1416	0.9903	0.0826	20	0.9637	0.0285	0.9574	0.0162
111	0.8849	0.1377	0.9239	0.0797	23	0.8772	0.0291	0.9380	0.0165
122	0.9477	0.1201	0.8878	0.0788	26	0.9220	0.0303	0.9413	0.01784
132	0.9174	0.1412	0.9632	0.0825	28	0.9585	0.0309	0.9737	0.0170
141	0.9597	0.1478	0.9475	0.0825	30	0.9248	0.0305	0.9724	0.0177
150	1.0218	0.1274	0.9645	0.0840	32	0.8979	0.0308	0.9637	0.0178

Table 21: Numerical values of the results for ^{40}Ar + ^{45}Sc collisions at 13*A*-75*A* GeV/*c* presented in Figs. 74 and 75 are tabulated. The subdivisions are in cumulative transverse-momentum space. The *top* table corresponds to fine binning, $1 \leq M \leq 150$, and the *bottom* table corresponds to coarse binning, $1 \leq M \leq 32$. The statistical uncertainties, σ_{F_2} are also shown.

	cumulative and fine binning									
	13*A* GeV/*c*		19*A* GeV/*c*		30*A* GeV/*c*		40*A* GeV/*c*		75*A* GeV/*c*	
M	$F_2(M)$	σ_{F_2}	$F_2(M)$	σ_{F_2}	$F_2(M)$	σ_{F_2}	$F_2(M)$	σ_{F_2}	$F_2(M)$	σ_{F_2}
1	1.0154	0.0160	0.9909	0.0102	0.9868	0.0070	0.9984	0.0067	1.0078	0.0077
50	0.8156	0.2882	0.7718	0.1870	1.0588	0.1479	0.6108	0.1017	0.7529	0.1329
70	1.2198	0.3855	1.3373	0.2671	0.6935	0.1287	0.9677	0.1381	0.8461	0.1544
86	0.7659	0.3126	0.8582	0.2215	0.8672	0.1486	0.8760	0.1367	0.9742	0.1721
100	0.4129	0.2384	1.0163	0.2464	0.8606	0.1521	0.8293	0.1363	0.8284	0.1624
111	0.6845	0.3060	0.4828	0.1707	0.8463	0.1519	0.8816	0.1411	0.4828	0.1246
122	0.7079	0.3166	0.7433	0.2145	0.7789	0.1472	0.8553	0.1406	0.7538	0.1571
132	0.8303	0.3389	0.3639	0.1485	0.7951	0.1476	0.7994	0.1351	0.9295	0.1726
141	1.1472	0.4055	0.9522	0.2458	0.9987	0.1688	1.0143	0.1546	0.8325	0.1665
150	0.8732	0.3564	1.0950	0.2656	0.9560	0.1664	0.8354	0.1412	0.7479	0.1594
	cumulative and coarse binning									
1	1.0087	0.0158	0.9918	0.0097	0.9997	0.0070	1.0006	0.0067	1.0245	0.0084
8	0.9148	0.0482	0.9776	0.0338	0.9721	0.0231	0.9548	0.0200	0.9933	0.0245
13	0.9372	0.0620	0.9588	0.0416	0.9075	0.0274	0.9530	0.0253	0.9384	0.0304
17	0.8610	0.0652	0.9335	0.0463	0.9768	0.0313	0.9789	0.0285	0.9228	0.0331
20	0.8364	0.0673	0.9616	0.0481	0.9508	0.0320	0.9865	0.0297	0.9337	0.0346
23	1.1055	0.0819	0.9491	0.0499	0.9834	0.0343	0.9340	0.0302	0.9146	0.0355
26	0.7432	0.0691	0.8737	0.0493	0.9548	0.0348	0.9035	0.0307	0.8926	0.0362
28	0.8070	0.0706	0.8269	0.0474	1.0013	0.0351	0.8976	0.0303	0.8430	0.0349
30	0.9905	0.0801	0.9810	0.0530	0.9290	0.0348	0.9551	0.0320	0.8253	0.0352
32	0.8641	0.0753	1.0222	0.0545	0.9443	0.0352	0.9193	0.0317	0.9763	0.0388

11 Summary

This analysis note reports on the search for the critical point of strongly interacting matter in 0-10% central ^{208}Pb + ^{208}Pb collision at beam momentum of 13*A* and 30*A* GeV/*c*, and ^{40}Ar + ^{45}Sc collisions at beam momenta of 13*A*, 19*A*, 30*A*, 40*A*, and 75*A* GeV/*c* recorded by the NA61/SHINE experiment at the CERN SPS. It includes a brief review of the field, methodology, and results. The search was conducted using intermittency analysis in transverse momentum space applied to protons produced at mid-rapidity. In particular,

(i) Proton intermittency analysis in high energy physics to search for the critical point of strongly interacting matter was discussed in Sec. 3,

(ii) The event and track selection for central ^{208}Pb + ^{208}Pb collisions at beam momentum of 13*A* and 30*A* GeV/*c*, and central ^{40}Ar + ^{45}Sc collisions at beam momenta of 13*A*-75*A* GeV/*c* was discussed in Sec. 5. Proton candidates produced in ^{40}Ar + ^{45}Sc and ^{208}Pb + ^{208}Pb interactions were selected (see Sec. 6.6) by the single (see Sec. 7) and two-particle (see Sec. 8) acceptance maps was also presented.

(iii) New approaches to the proton intermittency analysis to search for the critical point using cumulative variables and statistically independent data points were discussed in Sec. 9,

(iv) Results on second-order scaled factorial moments of proton multiplicity distribution in transverse-momentum space at mid-rapidity were presented in Sec. 10,

The key physics result of the analysis note is the absence of any indication of the critical point in 0-10% central ^{208}Pb + ^{208}Pb collisions at beam momentum of 13*A* and 30*A* GeV/*c*, and ^{40}Ar + ^{45}Sc collisions at beam momenta of 13*A*, 19*A*, 30*A*, 40*A*, and 75*A* GeV/*c*. This refers to the results obtained in transverse-momentum space using intermittency analysis for protons produced at mid-rapidity. The corresponding experimental results are summarized in Figs. 76 and 77, where second-scaled factorial moments are plotted as a function of the number of subdivisions in cumulative transverse-momentum space.

The status of the NA61/SHINE critical point search via proton intermittency is summarized on the diagram of chemical freeze-out temperature and baryon-chemical potential [57] in Fig. 78.

The search for the critical point of strongly interacting matter in the NA61/SHINE data recorded within its system-size and energy scan continues. In particular, the results for Xe+La collisions are still to be obtained.

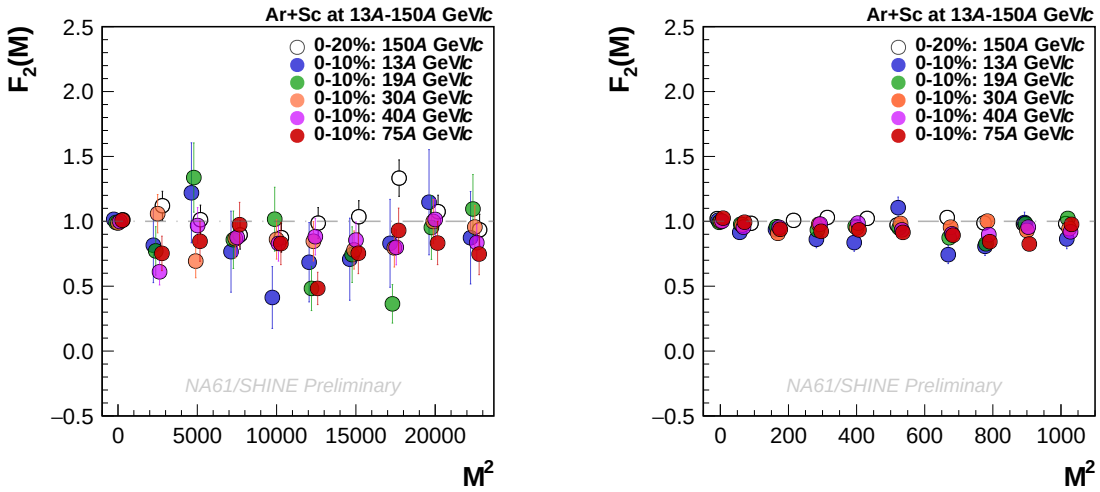

Figure 76: Summary of the proton intermittency results from the NA61/SHINE Ar+Sc energy scan. Results on the dependence of the scaled factorial moment of proton multiplicity distribution on the number of subdivisions in cumulative transverse momentum space M for $1 \leq M \leq 150$ (*left*) and $1 \leq M \leq 32$ (*right*) are shown. The open circles represent results on $0 - 20\%$ central ^{40}Ar + ^{45}Sc collisions at beam momentum of 150*A* GeV/*c* [37]. Closed circles indicate the experimental data results obtained within this work for $0 - 10\%$ central ^{40}Ar + ^{45}Sc collisions at beam momenta of 13*A*, 19*A*, 30*A*, 40*A*, and 75*A* GeV/*c*, respectively. Only statistical uncertainties are indicated. Points for different energies are slightly shifted to increase readability.

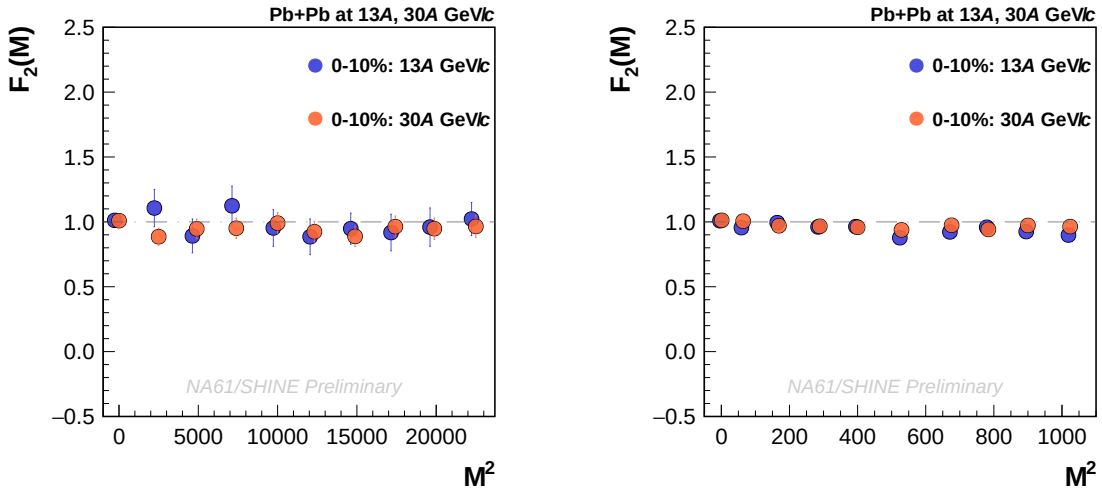

Figure 77: Summary of the proton intermittency results from the NA61/SHINE Pb+Pb energy scan. Results on the dependence of the scaled factorial moment of proton multiplicity distribution on the number of subdivisions in cumulative transverse momentum space M for $1 \leq M \leq 150$ (*left*) and $1 \leq M \leq 32$ (*right*) are shown. Closed circles indicate the experimental data results for $0 - 10\%$ central ^{208}Pb + ^{208}Pb collisions at beam momentum of 13*A* and 30*A* GeV/*c*, respectively, obtained within this work. Only statistical uncertainties are indicated. Points for different energies are slightly shifted to increase readability.

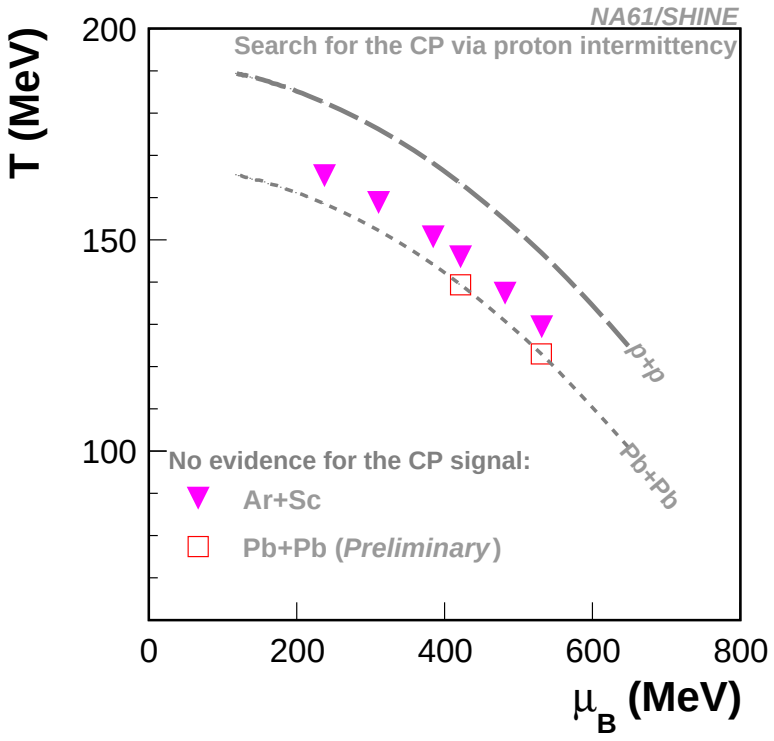

Figure 78: Diagram of chemical freeze-out temperature and baryon-chemical potential. The dashed line indicates parameters in *p*+*p* interactions and the dotted line in the central Pb+Pb collisions [57]. The colored points mark reactions in the $T - \mu_B$ phase diagram for which the search for the critical point was conducted, and no evidence for the critical point was found.

References

[1] M. A. Stephanov, K. Rajagopal, and E. V. Shuryak, "Event-by-event fluctuations in heavy ion collisions and the QCD critical point," Phys. Rev. D, vol. 60, p. 114028, 1999.

[2] P. Braun-Munzinger and J. Wambach, "The Phase Diagram of Strongly-Interacting Matter," Rev. Mod. Phys., vol. 81, pp. 1031–1050, 2009.

[3] A. Bialas and R. B. Peschanski, "Moments of Rapidity Distributions as a Measure of Short Range Fluctuations in High-Energy Collisions," Nucl. Phys. B, vol. 273, pp. 703–718, 1986.

[4] M. A. Shifman, A. I. Vainshtein, and V. I. Zakharov, "QCD and Resonance Physics. Theoretical Foundations," Nucl. Phys. B, vol. 147, pp. 385–447, 1979.

[5] M. I. Gorenstein, V. K. Petrov, and G. M. Zinovev, "Phase Transition in the Hadron Gas Model," Phys. Lett. B, vol. 106, pp. 327–330, 1981.

[6] K. Fukushima and C. Sasaki, "The phase diagram of nuclear and quark matter at high baryon density," Prog. Part. Nucl. Phys., vol. 72, pp. 99–154, 2013.

[7] M. Gyulassy, "The QGP discovered at RHIC," in NATO Advanced Study Institute: Structure and Dynamics of Elementary Matter, 3 2004, pp. 159–182.

[8] E. V. Shuryak, "Quantum Chromodynamics and the Theory of Superdense Matter," Phys. Rept., vol. 61, pp. 71–158, 1980.

[9] S. B. Ruester, V. Werth, M. Buballa, I. A. Shovkovy, and D. H. Rischke, "The Phase diagram of neutral quark matter: Self-consistent treatment of quark masses," Phys. Rev. D, vol. 72, p. 034004, 2005.

[10] C. Greiner, P. Koch, and H. Stoecker, "Separation of Strangeness from Antistrangeness in the Phase Transition from Quark to Hadron Matter: Possible Formation of Strange Quark Matter in Heavy Ion Collisions," Phys. Rev. Lett., vol. 58, pp. 1825–1828, 1987.

[11] E. V. Shuryak, "Multiparticle production in high energy particle collisions." Yad.Fiz., vol. 16, pp. 395–405, 1972.

[12] M. A. Stephanov, "QCD phase diagram and the critical point," Prog. Theor. Phys. Suppl., vol. 153, pp. 139–156, 2004.

[13] H. Sazdjian, "Introduction to chiral symmetry in QCD," EPJ Web Conf., vol. 137, p. 02001, 2017.

[14] K. Fukushima, "Chiral Symmetry and Heavy-Ion Collisions," J. Phys. G, vol. 35, p. 104020, 2008.

[15] P. Castorina, R. V. Gavai, and H. Satz, "The QCD Phase Structure at High Baryon Density," Eur. Phys. J. C, vol. 69, pp. 169–178, 2010.

[16] V. A. Goy, V. Bornyakov, D. Boyda, A. Molochkov, A. Nakamura, A. Nikolaev, and V. Zakharov, "Sign problem in finite density lattice QCD," PTEP, vol. 2017, no. 3, p. 031D01, 2017.

[17] M. Asakawa and K. Yazaki, "Chiral Restoration at Finite Density and Temperature," Nucl. Phys. A, vol. 504, pp. 668–684, 1989.

[18] A. Barducci, R. Casalbuoni, S. De Curtis, R. Gatto, and G. Pettini, "Chiral Phase Transitions in QCD for Finite Temperature and Density," Phys. Rev. D, vol. 41, p. 1610, 1990.

[19] J. Berges and K. Rajagopal, "Color superconductivity and chiral symmetry restoration at nonzero baryon density and temperature," Nucl. Phys. B, vol. 538, pp. 215–232, 1999.

[20] A. M. Halasz, A. D. Jackson, R. E. Shrock, M. A. Stephanov, and J. J. M. Verbaarschot, "On the phase diagram of QCD," Phys. Rev. D, vol. 58, p. 096007, 1998.

[21] N. G. Antoniou and A. S. Kapoyannis, "Bootstraping the QCD critical point," Phys. Lett. B, vol. 563, pp. 165–172, 2003.

[22] Y. Hatta and T. Ikeda, "Universality, the QCD critical / tricritical point and the quark number susceptibility," Phys.Rev., vol. D67, p. 014028, 2003.

[23] Z. Fodor and S. D. Katz, "Lattice determination of the critical point of QCD at finite T and mu," JHEP, vol. 03, p. 014, 2002.

[24] P. de Forcrand and O. Philipsen, "The QCD phase diagram for three degenerate flavors and small baryon density," Nucl. Phys. B, vol. 673, pp. 170–186, 2003.

[25] S. Ejiri, C. R. Allton, S. J. Hands, O. Kaczmarek, F. Karsch, E. Laermann, and C. Schmidt, "Study of QCD thermodynamics at finite density by Taylor expansion," Prog. Theor. Phys. Suppl., vol. 153, pp. 118–126, 2004.

[26] F. Karsch, "Lattice QCD at non-zero temperature and density," 12 2022.

[27] J. C. Vassilicos, Ed., Intermittency in Turbulent Flows, nov 30 2000.

[28] B. B. Mandelbrot, "Intermittent turbulence in self-similar cascades: divergence of high moments and dimension of the carrier," J. Fluid Mech., vol. 62, no. 2, pp. 331–358, 1974.

[29] J. Wosiek, "Intermittency in the ising systems," Acta Physica Polonica, Series B, vol. 19, no. 10, pp. 863–866, 1988.

[30] H. Satz, "Intermittency and Critical Behavior," Nucl. Phys. B, vol. 326, pp. 613–618, 1989.

[31] A. Bialas and R. Hwa, "Intermittency parameters as a possible signal for quark - gluon plasma formation," Phys.Lett., vol. B253, pp. 436–438, 1991.

[32] T. Czopowicz, "Search for critical point via intermittency analysis in NA61/SHINES," PoS, vol. CPOD2021, p. 039, 2021.

[33] A. Bialas and M. Gazdzicki, "A New variable to study intermittency," Phys. Lett. B, vol. 252, pp. 483–486, 1990.

[34] E. A. De Wolf, I. M. Dremin, and W. Kittel, "Scaling laws for density correlations and fluctuations in multiparticle dynamics," Phys. Rept., vol. 270, pp. 1–141, 1996.

[35] T. Anticic et al., "Critical fluctuations of the proton density in A+A collisions at 158A GeV," Eur. Phys. J. C, vol. 75, no. 12, p. 587, 2015.

[36] N. G. Antoniou, F. K. Diakonos, A. S. Kapoyannis, and K. S. Kousouris, "Critical opalescence in baryonic QCD matter," Phys. Rev. Lett., vol. 97, p. 032002, 2006.

[37] H. Adhikary et al., "Search for the critical point of strongly-interacting matter in ^{40}Ar + ^{45}Sc collisions at 150A GeV/c using scaled factorial moments of protons," 5 2023.

[38] H. Adhikary, "Search for the critical point of strongly interacting matter (Intermittency analysis by NA61/SHINE at CERN SPS)," EPJ Web Conf., vol. 274, p. 06008, 2022.

[39] M. Gazdzicki et al., "Study of hadron production in hadron-nucleus and nucleus-nucleus collisions at the CERN SPS," CERN, Geneva, Tech. Rep., Nov 2006. [Online]. Available: http://cds.cern.ch/record/995681

[40] N. Abgrall et al., "NA61/SHINE facility at the CERN SPS: beams and detector system," JINST, vol. 9, p. P06005, 2014.

[41] S. Afanasiev et al., "The NA49 large acceptance hadron detector," Nucl. Instrum. Meth. A, vol. 430, pp. 210–244, 1999.

[42] D. Banas, A. Kubala-Kukus, M. Rybczynski, I. Stabrawa, and G. Stefanek, "Influence of target material impurities on physical results in relativistic heavy-ion collisions," Eur. Phys. J. Plus, vol. 134, no. 1, p. 44, 2019.

[43] D. V. Babos, V. C. Costa, and E. R. Pereira-Filho, "Wavelength dispersive x-ray fluorescence (wd-xrf) applied to speciation of sulphur in mineral supplement for cattle: Evaluation of the chemical and matrix effects," Microchemical Journal, vol. 147, pp. 628–634, 2019. [Online]. Available: https://www.sciencedirect.com/science/article/pii/S0026265X18315303

[44] A. Acharya et al., "Measurements of π^- production in ^{7}Be+^{9}Be collisions at beam momenta from 19A to 150AGeV/c in the NA61/SHINE experiment at the CERN SPS," Eur. Phys. J. C, vol. 80, no. 10, p. 961, 2020, [Erratum: Eur.Phys.J.C 81, 144 (2021)].

[45] ——, "Spectra and mean multiplicities of π^- in central^{40}Ar+^{45}Sc collisions at 13A, 19A, 30A, 40A, 75A and 150A Ge V/c beam momenta measured by the NA61/SHINE spectrometer at the CERN SPS," Eur. Phys. J. C, vol. 81, no. 5, p. 397, 2021.

[46] A. SERYAKOV, "PSD acceptance maps for event selection," CERN, Geneva, Tech. Rep. [Online]. Available: https://edms.cern.ch/document/1867336/1

[47] P. Bożek, W. Broniowski, M. Rybczynski, and G. Stefanek, "GLISSANDO 3: GLauber Initial-State Simulation AND mOre..., ver. 3," Comput. Phys. Commun., vol. 245, p. 106850, 2019.

[48] Lewicki, Maciej Piotr PhD Thesis at https://cds.cern.ch/record/2772291?ln=en.

[49] N. G. Antoniou, F. K. Diakonos, C. N. Ktorides, and M. Lahanas, "Critical events and intermittency in nuclear collisions," Phys. Lett. B, vol. 432, pp. 8–14, 1998.

[50] NA61/SHINE acceptance map available at https://edms.cern.ch/document/2778197.

[51] B. Efron, "Bootstrap Methods: Another Look at the Jackknife," Annals Statist., vol. 7, no. 1, pp. 1–26, 1979.

[52] S. Samanta, T. Czopowicz, and M. Gazdzicki, "Scaling of factorial moments in cumulative variables," Nucl. Phys. A, vol. 1015, p. 122299, 2021.

[53] B. Wosiek, "Intermittency analysis of correlated data," Acta Phys. Polon. B, vol. 21, pp. 1021–1030, 1990.

[54] H. Adhikary, "Proton intermittency analysis note (will be upload soon to edms/cds)," NA61/SHINE at CERN SPS, CERN at Geneva, Tech. Rep.

[55] S. Samanta, T. Czopowicz, and M. Gazdzicki, "Impact of momentum resolution on factorial moments due to power–law correlations between particles," J. Phys. G, vol. 48, no. 10, p. 105106, 2021.

[56] T. Anticic et al., "Search for the QCD critical point in nuclear collisions at the CERN SPS," Phys. Rev. C, vol. 81, p. 064907, 2010.

[57] F. Becattini, J. Manninen, and M. Gazdzicki, "Energy and system size dependence of chemical freeze-out in relativistic nuclear collisions," Phys. Rev., vol. C73, p. 044905, 2006.